ORIGINATING ACTIVITY (Corporate author)	2a. REPORT SECURITY CLASSIFICATION
Purdue University	Unclassified
	2b. GROUP

REPORT TITLE

The Optimum Shaping of Axisymmetric Bodies for Minimum Drag in Incompressible Flow

DESCRIPTIVE NOTES (Type of report and inclusive dates)

Technical Report No. 4, June 1972

AUTHOR(S) (Last name, first name, initial)

Parsons, Jerome S. and Goodson, Raymond E.

REPORT DATE	7a. TOTAL NO. OF PAGES	7b. NO. OF REFS
June 1972	197	35

CONTRACT OR GRANT NO.	9a. ORIGINATOR'S REPORT NUMBER(S)
N00014-67-A-0226-0012	
PROJECT NO	No. 4
NR 041-423	
	9b. OTHER REPORT NO(S) (Any other numbers that may be assigned this report)

AVAILABILITY/LIMITATION NOTICES This document has been approved for public release and sale; its distribution is unlimited.

SUPPLEMENTARY NOTES	12. SPONSORING MILITARY ACTIVITY
	Office of Naval Research

ABSTRACT The engineering problem is the design of submerged minimum drag axisymmetric vehicles for a specified enclosed volume and constant speed. Propulsion is not considered so that drag rather than power is to be minimized. Drag reduction is to be accomplished solely through manipulation of the vehicle shape; other means of drag reduction, such as polymer injection into the boundary layer, are not considered.

The optimization problem is formulated as a nongradient search in a finite constrained parameter space. Two classes of bodies, described by five and eight parameters, are considered. The bodies are constrained to be well behaved based on previous hydrodynamic experience. The drag model, valid for nonseparating flows, consists of computer programs available in the literature and is representative of state-of-the-art drag prediction methods. The requirement for nonseparating flow represents an additional constraint on the optimization problem. Two optimization methods representing diverse search philosophies are used to obtain the optimal solutions. These include Box's Complex Method and Powell's Method of Conjugate Directions used in conjunction with a penalty function.

CONTINUED

I

13. Abstract (CONTINUED)

        The results show that significant drag reduction is possible
through shape manipulation. Reductions of one-quarter to one-third
below the best existing designs have been obtained. All optimal
designs exploit laminar boundary layers. If laminar flow is not
allowed, then drag reduction below the best existing designs apparently
must be accomplished by means other than shape manipulation. The
optimal laminar shape is a strong function of Reynolds number, ranging
from quite slender at low values to quite "fat" at high values. The
minimum drag shapes have a high sensitivity to early transition.
Suboptimal low drag bodies without this characteristic are used for
hydrodynamic design. Extensive runs at one Reynolds number suggest
that there is a unique global minimum drag shape at each Reynolds
number.

II

PREFACE

This technical report is a reprint of the main body
of a Ph.D. thesis for research which was done at the
Automatic Control Center and the Fluids Laboratory of
Westinghouse Research by Mr. J.S. Parsons under the direc-
tion of Professor R.E. Goodson. Research support for the
work was provided by the Office of Naval Research under
contract N00014-A-67-0226-0012, NR 041-423 and by the
Westinghouse Research Laboratories   The work described
in the thesis is being continued at the Automatic Control
Center by investigating better drag models and experimenting
with more efficient optimization techniques.

III.

$$\overline{IV}$$

TABLE OF CONTENTS

$\overline{VI}$

LIST OF TABLES

Table   **Page**

LIST OF FIGURES

Figure	Page

LIST OF SYMBOLS

Symbol	Definition
a_i	Component of parameter set a_i, $i = 1, \ldots, N$.
a_{L_i}, a_{U_i}	For Complex Method, the temporary lower and upper parameter boundaries, respectively, used during the initial complex generation. For Powell's Method, the lower and upper scaling values, respectively, used to scale the search space.
C_D	Drag coefficient defined as $\mathrm{Drag}/(\frac{1}{2}\,\rho U_\infty^2 V^{\frac{2}{3}})$.
C_D^*	Value of drag coefficient at a local minimum.
C_f	Skin friction coefficient defined as $\tau_w/(\frac{1}{2}\,\rho U_\infty^2)$.
C_p	Pressure coefficient defined as $(p-p_\infty)/(\frac{1}{2}\,\rho U_\infty^2)$.
$C_{p_{max}}$	Maximum allowable pressure coefficient to occur downstream of $C_{p_{min}}$. Used to help avoid separating boundary layers.
$C_{p_{min}}$	Minimum allowable pressure coefficient. Used to help avoid separating boundary layers.
D	Vehicle drag. Also maximum diameter of body.
f_r	Fineness ratio defined as L/D where D is the maximum diameter.
H	Shape factor defined as δ^*/θ.
K	Number of vertices in N-dimensional complex figure of the Complex Method. Normally $K = 2N$.
K_1	Body curvature at X_m.
k_e	Expansion factor used to generate body point distribution near leading edge.
k_1	Nondimensional curvature at X_m.

Symbol	Definition
L	Overall body length.
N	Number of independent parameters. Equivalently, the dimensionality of the search space.
NN	Total number of body points along body surface used in drag computation.
PF	Performance function. For drag minimization PF is the same as C_D.
p	Pressure impressed on the boundary layer.
p_∞	Free-stream static pressure.
R_i	Profile radius at X_i.
R_n	Radius of curvature at nose.
R_S	Running surface-length Reynolds number defined as $S\, u_e/\nu$.
R_V	Reynolds number based on (volume)$^{\frac{1}{3}}$. $R_V = V^{\frac{1}{3}} U_\infty/\nu$.
R_θ	Momentum thickness Reynolds number defined as $\theta u_e/\nu$.
r	Radial coordinate of a point in the boundary layer defined as $r_0 + y \cos \alpha$.
r_i	Nondimensional profile radius at X_i defined as $2R_i/D$.
r_n	Nondimensional radius of curvature at nose.
r_0	Body radius. Same as Y.
S	Surface length. Same as x.
S_i	Profile slope at X_i.
S_t	Profile slope at tail.
S_{Total}	Total surface arc-length.
s_i	Nondimensional profile slope at X_i.
s_t	Nondimensional slope at tail.

Symbol	Definition
T	Terminal profile radius.
t	Nondimensional terminal profile radius defined as $2T/D$.
u	Tangential velocity component at a point (x, y) in the boundary layer.
u_e	Local velocity at the edge of the boundary layer.
U_∞	Free-stream reference velocity.
V	Enclosed volume of vehicle.
v	Normal velocity component at a point (x, y) in the boundary layer.
X	Axial coordinate along body centerline.
X_i	Axial location of inflection point.
X_m	Axial location of maximum diameter D.
x	Streamwise curvilinear coordinate for boundary layer. Same as S.
x_i	Nondimensional axial location of inflection point defined as X_i/L.
x_m	Nondimensional axial location of maximum diameter D defined as X_m/L.
Y	Body radius. Same as r_o.
y	Normal curvilinear coordinate for boundary layer.
α	Angle between the surface tangent and the body centerline in a meridional plane.
ΔS_o	Initial step size for body point distribution.
ΔS_u	Uniform step size for body point distribution.
δ	Boundary layer thickness defined as the y-distance for which $u/u_e = .995$.
δ^*	Displacement thickness associated with momentum integral equation. Defined as $\int_o^\infty \frac{r}{r_o}(1- \frac{u}{u_e})dy$ for incompressible flow.

Symbol	Definition
δ^*_{ax}	External axisymmetric flow displacement thickness used to viscously correct the inviscid pressure distribution.
ϵ	Eddy viscosity.
ϵ_i	Inner region eddy viscosity.
ϵ_o	Outer region eddy viscosity.
ϵ_s	Relative convergence tolerance used in search methods.
θ	Momentum thickness associated with momentum integral equation and Young's formula for computing drag. Defined as $\int_0^\infty \frac{r}{r_o} \frac{u}{u_e}(1- \frac{u}{u_e})dy$ for incompressible flow.
μ	Fluid dynamic viscosity.
ν	Fluid kinematic viscosity.
ρ	Fluid density.
τ_w	Wall shear stress.

XV

ABSTRACT

The engineering problem is the design of submerged minimum drag
axisymmetric vehicles for a specified enclosed volume and constant
speed. Propulsion is not considered so that drag rather than power is
to be minimized. Drag reduction is to be accomplished solely through
manipulation of the vehicle shape; other means of drag reduction, such
as polymer injection into the boundary layer, are not considered.

The optimization problem is formulated as a nongradient search in
a finite constrained parameter space. Two classes of bodies, described
by five and eight parameters, are considered. The bodies are con-
strained to be well behaved based on previous hydrodynamic experience.
The drag model, valid for nonseparating flows, consists of computer
programs available in the literature and is representative of state-of-
the-art drag prediction methods. The requirement for nonseparating flow
represents an additional constraint on the optimization problem. Two
optimization methods representing diverse search philosophies are used
to obtain the optimal solutions. These include Box's Complex Method
and Powell's Method of Conjugate Directions used in conjunction with
a penalty function.

The results show that significant drag reduction is possible
through shape manipulation. Reductions of one-quarter to one-third
below the best existing designs have been obtained. All optimal designs
exploit laminar boundary layers. If laminar flow is not allowed, then
drag reduction below the best existing designs apparently must be
accomplished by means other than shape manipulation. The optimal lami-
nar shape is a strong function of Reynolds number, ranging from quite

slender at low values to quite "fat" at high values. The minimum drag shapes have a high sensitivity to early transition. Suboptimal low drag bodies without this characteristic are used for hydrodynamic design. Extensive runs at one Reynolds number suggest that there is a unique global minimum drag shape at each Reynolds number.

CHAPTER 1

INTRODUCTION

Of fundamental interest in the field of fluid mechanics is the study of fluid forces exerted on a moving body. In the area of hydrodynamics, a time-honored goal of the naval architect has been the reduction of vehicle resistance by means of vehicle shape as well as by more elaborate schemes [1], such as viscoelastic polymer injection into the boundary layer.

We are considering here the shape and resulting resistance, or drag, of bodies submerged in an incompressible fluid. The applications are directed toward vehicles such as torpedoes and submarines deeply submerged in water. The primary function of such vehicles is to provide an enclosed volume in which a payload is carried.

The purpose of the present study is to include the hydrodynamics as part of an optimization problem in which the vehicle drag is to be minimized through shape manipulation. Other means of drag reduction are not considered. The hydrodynamic problem is made more tractable by restricting the analysis to the class of axisymmetric vehicles (bodies of revolution) without appendages immersed in axisymmetric flow (zero angle of attack).

Stated somewhat more precisely, the optimization problem involves the following: for a specified incompressible fluid, vehicle volume, and constant vehicle speed, find the axisymmetric body shape which minimizes the drag. The vehicle whose shape minimizes the drag is defined as the optimum body. The equivalent nondimensional optimization problem may be stated as follows: for a specified Reynolds number $R_V = U_\infty V^{\frac{1}{3}}/\nu$, find the vehicle shape which minimizes the drag

coefficient $C_D = D/(\frac{1}{2}\rho U_\infty^2 V^{\frac{2}{3}})$, where U_∞ is the constant vehicle speed, V is the vehicle's enclosed volume, ν is the fluid kinematic viscosity, D is the vehicle drag, and ρ is the fluid density.

The primary concern here is the design of the largest vehicle volume with the lowest possible drag at a given speed; there are no prescribed constraints on the body. From the hydrodynamics analysis point of view, the actual volume and velocity separately are not important; the body shape and characteristic Reynolds number R_V completely establish the fluid dynamics. Thus a particular body shape has the same drag coefficient C_D over a wide range of velocities and volumes so long as the Reynolds number R_V is unchanged.

Other design problems may be more conveniently handled by using a characteristic Reynolds number based on something other than $(volume)^{\frac{1}{3}}$. For example, the torpedo must have a fixed maximum diameter (constant frontal-area); it is more convenient to specify a Reynolds number based on maximum diameter rather than volume. Other characteristic lengths which may be useful in design problems include body length and $(wetted area)^{\frac{1}{2}}$. It is emphasized that the optimization formulation in the present study applies to any of these design problems.

It is not known if a unique optimum body exists for each Reynolds number. That is, there may be an entire class of bodies which have the same minimum drag coefficient at a given Reynolds number. If such is the case, then the designer must introduce additional considerations or constraints to obtain the one design best suited for his application. For example, the optimization problem ignores the sensitivity of drag changes with body velocity variations and ignores the effect of angle of attack on drag. If the designer has several minimum drag body designs, he considers these kinds of ideas in making the final selection. Such considerations are outside the scope of the present study. A more complete discussion on design constraints is given in Chapter 3.

The application of formal optimization methods to the drag minimization problem has not appeared in the literature to date. One reason for this absence is the fact that no reliable drag model for arbitrary axisymmetric bodies in incompressible flow is available. More fundamentally,

there is an incomplete understanding of the fluid flow physics in the boundary layer transition region, in the turbulent boundary layer development, in the turbulent boundary layer separation region, and in the wake region following separation. All of these phenomena are of primary importance in drag prediction. In addition, there are other factors which complicate the prediction of drag in practice [2], such as the effects of ambient turbulence, body surface waviness, and body vibration on the boundary layer development.

With the lack of reliable drag models, all published work to date directed toward the design of low drag axisymmetric bodies in incompressible flow has been mainly experimental in nature. Two studies will be noted here.

1.1 Series 58 Study

An experimental study of drag for a systematic series of axisymmetric bodies was reported by Gertler in 1950 [3]. The series, known as "Series 58," was systematic in that five parameters characterizing the body shapes were perturbed one at a time about a selected "parent model." Twenty-four body shapes were selected, models were built, and tests were conducted by towing the models through water at different speeds. The results indicated that there was indeed a "best shape" for reducing drag. The results were to be extrapolated from model size and speed to full-scale submarine design.

From the optimization (drag minimization) point of view, the one-at-a-time perturbation scheme about the parent model represents a basic weakness in the Series 58 study. The information which may be drawn from the study is the variation in drag due to the variation of one parameter while holding four other parameters constant. Such information is "local" in nature, that is, the variation effects are pertinent only to the parent model. Such information cannot be construed as "global;" hence, no claim to global minimum drag shapes can be made.

A design assumption inferred from the Series 58 study is that at submarine Reynolds numbers ($R_v \simeq 10^9$) boundary layers are always

turbulent and that it is unrealistic to attempt to exploit laminar boundary layers to reduce drag. Without experimental data it is difficult if not impossible to judge the validity of such an assumption since so many extraneous factors influence the actual boundary layer development in a real flow situation. The Series 58 "best shape" may be a low drag design; however, it cannot be inferred from Reference 3 that such a shape represents a minimum drag shape at its design Reynolds number of around 10^9.

1.2 Laminar Flow "Dolphin" Body

A low-drag shape for torpedo-type Reynolds numbers was reported by Carmichael in 1966 [2]. The purpose of the study was to determine if significant drag reduction was possible through shape manipulation alone. A formal shape-synthesizing procedure was not developed; rather, one shape was designed based on NACA low drag airfoil data. The one model, dubbed the "Dolphin," was tested extensively by gravity-powered drop tests in the Pacific Ocean. A significant drag reduction was noted, the "Dolphin" having half the drag of a conventional torpedo at similar Reynolds numbers.

The low drag was achieved primarily by the "Dolphin's" ability to maintain a long run of laminar boundary layer. This fact in itself is important since prior to the "Dolphin" testing it was generally accepted that no significant amount of laminar boundary layer flow could be maintained at such high Reynolds numbers ($R_V \simeq 10^7$).

While the "Dolphin" is not a minimum drag shape, it certainly demonstrates the practical possibility of exploiting laminar boundary layers and body shaping in general to produce efficient low-drag designs, at least in the tested Reynolds number range.

1.3 Outline of the Text

In Chapter 2 the drag model used in this study is discussed in detail. The quality of the model is indicated by comparing drag

predictions with some of the experimental data available in the literature. Chapters 3 and 4 present the formulation of the optimization problem. A brief discussion of several possible formulations is given. The characteristics of the drag minimization problem which lead to the selected formulation are discussed. Chapter 5 presents the optimum body shapes found during this study. Comparisons with previous designs are made, including comparisons with some powerful swimmers found in nature. Chapter 6 presents conclusions and recommendations. The weaknesses of the drag model and optimization procedure are reviewed. Improvements in both areas are suggested, along with proposed future research.

CHAPTER 2

FLUID FLOW MODEL

This chapter discusses the general nature of the fluid physics and presents the drag model as used in the optimization problem. Only in recent years have the practical tools for predicting drag of arbitrary axisymmetric bodies in incompressible flow appeared in the literature, an example is Reference 4. These methods, while founded on more or less rigorous theoretical considerations, are forced to rely on some empirical correlations and simplifying assumptions. The empirical results and assumptions, along with the consequential limitations, vary from one investigator to the next; hence, no one method of drag prediction is regarded as standard. Therefore, it is the intent here also to indicate the quality of the drag model from which the quality of the optimization results may be inferred.

2.1 General Nature of the Physical Problem

The physical phenomena being considered here are sketched in Figure 1. The fixed, rigid axisymmetric body is immersed in an incompressible fluid medium which at a great distance from the body moves uniformly from left to right. The zero incidence (axisymmetric) flow is deflected in the vicinity of the vehicle resulting in a streamwise pressure gradient along a meridional line on the body surface.

The entire flow field F is dominated by inertial (non-viscous) forces except for a thin layer next to the body surface. Even for fluids of low viscosity, such as water or air, viscous forces dominate due to large normal velocity gradients which exist in this thin boundary layer.
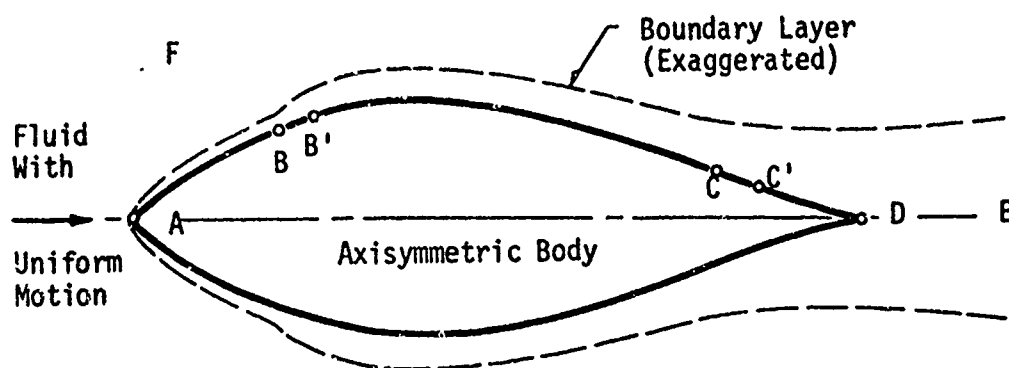
Figure 1. General Incompressible Zero Incidence Flow about an Axisymmetric Body.
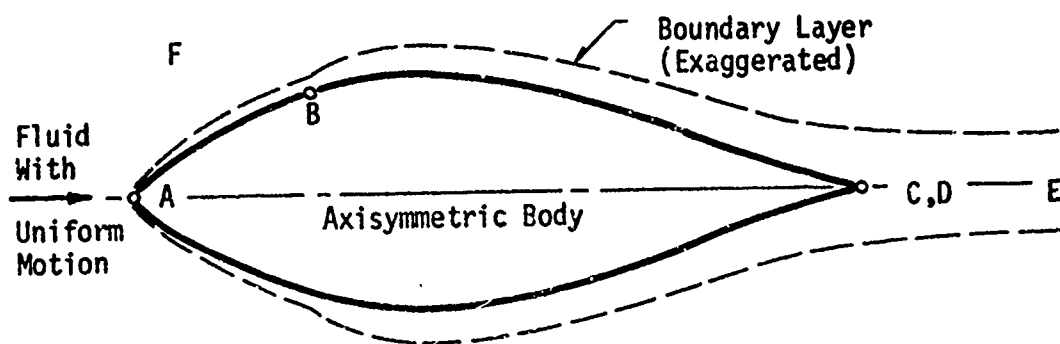
Figure 2. Simplified Nonseparating Flow Considered in Present Study.

Because of its fundamental importance to vehicle drag, the boundary layer development will be discussed somewhat in detail. Referring to Figure 1, the boundary layer is divided into several streamwise regions along a meridional line on the body surface.

The laminar region AB is well ordered relative to our own scale and can be readily described by the mathematics of continuum mechanics. This region is well understood in the sense that the mathematical description, with its assumptions, yields predicted behavior which agrees well with that observed in real laminar flows.

In the region BB' the fluid laminas, through some destabilizing process not fully understood, become chaotic on a macroscopic scale. One theory [5, 6] explains the process of transition in terms of the stability of small disturbances in the laminar flow. At point B, downstream of the so-called neutral stability point which is somewhere in the laminar region AB, certain disturbance frequencies begin to amplify rather than decay. As the fluid layers move downstream, the disturbances amplify and spread until the motion of the entire boundary layer crosssection is chaotic, at which point (B') the boundary layer is said to be fully turbulent.

The actual transition length BB' may be large or small depending on how fast the disturbances amplify. Some of the factors influencing the location and extent of the transition region for incompressible flow are listed below [5]:

1. Free-stream turbulence levels relative to free-stream mean velocity

2. Streamwise pressure gradient on body

3. Surface roughness and waviness

4. Body noise and vibration

The presence of free-stream turbulence, surface roughness and waviness, or body noise and vibration introduces disturbances in the laminar layer in addition to those already occurring naturally by self-excitation; the effect is the tendency to hasten transition. A negative pressure gradient (favorable, velocity increasing) tends to suppress transition, while a positive pressure gradient (adverse, velocity decreasing) tends

to hasten traisition, that is, tends to make the laminar layer more un-
stable. These qualitative effects have been verified experimentally [6];
all quantitative relationships rely on empiricisms to a greater or lesser
degree.

In the region B'C the boundary layer is fully turbulent, that is,
chaotic on a macroscopic scale. No rational theory exists to explain
the complex fluctuating turbulent motion. All attempts to describe the
phenomena have relied on hypotheses which are incomplete without some
empirical data. One example is Prandtl's mixing-length theory [6]; the
functional form of the mixing length is not established within the
theory, much less any constants within the functional form.

Turbulent flow is regarded as the superposition of mean and fluctu-
ating motions. The presence of the fluctuations has a decided effect on
the mean motion, even when the fluctuating velocities are a small per-
centage (1 - 2%) of the mean value. Energy is constantly transferred
from the mean motion to "large scale" fluctuations, and hence to pro-
gressively smaller fluctuations; ultimately the energy is dissipated as
heat. The apparent effect of the fluctuating motion is an increased
resistance by the mean flow to fluid deformation. In other words the
mean motion behaves as if the fluid had an increased viscosity compared
to the same fluid in laminar flow. The apparent viscosity of the mean
motion depends not only on the fluid but also, apparently, on the fluid
kinematics as well. The relationship between the apparent fluid viscosity
and the fluctuating motion is the central concept which defies complete
understanding.

Even with a lack of understanding of the basic mechanism of turbu-
lent motion, the mean turbulent flow can be predicted with the aid of
semi-empirical relationships [7]. The trend today is to use complex,
semi-empirical relationships, so-called "eddy viscosity" models, to
compute the apparent increase in fluid viscosity. The eddy viscosity
is a local quantity which must be computed iteratively since the fluid
kinematics affects the apparent viscosity which in turn affects the
kinematics. In all probability, however, the eddy viscosity concept,
which attempts to relate apparent viscosity to fluctuating motion, will
be replaced by more fundamental turbulent flow shear models in the future.

In the region CC' the turbulent boundary layer separates from the body surface. By this it is meant that as one proceeds toward the trailing edge along a meridian on the body surface, a point is reached at which the fluid motion immediately adjacent to the body reverses direction. The classical view of laminar separation assumes this flow reversal to occur at a point in a steady manner and to be synonymous with zero skin friction. This view is not adequate for turbulent boundary layer separation which may be unsteady both in space and time [8]. That is, "spots" of turbulent flow reversal may occur upstream of the fully separated region; these "spots" may be unsteady as well. Due to a lack of understanding of the physics of turbulent separation, it is common practice to model turbulent separation as if it were a steady phenomenon occurring at a point on the body meridian, that is, along an axisymmetric ring on the surface of an axisymmetric body.

The region C'DE is a fully separated turbulent wake. The means to compute turbulent wakes in the vicinity of arbitrary axisymmetric bodies are not established, although wakes behind blunt-ended cylinders have been predicted successfully [9].

It should be apparent that the complete flow associated with a submerged body is highly complex. Some of the most subtle physics of nature are probably associated with the phenomena of fluid flow. The incomplete understanding has forced investigators to rely to a greater or lesser degree on empirically based relationships, subject to experimental verification, in order to predict fluid flow behavior. The next section discusses the simplified flow field, and its limitations, to be considered in the present study as well as the methods used to predict such flows.

2.2 Simplified Flow Field and Its Solution

This section describes the somewhat simplified flow field and its limitations considered in the present study. The methods used to compute the flow are discussed briefly in the context of drag prediction.

The simplified flow field considered here is illustrated in Figure 2. The flow region F outside the boundary layer is accurately modeled by invisc ' potential flow theory. The boundary layer is laminar from the forward stagnation point A to the transition point B. Transition is assumed to occur at a single point B rather than over a region. The boundary layer is treated as fully turbulent from the transition point B to the trailing edge C. Turbulent separation is assumed not to occur so that the wake region CDE is due to viscous displacement effects only. In fact, if a body has a separating turbulent boundary layer, as indicated by any suitable separation criterion, then the relevance of the drag model described here is not known.

The flow field described here is essentially that considered by Cebeci [4] in his work on numerical drag prediction. In the present study we have taken non-proprietary versions of the component computer programs developed by Cebeci, A. M. O. Smith, and their co-workers, modified them as required, and combined them into a numerical drag package. The discussion following will pertain to the drag model as used in the present study and does not pertain necessarily to any drag package or component programs used within the Douglas Aircraft Company.

Inviscid Flow Outside the Boundary Layer. The zero-incidence inviscid flow about a rather general axisymmetric body has been successfully formulated for numerical solution by A. M. O. Smith and his co-workers [10]. The axisymmetric problem considered here is a subset of the more general geometries and flows which can be handled by Smith's formulation. The numerical procedure is extremely well documented [11] and is known generally as the Douglas-Neumann method.

In the context of the present problem, Smith's formulation considers a uniform flow field in which is placed a stationary hypothetical "transparent image" of the axisymmetric body. The body is temporarily regarded as "transparent" to the flow in that the flow field remains unperturbed. In this hypothetical situation the fluid flows uniformly from left to right, entering the body interior at some areas and leaving at others. Since the real body is impervious to the fluid, then it is apparent that the hypothetical transparent body must somehow be made impervious

also. This is done by distributing fluid sources along the body surface so that at every point on the surface the normal velocity component is zero. Stated another way, the proper source distribution, which is unique [10], causes the transparent body to become a streamline in the flow field. The superposing of the uniform flow and the source distribution flow results in the inviscid flow about the impervious body.

The Douglas-Neumann method reduces the problem of computing a source distribution to one of solving a linear system. A modified Seidel iteration scheme has proven efficient in solving for the source distribution and hence the inviscid pressure distribution.

The pressure impressed on the real body in a real, non-separating flow is the same as the inviscid pressure except as it is modified by viscous displacement effects. By this it is meant that the inviscid streamlines are shifted somewhat both by the retarded boundary layer and viscous wake flows. For non-separating bodies, the effect of this modification to the inviscid pressure distribution is small. But it is the viscous displacement effect, however small, that accounts for the pressure drag of a non-separating body.

If the flow does not separate from the body, then it is assumed that the inviscid pressure, as computed by the Douglas-Neumann method, is a reasonable approximation to the experimental distribution. This assumption appears to be justified particularly for bodies with no dominating rear stagnation point in inviscid flow. Examples are those with "inflected aftbodies," i.e., with "semi-infinite tailbooms" or with cusped pointed tails (Figures 8 and 13). For these kinds of bodies the inviscid flow tends to free-stream conditions rather than stagnation.

For bodies with dominating rear stagnation points, which apparently all non-inflected aftbodies have, the inviscid pressure is a poor approximation to the experimental distribution in the vicinity of the tail, due both to viscous displacement effects and probable separation. If the effect of separation on the inviscid flow streamlines is small compared to viscous displacement effects, then it may be possible to approximate the experimental pressure distribution, at least for the purposes of computing drag. The procedure suggested in Reference 4 is to replace the rear-stagnating velocity distribution by a linear

extrapolation of the inviscid velocity from 95% length to the trailing edge. That is, a straight line is drawn tangent to the curve of inviscid velocity versus axial distance at 95% length and is extended to the trailing edge. The inviscid velocity over the first 95% of the body remains unchanged. Using the modified velocity distribution, the boundary layer is computed. If separation does not occur, then the viscous displacement is added to the body geometry. The inviscid flow about this new "viscous body" is computed. The resulting corrected pressure should be a better approximation to the experimental distribution than the original inviscid flow or its linearly extrapolated modification. However, it cannot be assumed a priori that the corrected pressure is indeed the experimental distribution since the correction depends on the somewhat arbitrarily modified inviscid flow. Also, repeated corrections to the pressure do not imply convergence to the experimental distribution.

A further comment is in order concerning the correction to the pressure. The concept of viscous displacement is based on mass conservation. That is, the inviscid flow must adjust itself to compensate for the retarded flow in the boundary layer and viscous wake. This is necessary so that the total integrated mass flow across any infinite plane perpendicular to the body axis is conserved when the flow is steady. Therefore, the proper displacement thickness to be added to the body geometry for the purpose of correcting the pressure must be derived from mass conservation principles, not from the momentum integral equation. For this reason, the definition of displacement thickness δ^* given by equation (2.17) does not conserve mass flow. The derivation of the displacement thickness δ^*_{ax} for mass conservation in an external axisymmetric flow is given in Appendix A. The relation between δ^*_{ax} and δ^* as defined by equation (2.17) is

$$\delta^*_{ax} = \frac{r_0}{\cos \alpha} \left[-1 + \left(1 + \frac{2 \cos \alpha}{r_0} \delta^*\right)^{\frac{1}{2}} \right] \qquad (2.1)$$

where r_0 and α are shown in Figure 3. The quantity δ^*_{ax} is the proper displacement thickness to use for correcting the inviscid pressure distribution. The value of δ^*_{ax} is always less than that of δ^*, particularly when $\frac{\cos \alpha}{r_0} \delta^*$ is much larger than unity.

In summary, the correct pressure for computing the boundary layer and drag is the experimental distribution. For inflected aftbodies which do not have a dominant rear stagnation point in inviscid flow, the inviscid pressure is assumed to be a good approximation to the experimental distribution. In the case of a dominant rear stagnation point, for a lack of anything better, the inviscid velocity is linearly extrapolated from 95% length to the trailing edge as outlined above. Although corrections may improve the approximation to the experimental pressure distribution, such corrections are not done here in order to conserve computer time during optimization runs which may involve dozens of drag evaluations.

Boundary Layer Development. Once the pressure distribution impressed on the body surface is known, it is possible then to proceed with the boundary layer computation. A numerical procedure due to Cebeci, Smith, and Wang [7] computes planar/axisymmetric, laminar/turbulent, incompressible/compressible boundary layers using a variable-grid finite-difference method; the computer algorithm is called "Program E7ET." Our concern here is the axisymmetric, laminar and turbulent, incompressible problem. The method of transition is left to a later paragraph. The method retains transverse curvature effects which may be important for axisymmetric bodies with thick boundary layers. A two-layer eddy viscosity model is used for the turbulent boundary layer. Both laminar and turbulent separation are based on the zero skin-friction criterion. Zero or negative skin friction is inferred when the numerical iterative scheme diverges at a given streamwise location.

The coordinate system and basic notation are shown in Figure 3, following Cebeci [7]. There is some redundancy in notation for two reasons. In the past the notation for inviscid flows and boundary layer flows emerged separately. Also, computer printed output, with its lack of lower case symbols, has forced some changes in notation. To compute
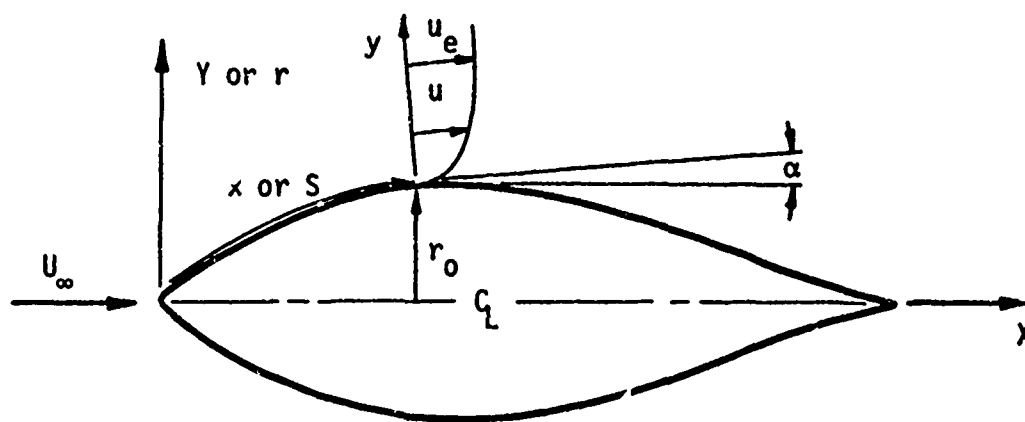
Figure 3. Coordinate System and
Basic Notation.

Indicated δ for
$u/u_e = .995$

Data from Reference 7, Part II

$\epsilon = \epsilon_0$

$\epsilon = \epsilon_1$

Normal Distance y
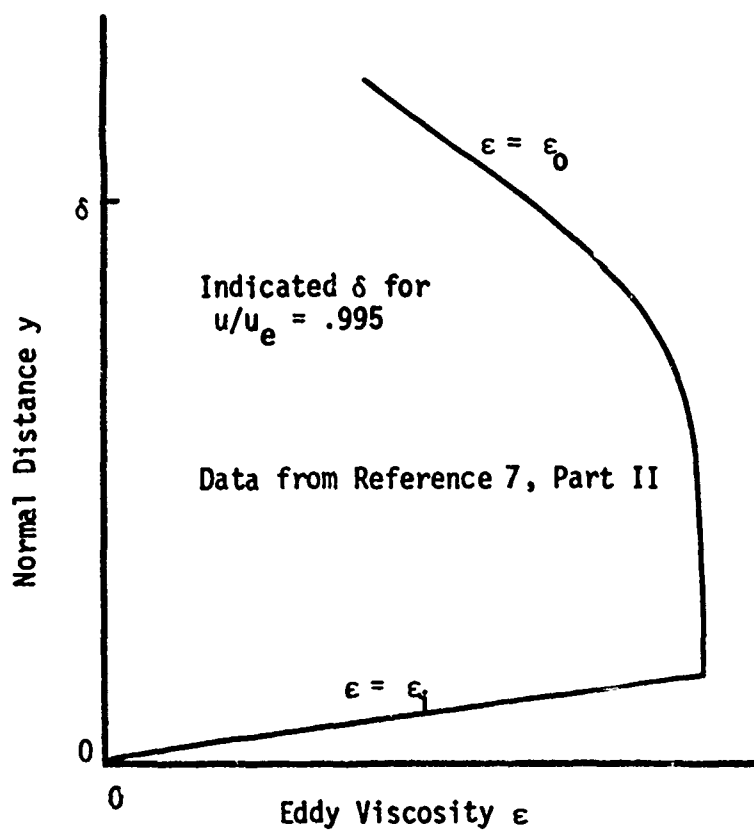
Eddy Viscosity ϵ

Figure 4. Typical Eddy Viscosity Distribution
Across Boundary Layer.

inviscid flows and to describe the body geometry, the X-Y coordinates are used; the reference velocity U_∞ is parallel to the X-axis. Boundary layers are computed using the curvilinear coordinate system with x (or S) aligned along a surface meridian and y normal to the surface. It is convenient also to use a radial coordinate $r = r_0 + y \cos \alpha$, where r_0 is the body radius and α is the angle between the surface tangent and the center line in a meridional plane. At any x location on the body surface, there is a boundary layer velocity profile $u(x, y)$ and a velocity at the edge of the boundary layer $u_e(x)$. For incompressible flow knowledge of the inviscid pressure implies that the velocity $u_e(x)$ is also known. Thus, the terms "pressure distribution" and "velocity distribution" are used interchangeably.

For incompressible axisymmetric flow the boundary layer equations [7] may be written as follows:

Continuity

$$\frac{\partial}{\partial x} r(\rho u + \overline{\rho'v'}) + \frac{\partial}{\partial y} r(\rho v + \overline{\rho'v'}) = 0 \tag{2.2}$$

Momentum

$$\rho u \frac{\partial u}{\partial x} + (\rho v + \overline{\rho'v'})\frac{\partial u}{\partial y} = -\frac{dp}{dx} + \frac{1}{r}\frac{\partial}{\partial y} r[\mu\frac{\partial u}{\partial y} - \overline{\rho v'u'}] \tag{2.3}$$

where ρ is the fluid density, μ is the fluid dynamic viscosity, p is the pressure impressed on the boundary layer, and v is the y-component of the boundary layer velocity. Terms containing primes and overbars, e.g., $\overline{\rho'u'}$, are time-averaged fluctuating quantities, and other notation is defined above and in Figure 3.

The boundary conditions for equations (2.2) and (2.3) are

$$u(x,0) = 0 \quad \text{(no slip)} \tag{2.4a}$$

$$v(x,0) = 0 \quad \text{(no mass transfer)} \tag{2.4b}$$

$$\lim_{y \to \infty} u(x,y) = u_e(x) \tag{2.4c}$$

The so-called Reynolds shear stress term $\overline{-u'v'}$ in the momentum equation is related to mean flow quantities using the eddy viscosity concept

$$\varepsilon \equiv \frac{\overline{u'v'}}{\frac{\partial u}{\partial y}} \tag{2.5}$$

where ε is the "eddy viscosity," which is represented by a two-layer model [7]. The eddy viscosity ε_i for the inner region, i.e., the boundary layer region near the wall, is based on Prandtl's mixing-length theory, so that

$$\varepsilon_i = \ell^2 \left| \frac{\partial u}{\partial y} \right| \tag{2.6}$$

where ℓ is the mixing length defined as

$$\ell = k_1 y \left[1 - \exp \left[-\frac{y}{26\nu} \left(\frac{\tau_w}{\rho} + \frac{dp}{dx} \frac{y}{\rho} \right)^{\frac{1}{2}} \right] \right] \tag{2.7}$$

where ν is the fluid kinematic viscosity, τ_w is the wall shear stress, and k_1 is a constant equal to 0.4. The outer region eddy viscosity ε_0 is given by

$$\varepsilon_0 = k_2 \, u_e \, \delta^* \, \gamma \tag{2.8}$$

which depends only on x except for the presence of the intermittency factor γ, where

$$\gamma = \left[1 + 5.5\left(\frac{y}{\delta}\right)\right]^{-1} \tag{2.9}$$

and where δ is the boundary layer thickness defined as the y-distance for which $u/u_e \doteq .995$. The quantity δ^* in equation (2.8) is a displacement thickness which for the eddy viscosity model is defined as

$$\delta^* = \int_0^\infty \left(1 - \frac{u}{u_e}\right) dy \tag{2.10}$$

The constant k_2 is equal to 0.0168 when the boundary layer thickness δ is defined as the y-distance for which $u/u_e = .995$. Hence, from the wall outward the eddy viscosity ε is equal to ε_i until the magnitude of ε_i equals ε_0 from which point outward ε equals ε_0. A typical plot of the eddy viscosity ε across a boundary layer is shown in Figure 4.

The purpose for setting down the complex expressions for the eddy viscosity is to bring out the implicit and empirical nature of the model. It is apparent that the boundary layer equations (2.2) and (2.3) cannot be solved until the eddy viscosity relations (2.6), (2.7), (2.8), (2.9), and (2.10) are all known. It is also apparent that equations (2.6) through (2.10) require the solution of the boundary layer before they can be evaluated. At least for this reason an iterative scheme is required to solve the turbulent boundary layer.

Using two transformations [7], the boundary layer equations (2.2) and (2.3) together with the boundary conditions (2.4), are non-dimensionalized and reduced to an ordinary third-order nonlinear differential equation with transformed boundary conditions. The equation is solved by an implicit finite-difference method using variable grid spacing in both the streamwise and normal coordinates. Convergence of solution, i.e., of the laminar or turbulent velocity profile, at each streamwise station is based on convergence of the transformed wall shear stress.

Transition Prediction. The state-of-the-art of predicting transition of axisymmetric boundary layers is unclear at the present time. An

example of the conflicting evidence and a conjectural explanation is given in Section 2.4. From the point of view of modeling and simulation, transition should begin at the point where laminar flow modeling ceases to be adequate in some sense. In the present study transition is treated as a point phenomenon, that is, as the switch which "turns on" turbulence.

The transition model used here is a composite of a planar-flow empirical correlation due to Michel ("Michel curve") and a rather sophisticated, semi-empirical, planar-flow correlation ("e-to-the-nine-curve") due to Smith and his co-workers [4, 5]. The composite correlation, the "Michel-e^9 correlation," is shown in Figure 5. The composite correlation is based on airfoil data taken from free-flight and low-turbulence wind tunnel tests. The correlation is between the momentum thickness Reynolds number at transition $R_\theta]_{tr}$ and the running surface-length Reynolds number at transition $R_S]_{tr}$, where in Figure 5 θ is the momentum thickness, u_e is the local velocity at the edge of the boundary layer, S is the surface length, and ν is the fluid kinematic viscosity. Also shown is a typical R_θ versus R_S plot as computed by the boundary layer program described in this study. The recommended ranges for each curve are indicated in Figure 5 [4].

It is believed that the axisymmetric laminar boundary layer parameters used to predict transition should be Mangler-transformed [6] to their equivalent planar-flow values before applying the transition correlations. However, the Mangler transformation is explicit only to within an "arbitrary" constant which is not specified in the transformation itself. The arbitrary constant has a direct bearing on the transformed boundary layer parameter values and hence affects the transition prediction directly. In a few cases that were checked no characteristic constant was found that consistently improved the transition prediction as inferred from drag data; indeed, in some cases, the Mangler transformation was grossly detrimental to drag prediction compared to the non-transformed values.

The correlation curve itself is based on the planar-flow definition of θ, which for incompressible flow is

$$\theta = \int_0^\infty \frac{u}{u_e} \left(1 - \frac{u}{u_e}\right) dy \qquad (2.11)$$
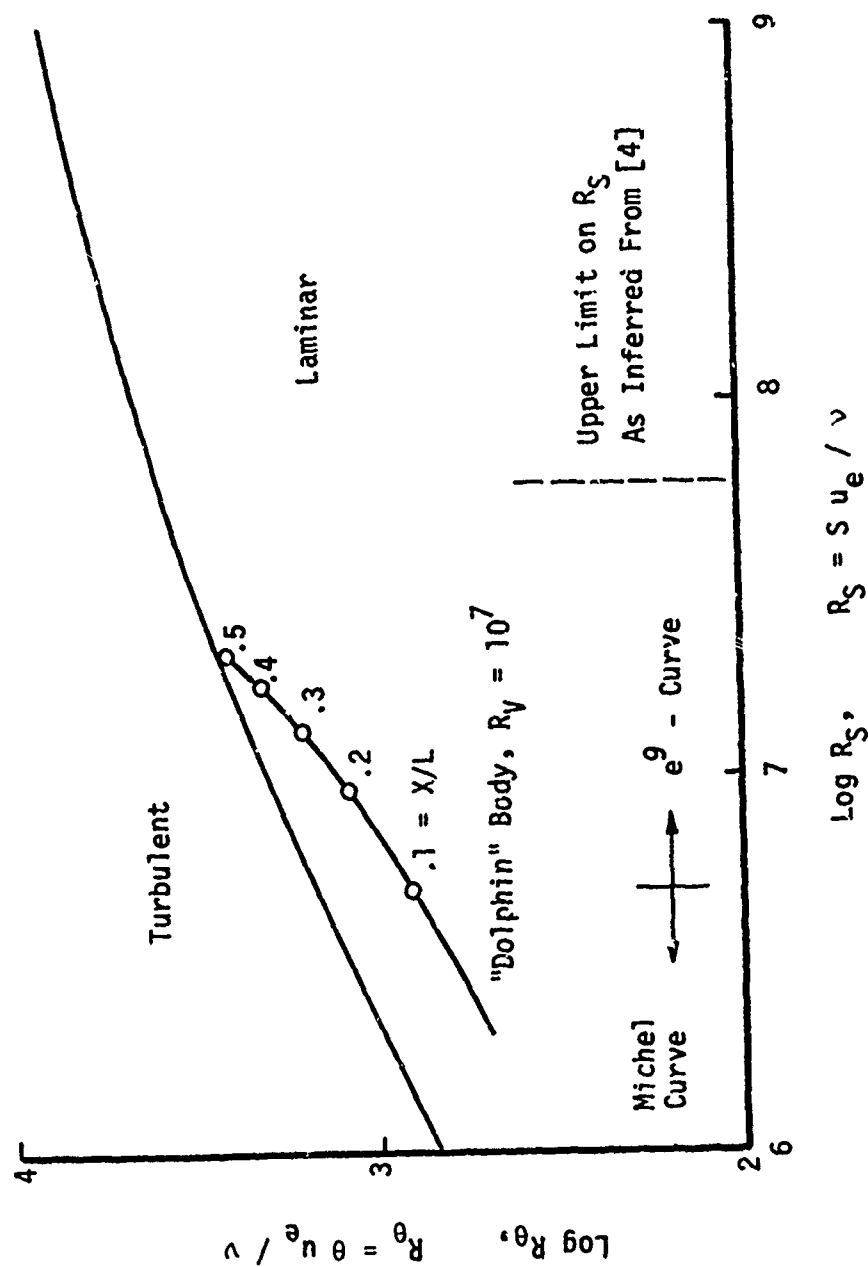
Figure 5. Michel-e^9 Correlation for Transition Prediction.

while the axisymmetric definition of θ used to predict transition is

$$\theta = \int_0^\infty \frac{r}{r_0} \frac{u}{u_e} \left(1 - \frac{u}{u_e}\right) dy \qquad (2.12)$$

where r is the radial coordinate of a point in the boundary layer and r_0 is the wall radius. However, for laminar boundary layers the value of r/r_0 is nearly 1, so that the difference in the definitions (2.11) and (2.12) should not be significant.

Occasionally the situation arises in which laminar separation occurs before transition is indicated by the Michel-e[9] correlation curve. Laminar separation is inferred when the numerical iteration scheme diverges. In this situation turbulent reattachment of the boundary layer is assumed. Thus, as far as the boundary layer computation is concerned, laminar separation is identical to transition.

Number and Distribution of Body Points.   It is appropriate to describe how the body shape Y(X), which in general may exist as an engineering drawing or as an analytic function, is translated into a table of points X_i, $Y(X_i)$, i = 1, ..., NN. This is not a trivial task since both the Douglas-Neumann method and the boundary layer program E7ET are sensitive to the number and distribution of body points. For example, the Douglas-Neumann method requires a close spacing of body points where the body slope or curvature is changing rapidly. Also, program E7ET requires a close spacing of body points where quantities such as velocity and skin friction are changing rapidly.

For streamlined bodies, these regions of rapid change occur near the leading edge and in the vicinity of the transition point. Since the transition point is not known a priori, the points are closely spaced in an expanding fashion near the leading edge and uniformly spaced elsewhere. It is emphasized that the spacing is established on the surface meridian, not on the axis of symmetry.

A partial distribution of points along a body surface is shown in Figure 6. A procedure which has been found to work well in practice is
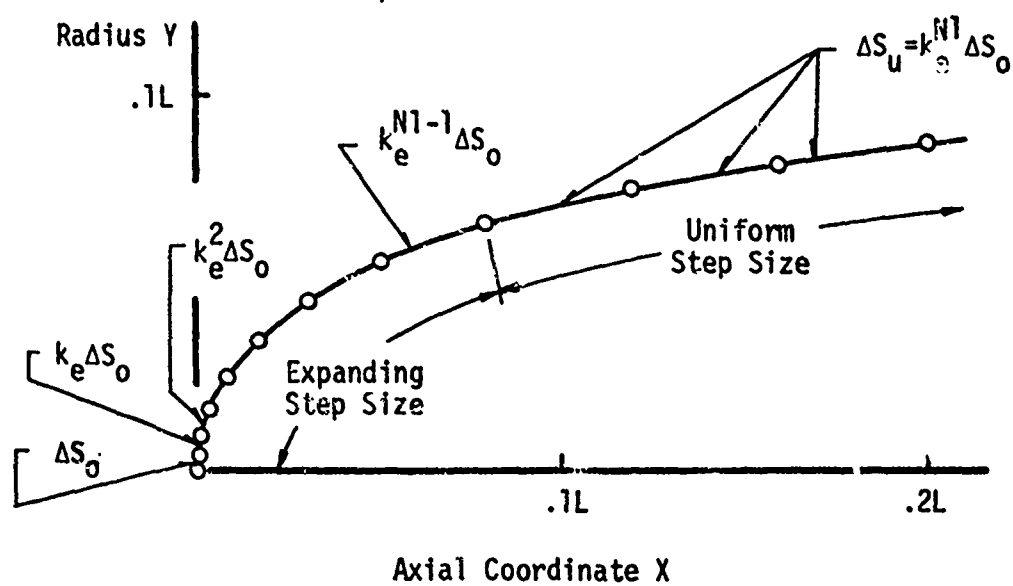
Figure 6. Typical Body Point Distribution.

to distribute in an expanding fashion about one-fourth of the NN points in the first ten to fifteen percent of the total surface arc-length S_{Total}. The remaining points are distributed uniformly over the last 85 to 90 percent of S_{Total}. Near the leading edge, each step size is equal to the preceding value multiplied by the expansion factor k_e. Thus, the initial step size is ΔS_0, the second is $k_e \Delta S_0$, the third is $k_e^2 \Delta S_0$, etc. The accumulated arc-length is the sum of the three terms. The initial step size ΔS_0 and the expansion factor k_e are found by solving simultaneously the following two equations:

$$\Delta S_0 (1 + k_e + k_e^2 + \dots + k_e^{N1-1}) = (FPC)(S_{Total}) \qquad (2.13a)$$

$$\Delta S_0 \, k_e^{N1} = \Delta S_u \qquad (2.13b)$$

where N1 is the number of steps to be included in the first FPC fractional part of S_{Total}. Equation (2.13a) insures that the accumulated arc-length of the first N1 steps is equal to the desired fractional part of S_{Total}. Equation (2.13b) requires that the first uniform step be equal to the previous step times the expansion factor k_e. The uniform step size ΔS_u is specified by

$$\Delta S_u = \frac{1 - FPC}{NN - 1 - N1} S_{Total} \qquad (2.14)$$

Two sets of typical values are given below:

1. Number of body points NN = 32

    FPC = 0.10

    N1 = 32/4 = 8

    ΔS_u = .03913 S_{Total}

$$\Delta S_0 = .00387 \ S_{Total}$$

$$k_e = 1.33524$$

2. Number of body points NN = 101

$$FPC = 0.15$$

$$N1 = 101/4 \approx 26$$

$$\Delta S_u = .01134 \ S_{Total}$$

$$\Delta S_o = .00299 \ S_{Total}$$

$$k_e = 1.05481$$

These two sets of values are used throughout the entire study.

The set of NN body points is used only within the Douglas-Neumann method which computes the inviscid velocities only at points midway between succeeding pairs of the original NN body points. The boundary layer is computed only at the "midpoints," referred to as "body stations," by program E/ET. The body stations are numbered starting from zero so that the last body station number NSTA is numerically equal to NN - 2. Throughout this study the term "30-station" or "99-station" solution refers to a solution obtained using NN = 32 or 101 body points, respectively.

Finally, the algorithm requires 60 seconds for 30 stations (NN = 32) to 180 seconds for 99 stations (NN = 101) of CDC 6500 computer time to compute one drag value. The 99-station solutions are more reliable; all drag values reported in this study are 99-station solutions. However, for an optimization run, during which dozens of drag computations may be performed, 30-station solutions are used in order to reduce computer costs. The "coarseness" of the 30-station numerical grid introduces a source of error which may slightly distort the relative trends encountered during a search for an optimum body shape. It is believed, however, that the distortion is minor and that overall results are not affected significantly.

In the next section the procedure for computing drag is presented.

2.3 Computational Procedure for Computing Drag

With the computational tools outlined in Section 2.2, there are two methods immediately available for computing drag. One method uses certain flow parameters at the trailing edge of the body in a formula due to Young [12]. The second method involves integrating the drag (axial) components of the forces acting over the body surface, these being pressure and skin friction. Both methods require an accurate prediction of the boundary layer and the transition location. The two methods are discussed briefly below.

Drag by Young's Formula. Young developed a formula relating total drag to certain flow parameters at the trailing edge of the body. The formula in its non-dimensional form is

$$C_D = \frac{\text{Drag}}{\frac{1}{2}\rho\, U_\infty^2\, V^{\frac{2}{3}}} = \frac{4\pi}{V^{\frac{2}{3}}}\, r_0\, \theta \left(\frac{u_e}{U_\infty} \right)^{\frac{H+5}{2}} \Bigg]_{T.E.} \qquad (2.15)$$

where C_D is the drag coefficient, ρ is the fluid density, U_∞ is the reference velocity, V is the body volume so that $V^{\frac{2}{3}}$ is the reference area, r_0 is the body radius, θ is the momentum thickness as defined in equation (2.12), u_e is the velocity at the edge of the boundary layer, and H is the shape factor defined as

$$H = \frac{\delta^*}{\theta} \qquad (2.16)$$

where θ is defined in equation (2.12), and δ^* is the displacement thickness which for equation (2.15) is defined as

$$\delta^* = \int_0^\infty \frac{r}{r_0} \left(1 - \frac{u}{u_e} \right) dy \qquad (2.17)$$

for incompressible flow. The definitions of δ^*, θ, and H are obtained during the derivation of the axisymmetric form of the momentum integral equation on which Young's formula is based. In equation (2.15) the subscript T.E. denotes quantities at the trailing edge of the body. It is noted that r_o, θ, u_e, and H are functions of the surface length x so that the drag coefficient C_D could be treated as $C_D(x)$, a function of x. Such a treatment is not implied in Young's derivation, although the behavior of $C_D(x)$ is of interest. The derivation of Young's formula is given in Appendix B.

Drag by Integration of Surface Forces. This method is simple in concept but difficult to apply in practice. Essentially, once the pressure and skin friction distributions are known over the entire body surface, an integration of the drag (axial) components should give the total drag. The integral is given as

$$\text{Drag} = \int_0^L (p - p_\infty)\, 2\pi Y \frac{dY}{dX}\, dX + \int_0^L \tau_w\, 2\pi Y\, dX \qquad (2.18)$$

or in its non-dimensional form as

$$C_D = \frac{\text{Drag}}{\frac{1}{2}\rho\, U_\infty^2\, V^{\frac{2}{3}}} = \frac{2\pi}{V^{\frac{2}{3}}} \int_0^L C_p\, Y \frac{dY}{dX}\, dX + \frac{2\pi}{V^{\frac{2}{3}}} \int_0^L C_f\, Y\, dX \qquad (2.19)$$

where the first and second integrals in (2.18) and (2.19) represent the contributions due to pressure and skin friction, respectively. The symbol p_∞ is the free-stream static pressure, p is the local pressure at the body surface, and C_p is the pressure coefficient defined as

$$C_p = \frac{p - p_\infty}{\frac{1}{2}\rho\, U_\infty^2} = 1 - \left(\frac{u_e}{U_\infty}\right)^2 \qquad (2.20)$$

for incompressible flow. Also C_f is the skin friction coefficient based on the reference velocity and is defined as

$$C_f = \frac{\tau_w}{\frac{1}{2}\rho\, U_\infty^2} \qquad (2.21)$$

Other notation is defined in previous sections.

The reason equation (2.18) or (2.19) is difficult to apply in practice is that the pressure over the body surface must be the experimental distribution, which is difficult to approximate numerically as discussed in Section 2.2. It appears that Young's method is less sensitive to errors in the pressure distribution than direct integration of the surface forces; hence Young's formula, equation (2.15), is used in the present study.

Drag Algorithm. The flow chart for computing drag in the present study is shown in Figure 7. The input consists of a characteristic Reynolds number $R_V = V^{\frac{1}{3}} U_\infty/\nu$ and a body shape $Y(X)$. A geometry table is generated using the procedures associated with equations (2.13) and (2.14) and illustrated in Figure 6. The actual numerical values in the geometry table are normalized to unit length or unit volume. For an optimization run 30-station solutions (NN = 32) are used; for detailed drag evaluations 99-station solutions (NN = 101) are used.

The velocity distribution along the body surface is computed using the Douglas-Neumann method. If a dominant rear stagnation point exists, then the inviscid velocity is modified by linear extrapolation from 95 percent axial length to the trailing edge.

The laminar and turbulent boundary layers are computed by program E7ET. Transition is predicted by the Michel-e[9] correlation or by laminar separation/turbulent reattachment, whichever occurs first.

Input: Reynolds Number R_V
           Body Shape $Y(X)$

Start ──────────▶ Generate Table of Body Points
                  X_i, $Y(X_i)$, i=1, ..., NN

Compute Inviscid Velocity by
Douglas-Neumann Method

Modify Velocity by
Linear Extrapolation
From 95% Length
◀── Yes ── Dominant Rear
           Stagnation Point?

No

Compute Boundary Layer by E7ET;
Transition by Michel-e^9 or Laminar
Separation/Turbulent Reattachment,
Whichever Occurs First

Compute Drag by
Young's Formula,
Equation (2.15)
◀── No ── Turbulent
          Separation?

Yes

Stop

Figure 7. Flow Chart For Drag Computation.

If turbulent boundary layer separation occurs, as indicated by solution divergence, the pro*r m aborts and no drag calculation is made. During an optimization run, turbulent boundary layer separation is treated as a constraint violation. The various constraints are discussed in Chapter 3.

If there is no separation, or more generally, if there are no constraint violations (details in Chapter 3), then the drag coefficient is computed using Young's formula, equation (2.15).

In the next section the characteristics of the drag model as described here will be demonstrated by comparing predictions with some of the data available in the literature.

2.4 Characteristics of the Drag Model

In this section comparisons are made between predicted and experimental drag coefficients using the drag model indicated in Figure 7. Transition data comparisons are also made. Rather than presenting a comprehensive study of the experimental data available in the literature, it is the intent here to demonstrate the characteristics of the drag model used in the present study. A more comprehensive comparison of predicted and experimental drag values is found in Reference 4.

Drag Prediction for the Laminar Flow "Dolphin" Body. A reasonable approximation to the "Dolphin" Body [2] is shown in Figure 8 along with the inviscid velocity distribution. A typical transition location is indicated. The long, slender tailboom is cut off at about two-thirds of the actual body length. The experimental data were obtained from gravity-powered accelerating drop tests in the Pacific Ocean at speeds up to 62 knots. Figure 9 shows the predicted and experimental drag coefficients; a standard torpedo curve [2] is also included for comparison. The experimental data has been corrected to hull drag values by subtracting out the drag due to stabilizing fins and the tailboom [2]. The agreement between predicted and experimental values is good, with the prediction tending to be optimistic. The role of the laminar boundary
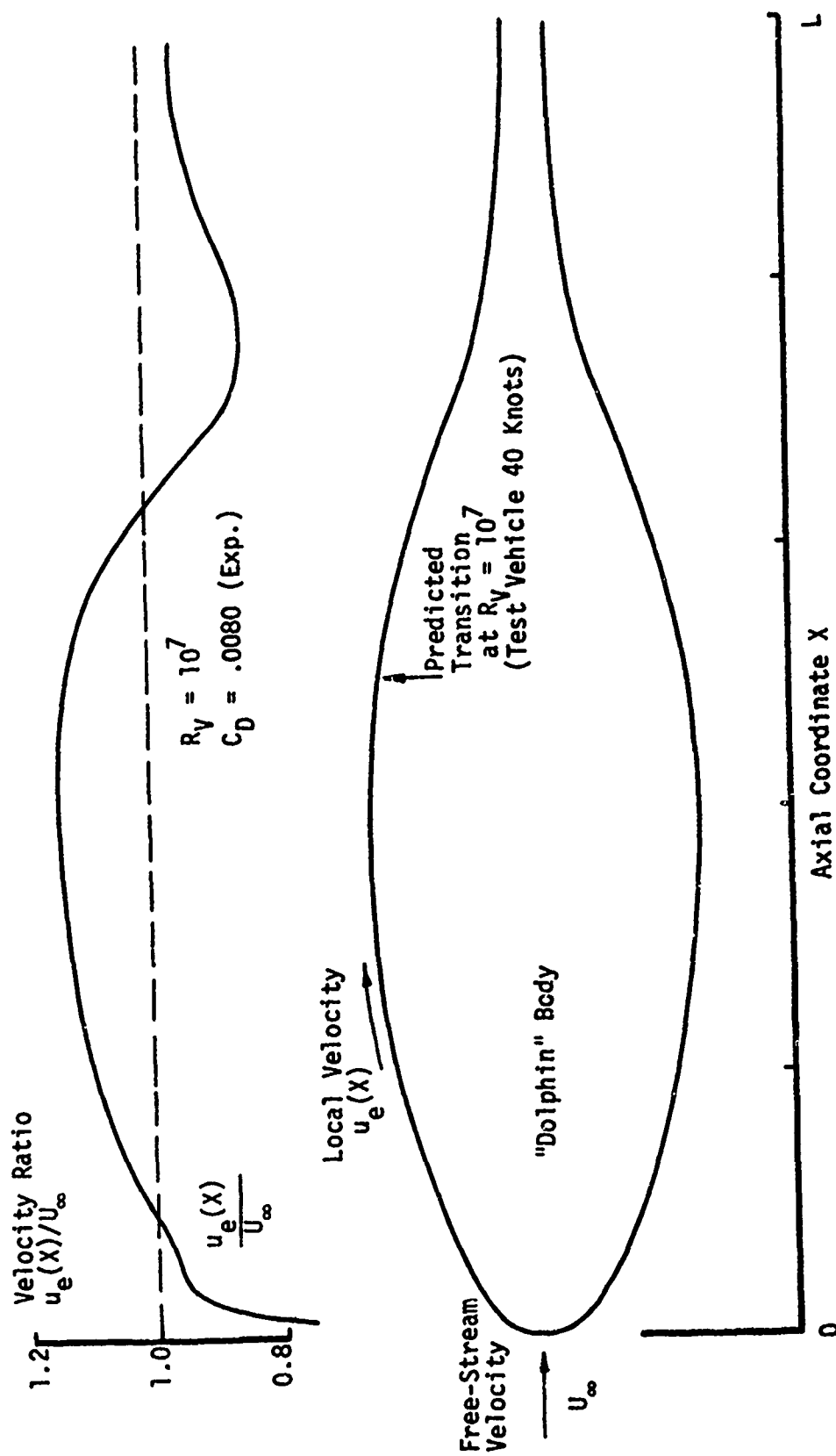
Figure 8. "Dolphin" Body with Velocity Distribution.
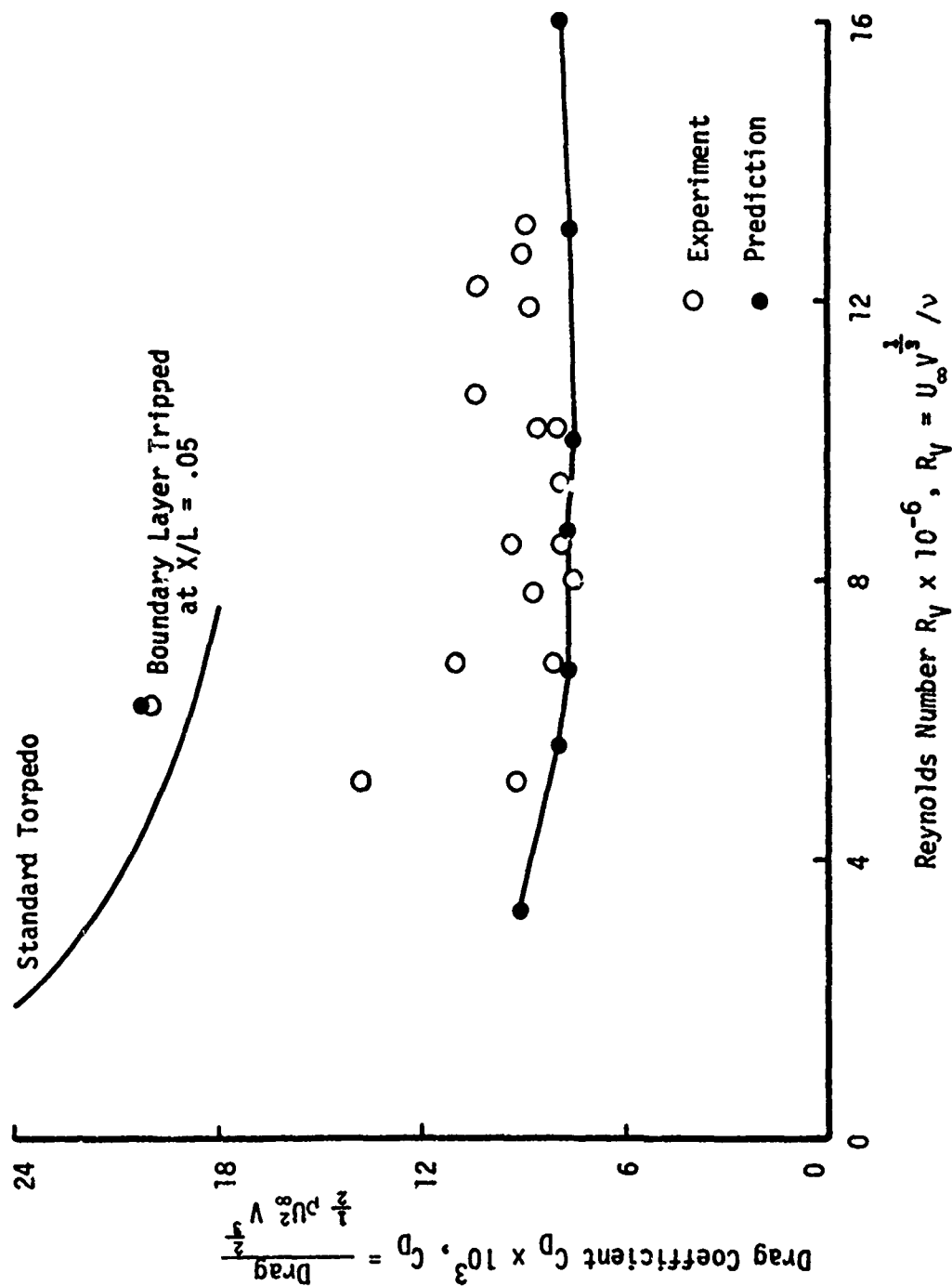
Figure 9. Predicted and Experimental Drag Coefficients for the "Dolphin."

layer in drag reduction is demonstrated both by prediction and experimentally by tripping the boundary layer at X/L equal 0.05. The drag coefficient is comparable to that of the standard torpedo as shown in Figure 9. These data demonstrate that substantial amounts of laminar flow are possible at high speeds (60 knots) in the ocean environment and that the drag model used in this study is capable of predicting such behavior reasonably well.

It is also of interest to observe the trend of C_D computed at various stations along the body surface. A typical $C_D(x)$ trend for the "Dolphin" body is shown in Figure 10. The drag coefficient C_D increases monotonically to the trailing edge.

Drag Prediction for Model 4165 of Series 58. The Series 58 study has produced a recommended best shape which is very nearly the same as Model 4165 of that series [3]. This body and its inviscid velocity distribution are shown in Figure 11. This body has a dominant rear stagnation point so that the drag is computed using the modified velocity distribution shown in the same figure; details of this modifying procedure are given in Section 2.3. For this case the boundary layer is tripped at X/L = .05. The drag prediction is for one Reynolds number, that corresponding to the highest test velocity. The drag coefficient is computed at various stations along the surface of the body; the trend is shown in Figure 12 along with the experimental drag value. As for the "Dolphin" body, C_D increases monotonically to the trailing edge.

The predicted value exceeds the experimental value by nine percent. The predicted value happens to equal the experimental value at the location on the body where u_e/U_∞ is unity. Cebeci, using a modified definition of θ in Young's formula, equation (2.15), reports this behavior for a number of bodies including Model 4165 [4]. It might be inferred that the drag coefficient is to be computed at the body station nearest the trailing edge for which u_e/U_∞ is unity. For the "Dolphin," with its asymptotic velocity, "nearest" would be interpreted to mean "at." However, this idea has not been investigated; for the sake of consistency, the predicted drag value will be that computed at the trailing edge except as noted in the next paragraph.
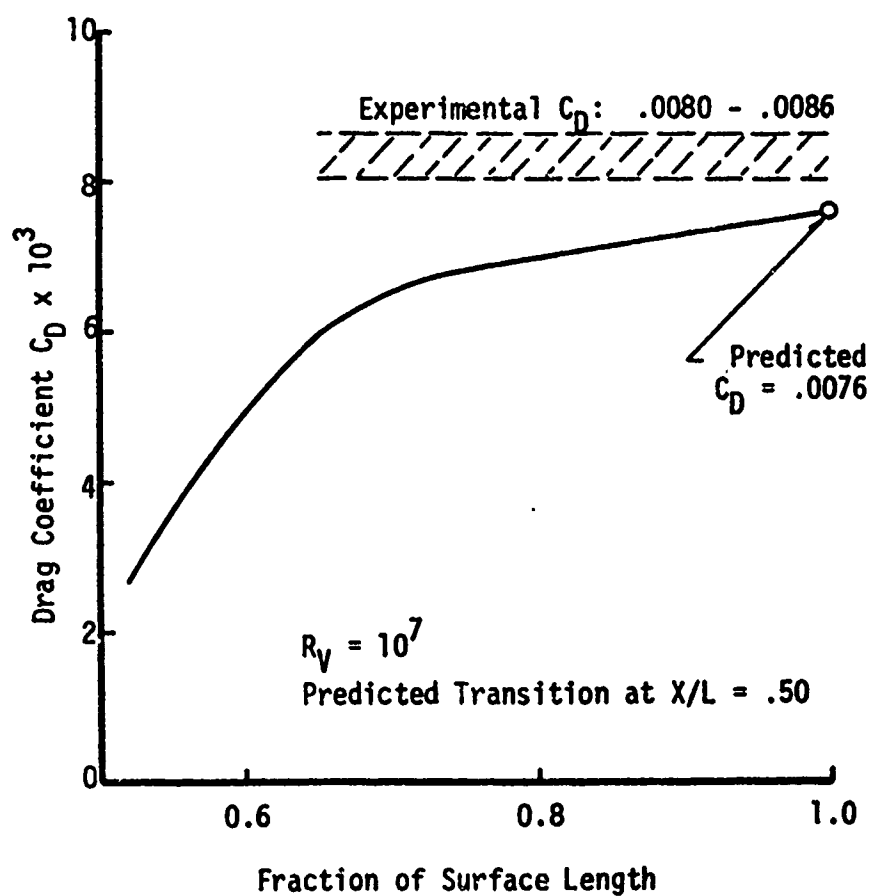
Figure 10. Variation in Predicted Drag Coefficient
Along Surface of "Dolphin."
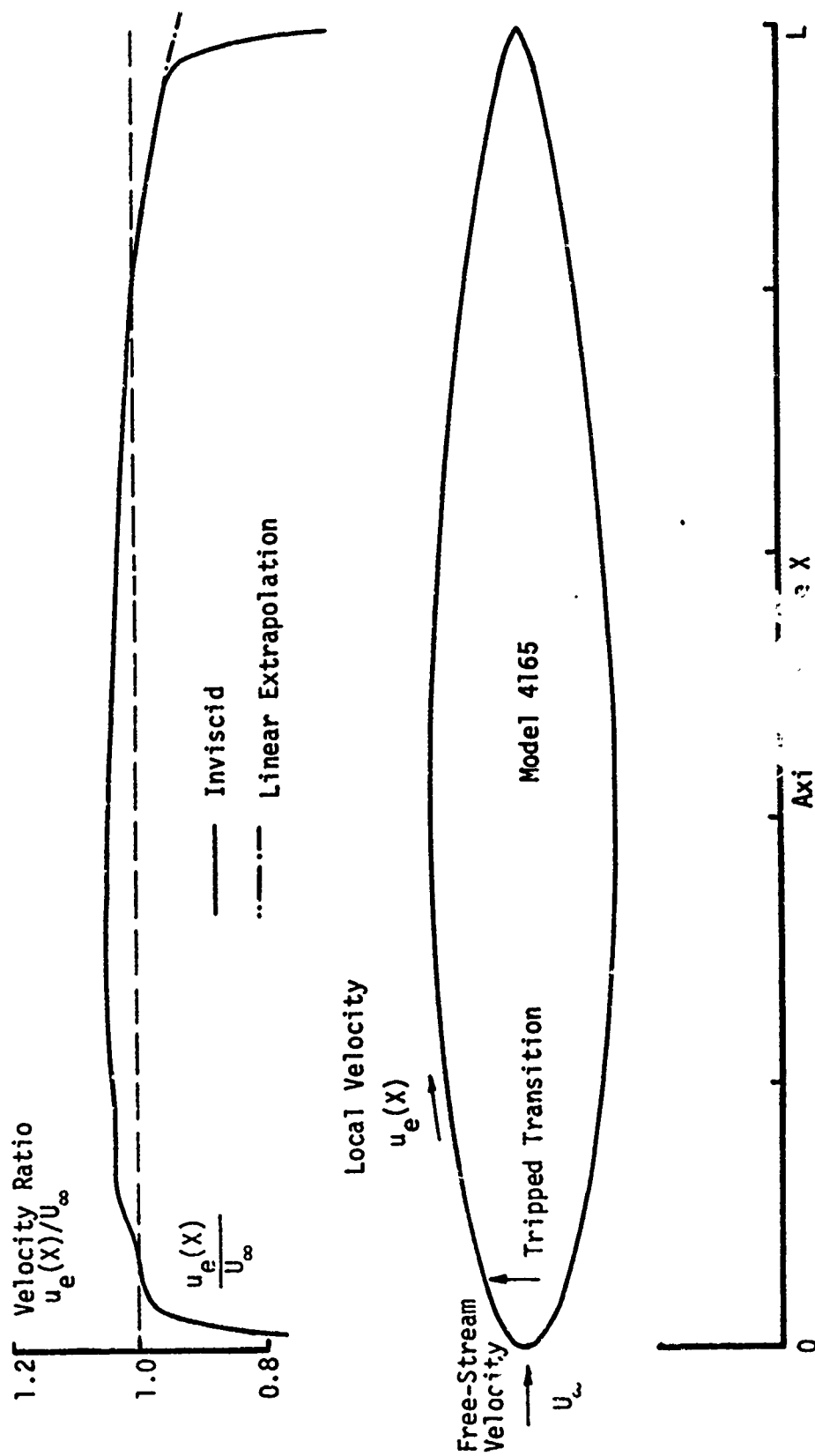
Figure 11. Model 4165 of Series 58 with Velocity Distribution.
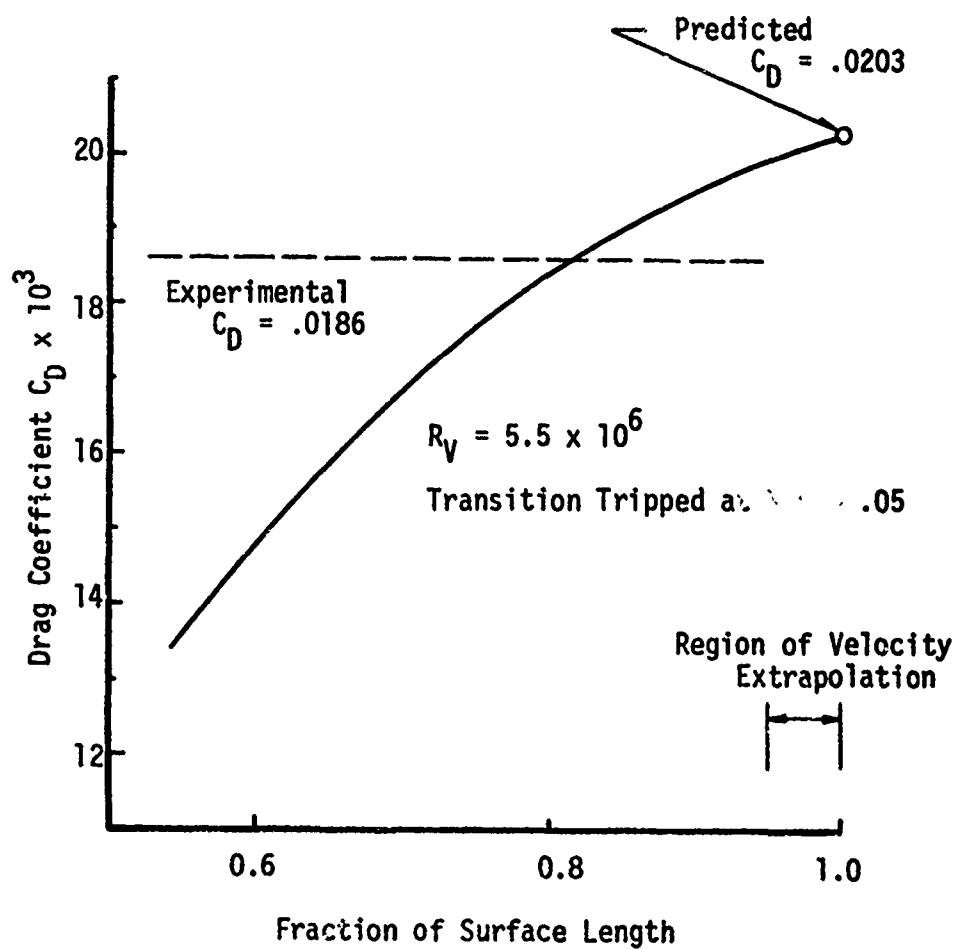
Figure 12. Variation in Predicted Drag Coefficient
            Along Surface of Model 4165.

Drag Prediction for Murphy Body A2, C4. This body consists of a rounded-nose forebody, a constant diameter midsection, and an inflected pointed tail [13]. The boundary layer is tripped using a porous strip about .03L in width. The downstream edge of the strip, located at X/L equal 0.5, is assumed to be the point of transition. The body is positioned about 0.27L inside the wind tunnel contraction cone so that the experimental and free-stream inviscid velocity distributions are different. The body shape and its velocity distributions are shown in Figure 13. Note that the experimental and inviscid velocity distributions are in good agreement near the trailing edge, away from the influence of the contraction cone. This substantiates to some degree the discussion in Section 2.2 in which it is assumed that the inviscid velocity is a fair approximation to the experimental velocity distribution which tends to the free stream value rather than rear stagnation.

The drag is computed at one Reynolds number, the C_D variation along the body surface is shown in Figure 14 for both pressure distributions along with the experimental range obtained by wake measurements. The C_D reaches a peak value at about S/S_{Total} equal 0.95 and then plunges rapidly. When such behavior occurs, it is assumed that the peak value is the proper one to use, the rapid plunging apparently indicating a breakdown in the method. No attempt is made here to investigate the underlying reasons for this behavior. The Douglas-Neumann velocity distribution yields a higher predicted drag than that obtained when using the experimental distribution, the difference due mainly to the different pressure gradients over the forebody.

Both predicted values are in reasonable agreement with the experimental range; the predicted values are 1.8% higher and 5.4% lower than the experimental mean value.

Transition Prediction for an Ellipsoid. Granville has reported the results of six different methods of transition prediction for axisymmetric bodies using three experimental pressure distributions on an ellipsoid with a fineness ratio (length/maximum diameter) of nine [14]. The different pressure distributions are obtained by placing the ellipsoid at various positions inside the wind tunnel contraction cone. For these
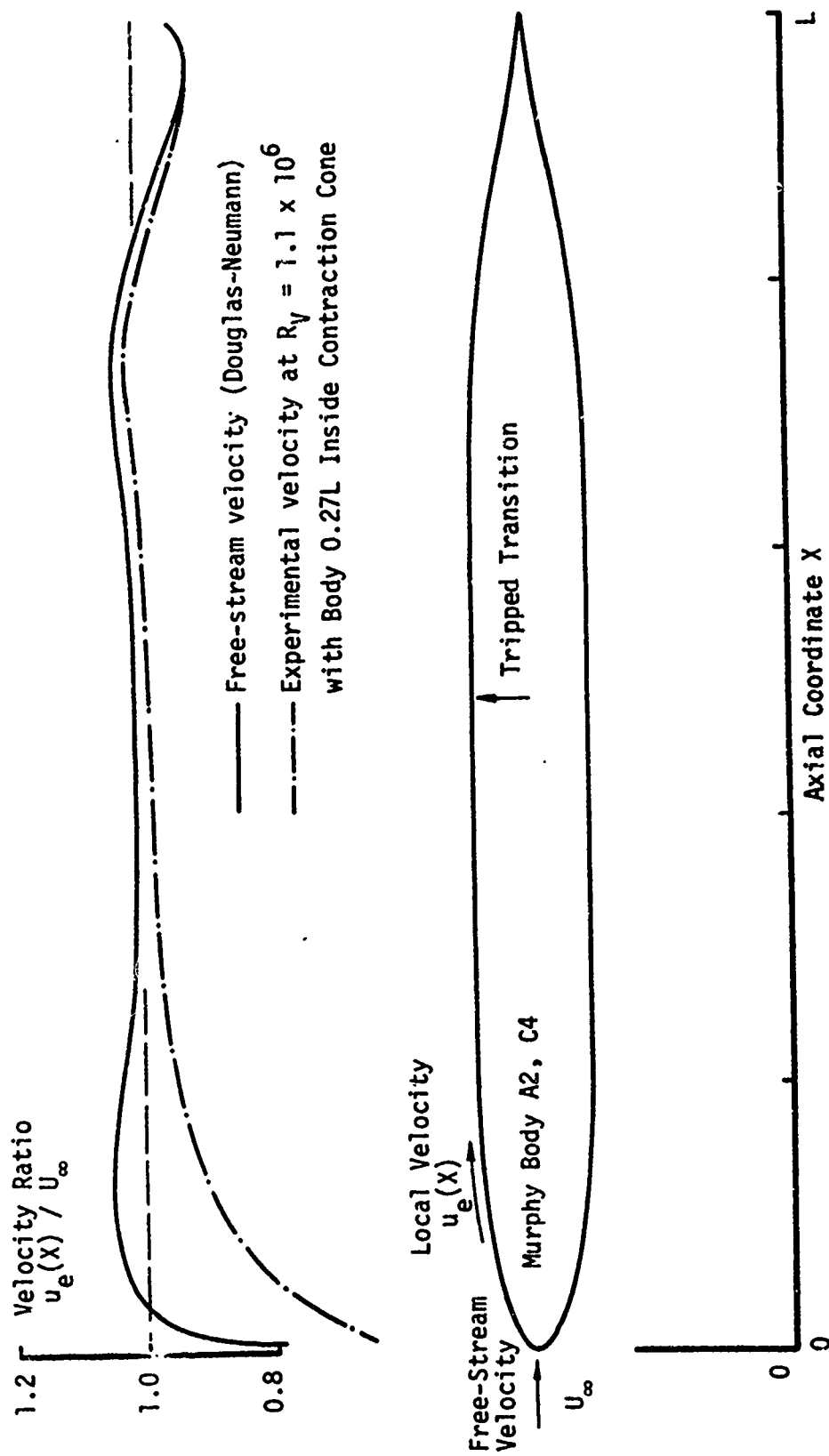
Figure 13. Murphy Body A2, C4 with Two Velocity Distributions.
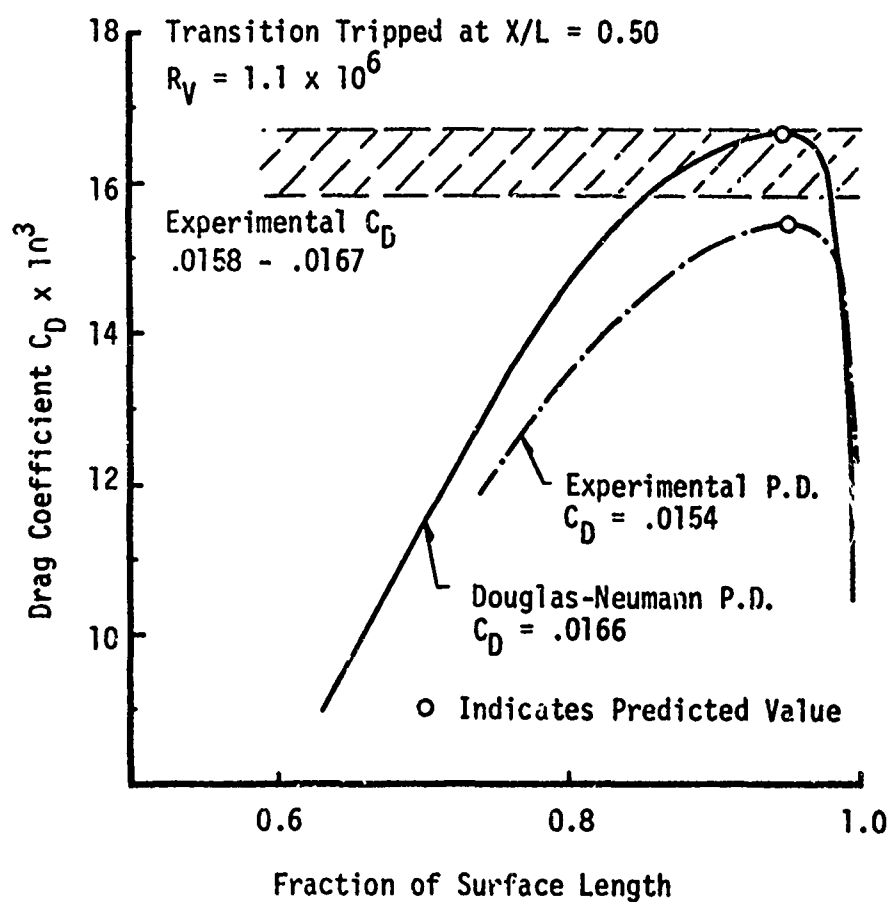
Figure 14. Variation in Predicted Drag Coefficient
Along Surface of Murphy Body A2, C4.

tests one turbulence burst per second is taken as the beginning of transition; the bursts are detected by pressure taps in the body surface.

The ellipsoid and two of the three experimental velocity distributions are shown in Figure 15. The change in transition location as a function of Reynolds number is shown in Figure 16 for both velocity distributions. It is readily apparent that the Michel-e[9] correlation prediction does not even resemble the trend of the experimental data; in fact, the correlation predicts nearly the same transition location under all test conditions.

The apparent contradiction between the successful "Dolphin" drag predictions, which include transition prediction, and the failure of the correlation for the ellipsoid has lead to a questioning of what is meant by "transition" in the context of drag prediction.

For drag prediction the transition point must represent the streamwise location on the body after which laminar flow modeling is no longer adequate. It is conjectured here that the acoustical definition for transition, i.e., one turbulence burst per second, may not be particularly relevant for predicting the location at which the boundary layer model should "switch" from laminar to fully turbulent. A recent experimental study [15] gives some support to this idea. The study produces a correlation among the average bursting frequency $\bar{f}$, the mainstream velocity u_e, and the displacement thickness δ^* using data from fully developed turbulent boundary layers along a flat wind tunnel wall; the correlation is of the form $\bar{f} = (\text{constant})(u_e)/(\delta^*)$. Although the correlation may not be directly applicable to axisymmetric boundary layers with pressure gradients, it seems reasonable that the idea of characterizing a turbulent boundary layer by using a correlated bursting frequency, as opposed to a fixed frequency, should carry over to the axisymmetric case.

2.5 Closing Comments about the Drag Model

The drag model as described here appears to be reasonably realistic. The drag predictions may be either optimistic or pessimistic, apparently
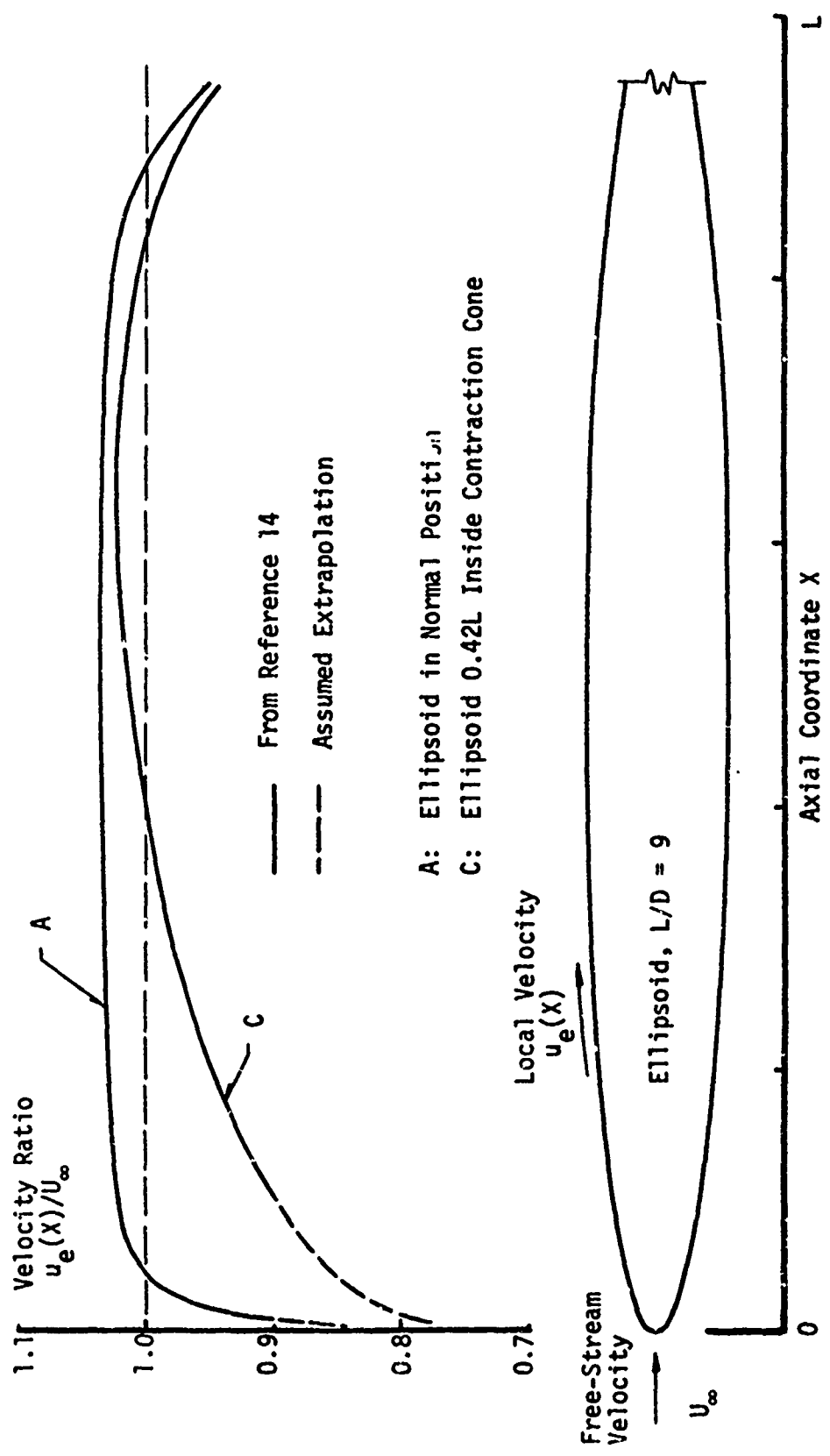
Figure 15. Experimental Velocity Distributions for an Ellipsoid in a Contraction Cone.
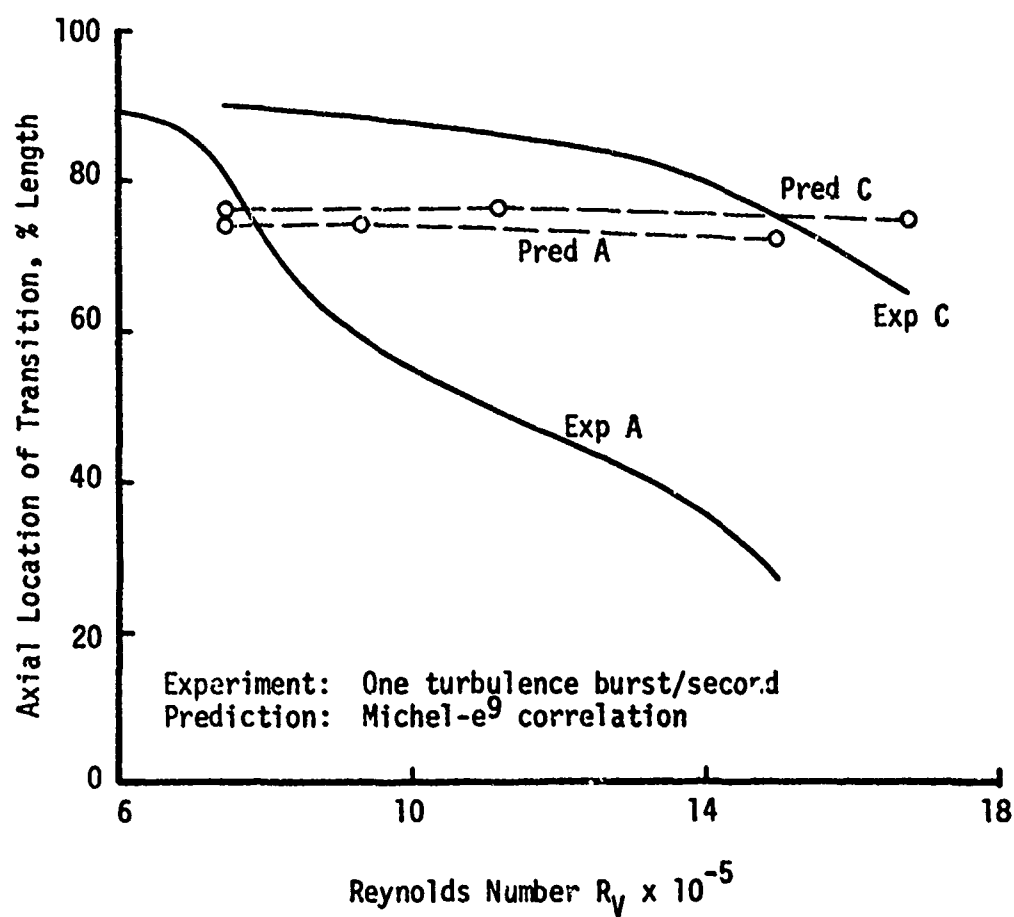
Figure 16.   Experimental and Predicted Transition
for Ellipsoid Shown in Figure 15.

depending on the body geometry being considered. For example, the predicted values for bodies with dominant rear stagnation points tend to be high, but for inflected aft-bodies the values tend to be low. It is felt that the method of transition prediction tends to be optimistic because of the somewhat optimistic drag predictions of the "Dolphin" body.

With the drag model established, the next chapter presents the formulation of the optimization problem.

CHAPTER 3

FORMULATION OF THE OPTIMIZATION PROBLEM

This chapter contains a brief discussion of two possible approaches to the optimization problem. The characteristics leading to the selected optimization approach are described; the constraints are discussed in detail. Two optimization methods used in this study are outlined.

3.1 Functional Optimization — Calculus of Variations

Once the reference Reynolds number R_v is fixed for the zero incidence uniform flow, the value of the drag coefficient C_D depends on the particular shape $Y(X)$ of the axisymmetric body; this may be expressed as

$$C_D = C_D[Y(X)] \tag{3.1}$$

where X is the axial coordinate. Equation (3.1) implies that the drag coefficient is to be minimized by manipulating the function $Y(X)$. Such a concept is the central idea of the calculus of variations [18, 19].

The simplicity of equation (3.1) is somewhat deceiving since variations must be performed not only on $Y(X)$ but on other dependent variables as well. This is apparent from equation (2.19) which is written here as

$$C_D = \frac{2\pi}{v^{\frac{2}{3}}} \int_0^L \left(C_p\, Y\, \frac{dY}{dX} + C_f\, Y \right) dX \tag{3.2}$$

where C_p and C_f are the pressure and skin friction coefficients defined by equations (2.20) and (2.21), respectively. Equation (3.2) shows that C_D is a function of $Y(X)$, $\frac{dY(X)}{dX}$, and the complicated quantities C_p and C_f which are governed by partial differential equations.

Certain conditions are imposed on the problem from the outset. The boundary conditions for $Y(X)$ are

$$Y(0) = 0 \tag{3.3a}$$

$$Y(L) = Y_{Terminal} \geq 0 \tag{3.3b}$$

where $Y_{Terminal}$ is not necessarily specified. The inequality constraint

$$Y(X) > 0, \quad 0 < X < L \tag{3.4}$$

must also be satisfied, as well as the equality constraint tacitly implied in equation (3.2), namely, a fixed volume

$$\int_0^L \left(\pi Y^2(X) \right) dX = V = \begin{array}{l} \text{Specified} \\ \text{Value} \end{array} \tag{3.5}$$

Furthermore, it may be necessary to treat the endpoint X equal L as a variable quantity. A more thorough analysis will reveal other constraints to be imposed on the problem. In addition, one must include the physics which constrain C_p and C_f.

If the problem can be properly formulated using the integral of performance defined in equation (3.2), along with the required constraints and boundary conditions, the result of the variational calculus is a set of necessary conditions which must be satisfied by the minimum drag shape. The set of necessary conditions, which relate the dependent variables Y, $\frac{dY}{dX}$, C_p, and C_f for a minimum drag body, do not explicitly

define the optimum body shape in terms of the independent variable X. However, the results may be used as a check to test any profile which is believed to be a local optimum.

Because of the complicated nature of C_p and C_f, both governed by partial differential equations, it is apparent that the drag integral, equation (3.2), cannot be formulated explicitly in terms of X, Y(X), and derivatives of Y(X). Without such a formulation, an explicit solution for the optimum Y(X) cannot be obtained, at least not from a calculus of variations analysis alone. For this reason this approach has not been pursued here.

An interesting alternate use of the calculus of variations has been successfully applied to nonseparating, maximum lift airfoils [16]. Rather than working with the blade geometry directly, an optimum pressure distribution for maximum lift is obtained from which the blade geometry is uniquely inferred. For axisymmetric design, this approach, called the "inverse design problem," cannot be used in its analytical form [17]; it has not been established that a unique axisymmetric body exists for a prescribed pressure distribution. Iterative numerical procedures have been attempted [17], but the inverse problem for axisymmetric bodies does not appear to be solved. Hence, this approach has not been pursued.

3.2 Parametric Optimization

If the calculus of variations approach were formulated in terms of X, Y(X), and derivatives of Y(X), and successfully solved, the solution for a fixed Reynolds number R_v would be an optimum profile Y**(X). For convenience it is assumed that Y**(X) is unique. Once the profile Y**(X) is known, either as an analytic function or as a table of numbers, it is possible to approximate it by a finite series of known functions $F_i(X)$, $i = 1, \ldots, N$, each multiplied by a constant. The series of known functions is assumed to be well behaved so that its properties, e.g., uniform convergence in the interval $0 \leq X \leq L$, do not require special consideration here.

The finite series approximation may be expressed as

$$Y^{**}(X) \simeq \sum_{i=1}^{N} a_i^{**} F_i(X) \qquad (3.6)$$

for $0 \leq X \leq L$, where N is the number of terms in the series and the $F_i(X)$, $i = 1, \ldots, N$, are known functions. The a_i^{**}, $i = 1, \ldots, N$, are the multiplicative constants which, when used with the functions $F_i(X)$, $i = 1, \ldots, N$, yield the best approximation to $Y^{**}(X)$ in some sense. For example, the a_i^{**}, $i = 1, \ldots, N$, in equation (3.6) may minimize the error defined by

$$E = \int_0^L \left(Y^{**}(X) - \sum_{i=1}^{N} a_i F_i(X) \right)^2 dX \qquad (3.7)$$

The optimum profile $Y^{**}(X)$ has associated with it a minimum drag coefficient C_D^{**}. The finite series on the right-hand side of equation (3.6) has associated with it a drag coefficient which can never be better than C_D^{**} since the finite series represents a perturbation away from the optimum $Y^{**}(X)$.

It is apparent that by fixing N and the $F_i(X)$, $i = 1, \ldots, N$, it is possible to manipulate the multiplicative constants a_i, $i = 1, \ldots, N$, also called "parameters," to produce an optimum profile

$$Y^{*}(X) = \sum_{i=1}^{N} a_i^{*} F_i(X) \qquad (3.8)$$

for which the drag coefficient C_D^{*} is a minimum. For convenience it is assumed here that the a_i^{*}, $i = 1, \ldots, N$, form a unique set. It is

expected that the set a_i*, $i = 1, ..., N$, in equation (3.8) is different from the set a_i**, $i = 1, ..., N$, in equation (3.6) since the former results from minimizing the drag coefficient C_D while the latter results from minimizing the error E exemplified by equation (3.7).

Implied in the above discussion is the fact that for a parametrically defined body the drag coefficient depends on the number N of terms in the series, the nature of the functions $F_i(X)$, $i = 1, ..., N$, used in the series, and the multiplicative constants a_i, $i = 1, ..., N$. This may be expressed as

$$C_D = C_D [N, a_i, F_i(X), i = 1, ..., N] \qquad (3.9)$$

This is true in particular for the minimum drag coefficient C_D* associated with $Y*(X)$ in equation (3.8), which is to emphasize the fact that the minimum drag profile $Y*(X)$ will be different for every value of N and every set of functions $F_i(X)$, $i = 1, ..., N$. Therefore, minimum drag shapes obtained using a formulation implied by equation (3.9) can be regarded only as the optimum of a restricted class of bodies with profiles defined by

$$Y(X) = \sum_{i=1}^{N} a_i F_i(X) \qquad (3.10)$$

where N and the $F_i(X)$, $i = 1, ..., N$, are fixed.

Although the parametric formulation necessarily introduces limitations on the optimization results, it has been adopted as the most feasible procedure for the drag minimization problem. Indeed, it appears that the functional approach, with its implicit necessary conditions, would require the use of an iterative search strategy of the general nature that we are considering here for the direct problem solution. A few comments about parametric optimization in general are given below.

Nearly all contemporary research in the area of optimization methods is addressed to the parametric problem rather than the functional problem

of the classical calculus of variations. These contemporary methods are usually reducible to a digital computer algorithm so that they are compatible with performance function models, e.g., drag models, which may already exist in digital computer program form. The standard measure of efficiency of parametric methods is the number of performance function evaluations required to obtain the optimal solution to within a given error tolerance. An alternate standard is to compare the performance function value obtained at the end of a fixed number of evaluations.

The parametric optimization methods may be broadly classified as unconstrained or constrained methods. The generally more efficient unconstrained methods are designed to be used in a parameter space without parameter boundaries (constraints). The generally less efficient constrained methods are designed to cope with parameter boundaries (constraints) which divide the parameter space into feasible and nonfeasible regions. The presence of nonfeasible regions may be due to physical considerations or limits of model validity, for example. To take advantage of the efficient unconstrained methods, it is common practice to convert a constrained problem into one which appears unconstrained by introducing "penalty functions." A penalty function artificially distorts the true performance function "surface," so that whenever a constraint boundary is violated, the performance function appears worse than the neighboring performance surface in the feasible region. The effect of the penalty function is to force the optimal solution into a feasible, hence acceptable, region. It is generally desirable to cast the optimization problem into one which is unconstrained so that a more efficient unconstrained method may be used.

A second broad classification for parametric optimization is gradient versus nongradient methods. This classification refers to the availability of analytical gradients of the form ∂(performance function)$/\partial(a_i)$, where the a_i, $i = 1, \ldots, N$, are the parameters to be manipulated. Depending on the optimization problem this information, i.e., the analytical partial derivatives, may or may not be available. The generally more efficient gradient methods use both the performance function and the local gradients to obtain the optimal solution. The

generally less efficient nongradient methods are designed to obtain the optimal solution using only the performance function itself. When the analytical gradients are not available, it is possible to approximate the gradients using finite differences. But it is usually more efficient to use a suitable nongradient method in this case rather than finite-difference approximations in conjunction with an efficient gradient method [20].

From the above discussion it may be concluded that problems which are unconstrained and have analytical gradients are to be more efficiently solved than other problems. There are other broad classifications of parametric optimization problems as well. For example, the performance function and/or the constraints may be linear or nonlinear functions of the parameters. The constraints may be expressed as equalities or inequalities and may involve algebraic, differential, and integral expressions. The constraints may be explicit or implicit in the parameters. The performance function and/or the parameters may be deterministic or stochastic. The performance function and/or parameters may be allowed only certain discrete values rather than continuously varying values. The parameter constraint boundaries may be convex or nonconvex. The optimal solution may or may not lie on a constraint boundary. Every optimization problem will involve some combination of these characteristics and perhaps others as well.

The parametric optimization method best suited to a particular problem depends, of course, on the characteristics of the performance function and constraints as mentioned above. The characteristics of the drag minimization problem are discussed in detail in the next section. The discussion leads to the optimization methods which are used in the present study.

3.3 Characteristics of the Drag Minimization Problem

The implication of the preceding two sections is that the drag minimization is to be cast as a parametric rather than a functional

optimization problem. This section examines in detail the characteristics of the drag model and the constraints in order to select appropriate methods (search strategies).

Model Characteristics. From the parametric optimization point of view the drag model is a performance function surface (response surface) in an N-dimensional space, where N is the number of independent parameters (variables) to be manipulated. The drag model, discussed in Chapter 2, is essentially a nonlinear numerical "black-box" whose input is a set of parameters a_i, i = 1, ..., N, and a Reynolds number, and whose output is a drag coefficient C_D. The parameters imply a unique shape Y(X) when N and F_i(X), i = 1, ..., N are specified in equation (3.10). Although it is possible to treat the drag prediction in a stochastic manner by using an error probability distribution, the model is treated as deterministic in the present study.

The model is a "black-box" in the sense that no analytic expression exists relating the drag coefficient C_D to the parameters a_i, i = 1, ..., N. Indeed, the numerical model performs the same function as an experiment, for example, in which a body, whose shape is Y(X) as implied by the a_i, i = 1, ..., N, is built and tested in a wind tunnel. For both the numerical model and the hypothetical experiment, the only information available for a given body at a fixed Reynolds number is its drag coefficient C_D. No analytical gradients $\partial C_D/\partial a_i$, i = 1, ..., N, are available in either case.

The numerical black-box, with its lack of analytical gradients, is to be used in conjunction with a nongradient (direct) search method. The procedure of approximating gradients with finite-differences has been rejected at the outset since it is believed that nongradient methods are more efficient with "nongradient problems" than finite-di   ng used with gradient methods [20].

Constraint Characteristics. Several statements can be made about the constraints at the outset. Constraints do exist for the drag minimization problem. The obvious ones include requirements for non-negative body dimensions, nonseparating flow, and a fixed Reynolds

number. Less obvious constraints for a particular class of bodies defined by equation (3.10) include requirements for a rounded nose and no inflection points on the forebody (section of body from nose to maximum diameter). These latter constraints are discussed in detail in Chapter 4 for two classes of bodies used in the present study. Other statements which can be made at the outset are that the parameters vary in a continuous manner and that the parameters are treated as deterministic, not stochastic.

The procedure for a performance function (PF) evaluation during an optimization run is to check for constraint violations and then to compute the PF if no violations occur. When violations do occur, no PF evaluation is made; indeed, the PF value may not exist in such cases, e.g., negative body dimensions. The nonseparating flow constraint presents a special problem; its violation is not known until a complete pass is made through the drag model. In an attempt to reduce computer time wasted due to the occurrence of a separated boundary layer, two additional constraints are checked preceding the costly boundary layer computation (75% of computer time). These constraints are designed to avoid pressure distributions which are probably conducive to boundary layer separation. These constraints are

1. Minimum pressure coefficient $C_{p_{min}} \geq -.45$

2. Maximum pressure recovery after the minimum pressure point is $C_{p_{max}} - C_{p_{min}} \leq 1.0.$

Item 1 restricts the maximum velocity, which occurs near the maximum diameter for streamlined bodies at zero incidence, to values less than $u_e/U_\infty = 1.2$. Item 2 restricts the amount of deceleration occurring downstream of the minimum pressure (maximum velocity) point. These constraints are not "hard" in that they represent reasonable values but may rightfully be questioned since they are engineering approximations to the separation constraint boundary.

Excepting the Reynolds number, all of the constraints mentioned above are of the inequality type since they represent limiting situations or boundaries. The general conceptual form of these inequalities can be written as

$$g(a_1, a_2, \ldots, a_N) \leq 0 \qquad (3.11)$$

although the explicit expression does not always exist, e.g., non-separating constraint boundary. The requirements for non-negative body dimensions are constant linear constraints, while the noninflected forebody and nonseparating flow constraints are nonlinear. Thus the drag minimization proble... involves linear and nonlinear inequality constraints; at least one constraint possesses no explicit form as given by equation (3.11).

The convexity of the constraint boundaries must be considered. Regions with convex boundaries, e.g., interior of a circle, normally present no additional difficulties to a search strategy. However, regions with nonconvex boundaries, e.g., interior of a cardioid, may cause a search strategy to "hang up" on such a boundary far from the true feasible optimum. It will be shown by graphical means in Chapter 4 that nonconvex boundaries do exist for at least one of the two classes of bodies considered in the present study.

The feasible optimum may lie on the interior or on the boundaries of a constrained parameter space. Optimization methods which converge quickly on the interior due to approximate quadratic convergence may not be able to exploit this property if the optimum lies on constraint boundaries (constrained optimum). One reason is that the performance function may retain dominating first-order properties at the boundaries so that second-order (quadratic) characteristics remain insignificant. By contrast, a performance function with an interior optimum will have a neighborhood about the optimum in which the first-order character-istics, i.e., the gradient or first partial derivatives, tend to zero so that second-order properties, i.e., second partial derivatives, tend to dominate. Since it is not known at the outset that the optimal solution lies on or off constraint boundaries, it is appropriate to consider alternate methods which work well in one situation or the other if not both.

Reference Reynolds Number — An Equality Constraint. In previous discussions the reference Reynolds number has been defined as

$R_V = V^{\frac{1}{3}} U_\infty/\nu$, where V is the vehicle volume so that $V^{\frac{1}{3}}$ is a reference length, U_∞ is the constant vehicle speed, and ν is the fluid kinematic viscosity. No consideration is given to ν since it is regarded as a fixed constant here. A fixed Reynolds number R_V implies a fixed vehicle volume V since U_∞ is already specified. Thus R_V is equivalent to an equality constraint requiring the body profile Y(X) to enclose a specified volume V. However, since the fluid dynamics depends on the shape Y(X) and Reynolds number R_V, and not separately the volume V, i.e., the size of the body, and velocity U_∞ one may simply scale the shape to automatically maintain the proper volume. In fact, both V and U_∞ may be scaled so long as the proper R_V is preserved. Thus, because of the nature of the fluid dynamics, it is possible to exclude consideration of the volume equality constraint from the optimization strategy itself.

As mentioned in Chapter 1, it may be desirable to specify equality constraints on quantities other than volume. For example, the constant frontal-area problem, e.g., torpedo design, may be more conveniently based on a constant maximum diameter Reynolds number. If there are neutral buoyancy requirements for the torpedo problem, then a volume equality constraint is still present and must be dealt with by suitable means, not necessarily within the search strategy itself.

Depending on the application there may be other constraints to be considered. For example, submarines must occasionally negotiate channels dredged to a certain depth; hence, the submarine hull design is subject to a maximum diameter constraint. Another example is the design of the "lower unit" of an outboard motor. The lower unit is the faired transmission housing to which the propeller is attached and by which the propeller is powered. The design of the lower unit is subject to the constraint of the space requirements of the transmission. The optimization method should be able to cope with these kinds of constraints, assuming, of course, that the constraints do not prohibit the existence of a feasible solution.

To summarize the ideas of the preceding paragraphs, the optimization method used for the drag minimization problem must be capable of

dealing with a nonlinear performance function without the use of gradients. The method must cope with nonlinear inequality constraints which may be nonconvex and which exist in implicit or explicit form. Furthermore, it is appropriate to consider alternate methods which are well suited to the optimum-on-boundary or optimum-on-interior situations.

3.4 Selected Search Strategies

For the nongradient, constrained, nonlinear drag minimization problem there are two possible approaches using direct (nongradient) search methods. One approach is to use a method which operates in a nonlinear inequality constraint environment. The second approach is to replace all inequality constraints with a suitably constructed penalty function so that an unconstrained search method may be used. In either case there are methods which are regarded as more efficient than others, but the generalization is not always valid since the performance of a search method is problem dependent. It is not unusual to modify the search method so as to make it more efficient for a particular problem. Some "tailoring" has been necessary in the present study; details are given below.

For the drag minimization problem it was decided at the outset to select one promising method and to proceed with the hydrodynamic design problem. Modifications in the method would be made if they were necessary to obtain optimal solutions. No comprehensive experimentation with various modifications or different methods would be done due to the costly nature of the performance function evaluation (40 seconds on the CDC 6500). Later in the study, however, it was decided to try one additional method.

Of the many search strategies in the literature for nongradient, nonlinear parametric problems, there are two which have been developed to operate in an environment of general nonlinear inequality constraints of the form given by equation (3.11). The earlier method is due to Rosenbrock (1960) [21]; the newer method is due to Box (1965) [22] with suggested modifications by Guin (1968) [23]. In this study a slight

modification of the Box-Guin "Complex Method" has been used extensively. The method is described in a later section.

The various nongradient search strategies in the literature for unconstrained problems far outnumber those developed for the constrained variety. Examples of these methods include an early approach due to Hooke and Jeeves (1961) [24], a method with approximate quadratic convergence due to Powell (1964) [25], a directed-hypercone random search algorithm due to Wozny and Heydt (1970) [26], and a recent modification of the Nelder-Mead procedure due to Masters and Drucker (1971) [27]. A crit' eview including Powell's method has been reported by Fletcher (1965) [28]. When using unconstrained search strategies with constrained problems, one common practice is to replace the inequality constraints by a penalty function (pp. 477 - 482 of [20]). Of the many available unconstrained direct search methods, Powell's method, because of its approximate quadratic convergence, is used in the present study in conjunction with a simple but general penalty function. The details are left to a later section.

<u>Modified Complex Method.</u> A detailed word flow chart of the modified Complex Method, as used in the present study, is given in Appendix C. The Guin modifications, which include strategies for coping with nonconvex boundaries and for generating alternate search directions when the primary direction fails, have been included in this method. A modification in the starting procedure is also included.

Shown in Figure 17 is a slightly simplified version of the method; specifically, the strategy for nonconvex boundaries is omitted since its use has never been required during drag minimization runs. The basic input data are the nu: ~r of independent parameters N, the number of vertices K in the complex figure (usually K = 2N), convergence tolerances ϵ_2 and ϵ_3 (usually $\epsilon_2 = \epsilon_3 = .01$), and the fixed Reynolds number. For the initial complex generation, constant lower and upper boundaries, a_{L_i} and a_{U_i}, i = 1, ..., N, respectively, are also input. No initial guess is needed.

The vertices $\underline{a}_j$, j = 1, ..., K, for the initial complex figure are randomly generated within the constant rectangular boundaries defined

Input. N, K, c_1, c_3
a_{L_i}, a_{U_i}, $i = 1, \ldots, N$

Start → Set $j = 1$

Randomly Generate Vertex $\underline{a}_j$ in N-Space
Bounded by a_{L_i} and a_{U_i}, $i = 1, \ldots, N$

Is $\underline{a}_j$ Feasible? — No

Yes

Evaluate Performance Function PF_j

$j = j + 1$

$j > K$ — No

Yes
(End of Initial Complex Generation)

① → Reject Worst Vertex

② (Rejected Vertex is $\underline{a}_r$)

Compute Centroid $\underline{cgr}$ of Remaining Vertices

Generate Trial Vertex $\underline{a}_t$ by Reflection through $\underline{cgr}$

Is $\underline{a}_t$ Feasible? — No → Move $\underline{a}_t$ Halfway Toward $\underline{cgr}$

Yes

Move $\underline{a}_t$ Halfway Toward $\underline{cgr}$

Evaluate PF_t for $\underline{a}_t$

Is $\underline{a}_t$ within c_1-Neighborhood of $\underline{cgr}$? — No

Is PF_t Better Than 2nd Worst PF Value? — No

Yes

Replace $\underline{a}_r$ by $\underline{a}_t$

Yes

Try New Search Direction. Reject Next Worst Vertex and Retain Previously Rejected Vertex

Check Stopping Condition. Are Five Best PF Values within c_3 Neighborhood of Best PF Value? — No → go to ①

go to ②

Yes

Problem Is Solved. Optimum Is Best Vertex

Stop

Figure 17. Flow Chart for Modified Complex Method.

by a_{L_i}, a_{U_i}, $i = 1, \ldots, N$. Each parameter a_i is uniformly distributed over its interval $a_{U_i} - a_{L_i}$, so that each vertex $\underline{a}_j$ is uniformly distributed over the enclosed rectangular N-dimensional volume. The random vertex $\underline{a}_j$ is checked for feasibility; a nonfeasible vertex is simply thrown out and randomly regenerated. Whenever a random vertex is found to be feasible, its performance function PF_j is evaluated. The process continues until a complete complex is formed.

The original starting procedure used by Box [22] requires an initial feasible vertex. Each succeeding vertex is randomly generated as outlined in the above paragraph, but a nonfeasible vertex is moved halfway toward the centroid of the partially completed complex figure. The presence of the initial feasible vertex insures that the random vertex will always become feasible by this process. This procedure is r t adequate for feasible regions which are highly nonrectangular, which is the situation in the present study. Although each parameter may be allowed large variations, the actual feasible volume is a small fraction of the N-space rectangular volume bounded by $\underline{a}_U$ and $\underline{a}_L$. This effect is more prc 'ounced for large N. The effect of the nonrectangularity of the feasible region is to cause each random vertex to be moved half the distance to the centroid many times. The result is that the entire initial complex tends to be clustered in a relatively small neighborhood about the initial feasible vertex. Since the initial complex is not well distributed over the feasible space, there is no global information about the performance function surface. Hence, the chances of converging to the global feasible optimum are reduced. Furthermore, the small scale of the initial complex implies small steps and slow progress until the complex has a chance to expand. But the most detrimental effect is that the close proximity of all the vertices in the initial complex greatly increases the chances of premature convergence by the stopping criterion used with this method. The modified starting procedure removes these problems. The well-distributed initial complex makes large global moves at first and has a better chance of finding the global feasible optimum, although it does not always do so, as results in Chapter 5 demonstrate.

Continuing with Figure 17, once the initial complex is formed, the procedure is to reject the worst vertex, i.e., the vertex associated with the highest drag coefficient. A trial vertex is generated by reflection through the centroid of the nonrejected vertices an amount α times the distance from the rejected vertex to the centroid. The empirical expansion factor α is 1.3 throughout this study, as recommended by Box [22]. If the trial vertex is not feasible, it is repeatedly moved halfway toward the centroid until it becomes feasible. Nonconvexities may cause problems here since the centroid of the feasible vertices may not lie in a feasible region. Repeatedly moving a nonfeasible vertex halfway toward a nonfeasible centroid may prove futile. Guin suggests at this point that the entire complex be thrown out; details are in Appendix C.

Once a feasible trial vertex is found, its performance function PF, i.e., drag coefficient, is computed and compared with the second worst PF value of the complex. The second worst value is used rather than the worst to avoid the situation in which the trial PF is between the worst and second worst values, in which case the newly found vertex is immediately rejected at the start of the next cycle. This implies that the direction of the next cycle will be toward the point from which the present cycle started. This situation is expected when the complex is straddling a local optimum, but otherwise wasted moves result. If the trial PF is better than the second worst PF value, the trial vertex replaces the worst vertex; otherwise, the trial vertex is moved halfway toward the centroid and the new PF is checked. This retraction toward the centroid continues until the PF value is acceptable or until the trial vertex enters a relative ε_2-neighborhood of the centroid. If the latter occurs, a new search direction is tried by rejecting the next worst vertex and retaining that previously rejected.

The process of direction change continues until an acceptable vertex (feasible, PF better than second worst value) is found. In all cases, the worst vertex is replaced by the newly found vertex. The stopping condition is checked and if it is not satisfied the procedure begins again at entry point 1 in Figure 17. A premature abort occurs when a new acceptable vertex cannot be found. In such cases, it is

assumed that an optimum has been found even though the stopping condition is not satisfied. As with all search strategies, the modified Complex Method converges to a local optimum; hence, it may be necessary to solve the problem several times using different randomly generated initial complex figures in order to establish that a feasible global optimum has indeed been found.

Several features of the modified Complex Method make it especially suited to the drag minimization problem. The primary feature is that the method can cope with rather general inequality constraints which are explicit or implicit in the parameters. The method only requires a "yes" or "no" to the feasibility question; it does not matter which constraints are violated or how much. Thus it is a simple matter to cope with the separation constraint directly. The complex figure's ability to "roll" along boundaries helps to prevent premature convergence on a boundary. Since the method uses global features of the function surface, it is not sensitive to local irregularities which might confuse local gradient methods. The logical strategy is straightforward and easy to implement on the digital computer. The method as presented here is self-starting; if the optimum is known to lie in a certain region, that information can be exploited at the outset by adjusting the constant boundaries a_{L_i} and a_{U_i}, $i = 1, \ldots, N$. No parameter scaling is required since the movements of the complex are automatically scaled to the range $a_{U_i} - a_{L_i}$, $i = 1, \ldots, N$.

There are several deficiencies in the method described here. The stopping condition, while precisely defined, has proved economically costly to satisfy. That is, many PF evaluations are required to establish that the present best vertex is a local optimum. In fact, for the drag minimization problem, the stopping condition has never been satisfied. Rather, the search is aborted after a large number, e.g., 3N to 4N, of PF evaluations do not improve the best PF value. The best vertex is assumed to be a reasonable approximation to the local optimum. A second deficiency is the method's inability to handle equality constraints; these must be handled by means outside the search strategy itself.

A third deficiency, related to the stopping condition, is that the method lacks quadratic convergence near local optima. This is important if the local optimum is interior, not on a boundary. One of the two classes of bodies considered in this study appears to have interior optima (changing with Reynolds number R_v), so that some consideration has been given to this weakness of the Complex Method. It appears appropriate to exploit a quadratically convergent method for constrained problems which have interior optima; for this reason Powell's Method of Conjugate Directions [25], which is approximately quadratically convergent, has been used.

Powell's Method of Conjugate Directions.

A detailed word flow chart of Powell's Method, as used in the present study, is given in Appendix D. Powell's Method generates search directions but leaves the actual minimization along the line of search to an external method. A parabolic interpolation scheme is used for the linear minimization in the present study; details are given in Appendix D.

Shown in Figure 18 is the essential structure of Powell's Method of Conjugate Directions as used in this study. The basic input data are the number of independent parameters N; an initial feasible guess vector $\underline{a}_o$, i.e., $\underline{a}_o = (a_{o_1}, a_{o_2}, \ldots, a_{o_N})$; the lower and upper scaling vectors $\underline{a}_L$ and $\underline{a}_U$, respectively, used to scale the search space; a set of linearly independent search directions $\underline{\xi}_1, \underline{\xi}_2, \ldots, \underline{\xi}_N$; an initial step size STEP for the linear search routine and a convergence tolerance ε_3. Normally the initial set of search directions is the set of unit vectors parallel to the parameter axes. The scaled parameters vary nominally between zero and one.

To start the procedure the initial guess is scaled to $\underline{X}_o$, where $\underline{X}_o = (X_{o_1}, X_{o_2}, \ldots, X_{o_N})$, using the relationship $X_{o_i} = (a_{o_i} - a_{L_i})/(a_{U_i} - a_{L_i})$. The corresponding performance function value PF_o is evaluated. One cycle consists of a linear search along each of the N direction vectors $\underline{\xi}_1, \underline{\xi}_2, \ldots, \underline{\xi}_N$. The minimum point of one search is the base point for the next, so that $\underline{X}_N$ is the best point of the entire cycle. Also, Δ_m is the magnitude of the maximum change in performance

Input. N, ε_n, a_L, a_U, $(c_1, c_2, \ldots, c_K)$, STEP, c_i

Start → **Initialization.**
Scale initial guess $x_i = (a_{i} - a_L)/(a_U - a_L)$
Evaluate PF_o.

Start Search Cycle
$\Delta_m = 0$, $i_m = 1$, $j = 1$

From Base Point x_{j-1} Perform Linear Search in Direction ξ_j. Obtain Minimum x_j with Performance Function Value PF_j.

$|PF_j - PF_{j-1}| > \Delta_m$ — Yes → $\Delta_m = |PF_j - PF_{j-1}|$, $i_m = j$

No

$j = j + 1$

$j \leq N$ — Yes

No

$x_{best} = x_N$
$PF_{best} = PF_N$

$u = x_N - x_o$
$y_t = x_N + u$
$PF_t = PF(y_t)$

$PF_t \geq PF_o$ — Yes

No

$(PF_o - 2PF_N + PF_t)(PF_o - PF_N - \Delta_m)$
$\geq \frac{1}{2} \Delta_m (PF_o - PF_t)$ — Yes

No

New Direction u is to be Inserted into Direction Matrix. Remove Direction ξ_{i_m}.
for $i = 1, \ldots, i_m - 1$ $\xi_i = \xi_i$
for $i = i_m - 1, \ldots, N - 1$ $\xi_i = \xi_{i+1}$
for $i = N$ $\xi_N = u/|u|$

From Point x_N Perform Linear Search in New Direction ξ_N. Obtain Minimum Point x_{best} with PF_{best}.
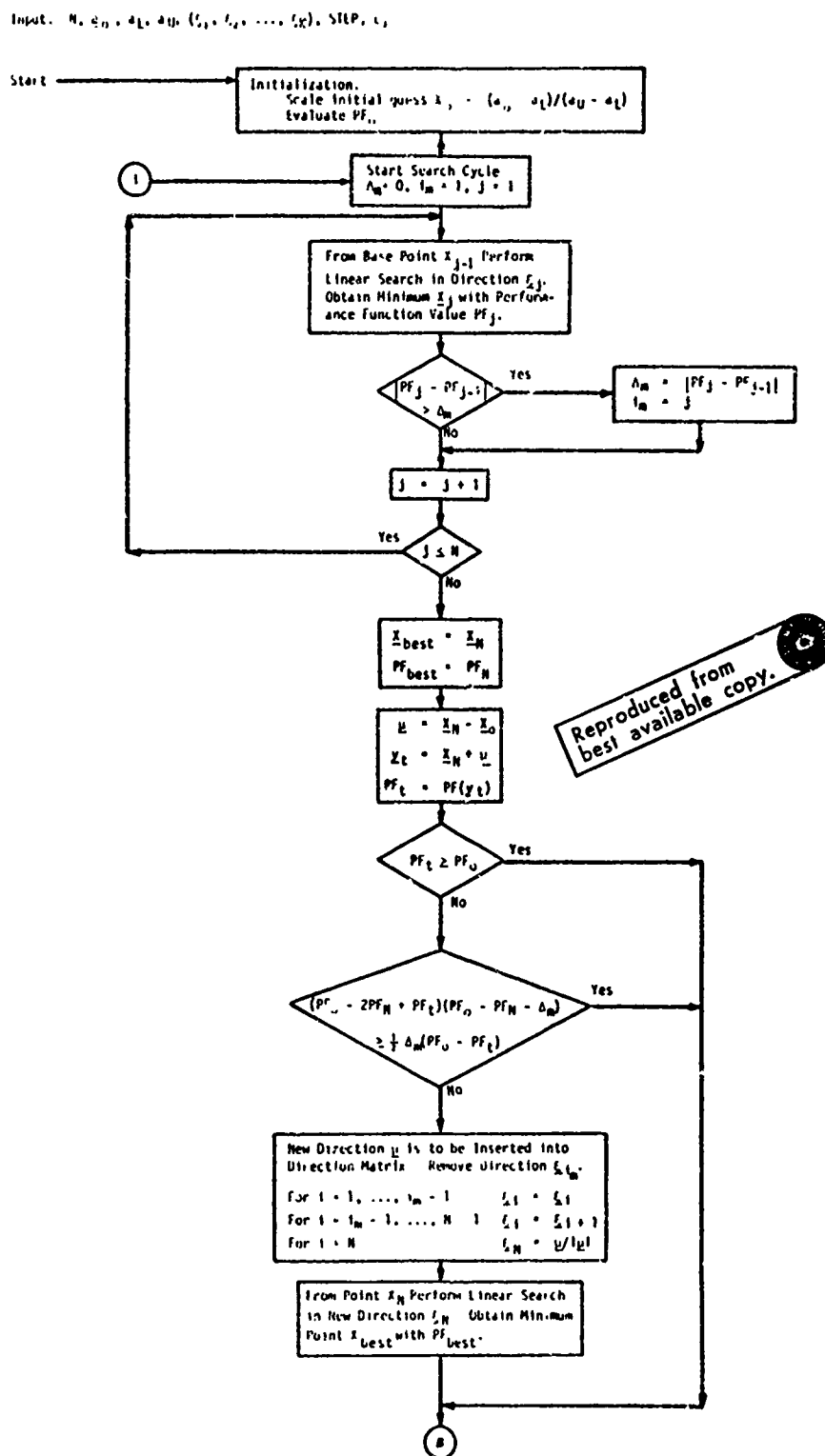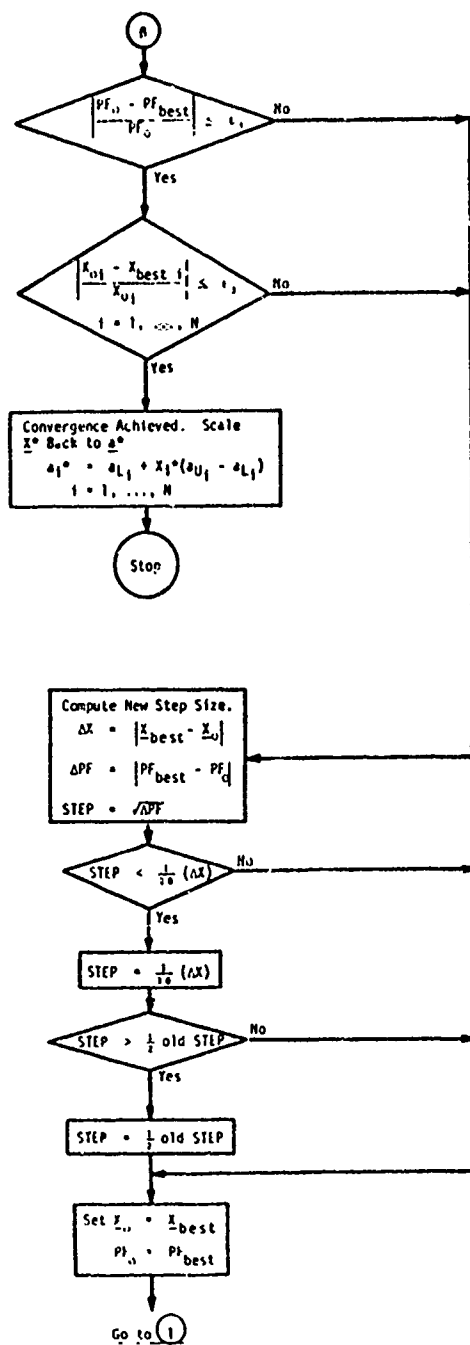
Figure 18. Flow Chart for Powell's Method.

Figure 18. cont.

function to occur in any one linear search. The corresponding direction vector of maximum change is $\underline{\xi}_{im}$.

The next phase of the method is to generate the new direction vector $\underline{\mu} = \underline{X}_N - \underline{X}_o$, and to compute the trial point $\underline{y}_t = \underline{X}_N + \underline{\mu}$ with its performance function PF_t. Two inequality checks determine whether the new direction is promising or not. If the new direction is promising, an additional linear search along it is made; the $\underline{\xi}_{im}$ direction vector is thrown out and the new direction vector $\underline{\mu}/|\underline{\mu}|$ is inserted into the last position of the set of search directions. Powell has proved for quadratic surfaces that this procedure guarantees that the new set of directions will be at least as efficient as the previous set.

After deciding to keep or reject the new direction, a convergence check is performed. The check involves the original base point $\underline{X}_o$ and the best point of the cycle. If convergence is not achieved, a new step size STEP is computed. The new STEP magnitude must lie between certain reasonable limits; it can never be larger than $\frac{1}{2}$ (old STEP). The latter limit is introduced to forc the search to become more local with each succeeding cycle; it is a modification of Powell's original procedure. The minimization continues cycle by cycle until the convergence criteria are satisfied.

Since Powell's method cannot cope with constraint boundaries, they must be replaced with a suitably constructed penalty function. The effect of the penalty function must be to keep the search in the feasible region. For the drag minimization a penalty function with the following properties is desirable:

1. The penalty function must deal with general explicit or implicit inequality constraints in a manner similar to the Complex Method.

2. Since a constraint violation may render the drag model totally invalid, the penalty function must generate an apparent performance function value without employing the drag model itself. In other words, in nonfeasible regions the response surface may not even exist.

3. The penalty function should not distort the response
   surface on the feasible region.

Item 1 implies that constraint violaticns are to be indicated with a
simple "yes" or "no" as is done in the Complex Method, rather than indi-
cating which constraints are violated and by how much. Item 2 is a real
necessity since some constraint violations, e.g., non-negative body
dimensions, yield a physically meaningless body shape. Furthermore,
avoiding a drag computation saves computer time   Item 3 implies that
the penalty function has no influence on the feasible region so that the
performance function is the actual drag value there. For the drag mini-
mization a performance function PF which includes a simple penalty
function satisfying all three items above is defined as

$$
PF = \begin{cases} C_D & \text{, no constraints violated} \\[2em] C_{D_{NKV}} + c_1 \left| C_{D_{NKV}} \right| & \text{, constraints violated} \end{cases} \tag{3.12}
$$

where $C_{D_{NKV}}$ is the nearest known value of C_D on the feasible region and
c_1 is a small positive constant approximately equal to the search conver-
gence tolerance. Equation (3.12) may be generalized to

$$
PF = \begin{cases} PF_{\text{actual value}} & \text{, no constraints violated} \\[1.5em] PF_{NKV} + c_1 \left| PF_{NKV} \right| & \text{, constraints violated and} \\ & \quad PF_{NKV} \neq 0 \\[1em] \text{small positive number,} & \text{constraints violated and} \\ & \quad PF_{NKV} = 0 \end{cases} \tag{3.13}
$$

where PF_{NKV} is the nearest known value of PF on the feasible region.

The constant $c_1 > 0$ is arbitrary but is selected so as to make the ficticious PF surface appear reasonably well behaved.

The Powell Method used in conjunction with the penalty function implied in equation (3.13) has several features useful in the drag minimization problem. It can handle the general inequality constraints in the same manner as the Complex Method. It possesses approximate quadratic convergence which may be beneficial for finding interior optima.

There are potential deficiencies in the method. An initial feasible guess is required so the method is not self-starting; for some problems locating a feasible initial guess is not trivial. The parameter space should be scaled so that each parameter has an "equal interest" in the performance function. The method uses local information in its moves so that local irregularities may confuse the search strategy. However, one motivation for using a "local" method in the drag minimization is to study the migration of local minima with Reynolds number. The stopping condition as indicated in Figure 18 is as costly to satisfy as that for the Complex Method. From a practical point of view it may be adequate to test for performance function convergence but not parameter convergence.

3.5 Properties of the Optimal Solution

After obtaining an optimal solution, four properties of that solution must be considered. These include uniqueness, a global versus nonglobal solution, and the sensitivity of the optimum to off-design conditions. The fourth property emerges when the optimal solution is obtained using a finite search and a finite stopping condition; it is the proximity of the reported solution to the true local minimum. These properties are of concern in all optimization problems, but they will be commented on below in terms of a numerical "black-box" performance function to which a finite search has been applied. This is, of course, the situation for the drag minimization problem.

The te... ...que" is being used in an engineering sense. Optimal solutions w. ... are spatially far apart in an N-parameter space but wnich are close in their performance function values, say to within the convergence tolerance, are regarded as nonunique solutions. The term "global" refers to the best of all the feasible local optima, but it has meaning only after uniqueness is established. For "black-box" models there are no rigorous procedures for establishing whether an optimal solution is either unique or global. This is true for optima on the interior or on a boundary. At best these properties can only be indicated by solving the same optimization problem several times using different starting conditions. This procedure has been used in the present study.

The question of sensitivity has real practical importance. Essentially, it is desirable to know how quickly the optimal solution degrades in performance at off-design conditions. Such conditions occur due to variations in the parameters, variations in assumed fixed conditions, e.g., Reynolds number, and variations in the model, e.g., transition prediction. These off-design conditions are examined in this study, although not uniformly for every optimum body design.

The proximity of the reported solution to the true local optimum can be interpreted in two ways. From the design point of view proximity of performance is emphasized; from the optimization point of view spatial proximity as well as performance proximity are important. The latter statement is true because it is of interest to know how efficient a search strategy is in seeking out local minima. When using finite search strategies with "black-box" models, the local optimum is usually never known exactly. One procedure is to fit an analytic quadratic surface locally in the neighborhood of the best solution [20]. The minimi of this analytic surface is found accurately; the true minimum is known to within a finte but smaller tolerance. A side benefit of the quadratic surface fit is the immediate approximate information of local curvature behavior useful in sensitivity studies.

To work reliably the above procedure requires a reasonable distribution of experiments (points) in a neighborhood about the suspected local optimum. In an N-parameter space at least $N + N(N + 1)/2$

experiments are required. Usually the requirement of a "reasonable
distribution" forces the generation of some additional points not ob-
tained during the actual optimization run so that an extra cost is
incurred using this procedure.

A less thorough and less costly approach for determining the
proximity of the best point to the true local optimum is to examine
several points randomly distributed on the surface of an N-hypersphere
whose center is the reported best point. The radius of the normalized
hypersphere may be the normalized convergence tolerance for example.
The procedure is to randomly generate a direction, orthogonal to any
previous directions, and to test the performance function value at
both ends of the hyperspherical diameter parallel to the generated
direction. The random direction is rejected and regenerated if both
ends are in nonfeasible regions. If no better point is found after
two or three random directions have been checked, then the confidence
in the assumption that the reported optimum is near the true local
optimum has increased. However, if a better point is found, then the
radius is immediately increased and the procedure is repeated. An
alternate procedure is to re-center the same hypersphere on the new
best point and to repeat the procedure. If a better point is found
on the second hypersphere, then it is assumed that the reported optimal
solution is not a particularly good approximation to the true local
optimum. But the point may still be acceptable if the performance
function value differences are small. In the present study proximity
checks are made using this procedure rather than the quadratic surface
fit.

3.6 Comment on Optimization Philosophy

The optimization philosophy emerging in this chapter is summarized
in this section. Essentially the drag minimization is to be solved
through the interactions of two digital computer programs, each a
"black-box" to the other. The drag model and search strategies are
independent of each other; hence, independent improvements can be made

in one without affecting the other. This idea has been established
from the outset so that as better drag models or search strategies
become available, they may be incorporated into the drag minimization
package with only minor programming changes. So as to not overempha-
size the "black-box" relationship, experience has shown that it is
usually beneficial to tailor the search strategy somewhat to the partic-
ular problem in order to make the complete package more efficient.

The Complex Method and Powell's Method with the penalty function
given by equation (3.13) represent diverse search strategies. The
diversity should lend a degree of confidence to the determination of
uniqueness and global optimality. The Complex Method, with its ran-
domly and globally distributed initial complex figure, has some chance
of finding the global optimum, if there is only one. Powell's Method,
with its local movements, should be able to "track" a local minimum
drag shape with changing Reynolds number. Two other benefits of
Powell's Method for interior optima include efficient convergence and
the approximate knowledge of the local curvature at the optimum point.

There are two points of view regarding the results of the drag
minimization studies. One is the design point of view in which the
emphasis is on the performance of the design and its sensitivity to
off-design conditions. The other is the optimization point of view
which includes consideration of the above and also uniqueness, globality,
proximity to the true optimum, and search efficiency. Both points of
view are retained in the results to follow but not uniformly with every
minimum drag shape.

CHAPTER 4

PARAMETRIC BODY PROFILES

This chapter defines the two classes of bodies used in the present study. Certain inequality constraint expressions are also presentcJ. A parametric definition of body shapes more general than that given by equation (3.10) may be expressed as

$$Y(X) = Y\left[\sum_{i=1}^{N} a_i F_i(X), G(X) \right] \tag{4.1}$$

where N is the number of independent parameters a_i associated with the known functior. $F_i(X)$. The known function $G(X)$ is present to satisfy certain boundary conditions built into $Y(X)$. Equation (4.1) implies that $Y(X)$ may not be a simple linear combination of known functions.

The procedures used to derive the expressions for $Y(X)$, i.e., equation (4.1), are essentially those reported by Granville (1969) [29]. The idea is to divide the body into sections each of which is described by a low degree polynomial. From hydrodynamic ، nsideratio s the complete body is to be continuous through second derivatives; for example, a discontinuity in curvature can cause a "pressure spike" (local region of highly accelerated flow) to occur. The low degree polynomial of each section is completely specified in terms of its boundary conditions, some of which are fixed and some of which are free to be manipulated. Those which may be manipulated are the parameters to be varied during an optimization run. Furthermore, for each body section only two boundary conditions are free so that two-dimensional constraint boundaries can be plotted. The complete derivations are left to Appendix E; th results are reported here.

4.1 Five-Parameter Rounded-Nose, Pointed-Tail Body [29]

An example of this body is shown in Figure19. The forebody $(0 \leq X \leq X_m)$ is described by a fourth-degree polynomial, the aftbody $(X_m \leq X \leq L)$ by a fifth-degree polynomial.
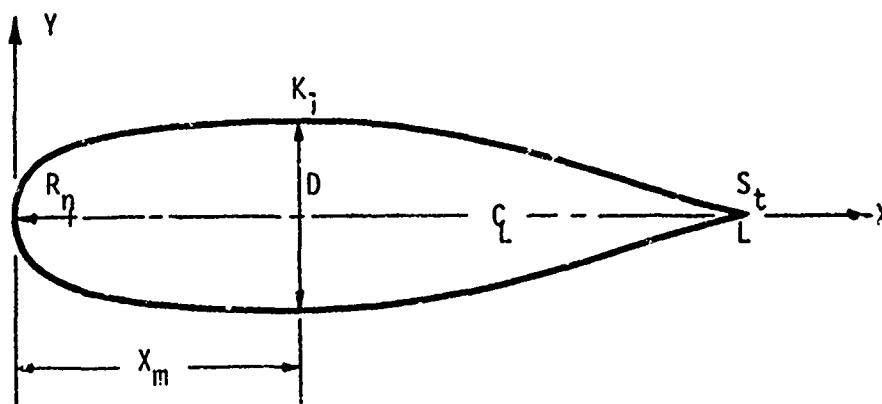

Figure 19. Rounded-Nose Pointed Tail Body.

The six dimensional parameters shown in the figure are listed below:

1. R_n = Radius of curvature at nose

    = $1/(d^2X/dY^2)$ at X = 0

2. D = Maximum diameter

    = $Y(X_m)$

3. X_m = Axial location of maximum diameter D

4. K_1 = Curvature at X_m

   = $d^2Y(X_m)/dX^2$

5. S_t = Profile slope at tail

   = $dY(L)/dX$

6. L = Overall body length

The rounded-nose, i.e., infinite slope, is a built-in boundary condition, although a zero radius of curvature, $R_n = 0$, is allowed. The pointed-tail, i.e., finite slope, is also a built-in boundary condition.

The six parameters listed above can be reduced to five which are nondimensional, hence the "five-parameter" designation. These are listed below.

1. r_n = Nondimensional radius of curvature at nose

   = $[4X_m/D^2]\ R_n = [4x_m f_r^2]\ R_n/L$ (4.2a)

2. f_r = Fineness ratio

   = L/D (4.2b)

3. x_m = Nondimensional axial location of maximum diameter D

   = X_m/L (4.2c)

4. k_1 = Nondimensional curvature at X_m

   = $[-2X_m^2/D]\ K_1 = [-2x_m^2 f_r]\ K_1\ L$ (4.2d)

5. s_t = Nondimensional slope at tail

   = $[-2(L-X_m)/D]\ S_t = [-2(1-x_m)f_r]\ S_t$ (4.2e)

All nondimensional parameters are defined so that they are normally non-negative. The particular nondimensionalizing expressions emerge

during the derivations given in Appendix E. The length L is not a free parameter to be manipulated since it must be scaled to satisfy the fixed Reynolds number.

The analytical expressions for this five-parameter body are given below:

1. For $0 \leq X \leq X_m$ (forebody):

$$\frac{Y(X)}{L} = \frac{1}{2f_r} [r_n F_1(x) + k_1 F_2(x) + G(x)]^{\frac{1}{2}} \qquad (4.3)$$

where

$$x = X/X_m \qquad (4.4a)$$

$$F_1(x) = -2x(x - 1)^3 \qquad (4.4b)$$

$$F_2(x) = -x^2(x - 1)^2 \qquad (4.4c)$$

$$G(x) = x^2(3x^2 - 8x + 6) \qquad (4.4d)$$

2. For $X_m \leq X \leq L$ (pointed aftbody):

$$\frac{Y(X)}{L} = \frac{1}{2f_r} [s_t^2 F_1(x) + (\frac{1-X_m}{X_m})^2 k_1 F_2(x) + G(x)]^{\frac{1}{2}} \qquad (4.5)$$

where

$$x = (L-X)/(L-X_m) \qquad (4.6a)$$

$$F_1(x) = -x^2(x - 1)^3 \qquad (4.6b)$$

$$F_2(x) = -x^3(x - 1)^2 \qquad (4.6c)$$

$$G(x) = x^3(6x^2 - 15x + 10) \qquad (4.6d)$$

The constraint boundaries imposed on the five nondimensional parameters are listed below. Some are obviously "pre-judgments" influenced by previous hydrodynamic experience.

The complicated constraints are listed last and are considered in detail.

1. Non-negative radius of curvature R_n at nose, or

$$r_n \geq 0 \qquad (4.7a)$$

2. Nonpositive curvature K_1 at maximum diameter, or

$$k_1 \geq 0 \qquad (4.7b)$$

3. Real location for maximum diameter so that

$$0 < x_m < 1 \qquad (4.7c)$$

4. Reasonable fineness ratios, i.e., not conducive to separation, so that

$$f_r \geq \text{ some positive constant, say } 2.5 \qquad (4.7d)$$

5. Nonpositive slope S_t at tail, or

$$s_t \geq 0 \qquad (4.7e)$$

6. No inflection points on forebody

7. No or only one inflection point on aftbody

The low degree polynomials for the two body sections together with constraints 1 through 7 above imply that the body profile is always non-negative.

Noninflected Forebody. The forebody, which is described by a fourth-degree polynomial, may have zero, one, or two inflection points. The analysis [29] given in Appendix E leads to a set of two simultaneous nonlinear algebraic equations which must be solved by numerical iteration. The solution gives the r_n versus k_1 curve along which one limiting inflection occurs on the forebody in that the second derivative touches

zero but does not change sign. The convex r_n versus k_1 boundary is shown in Figure 20; the non-negative boundaries are due to equations (4.7a) and (4.7b) above. The existence of two inflections in the labelled region is demonstrated graphically [29].
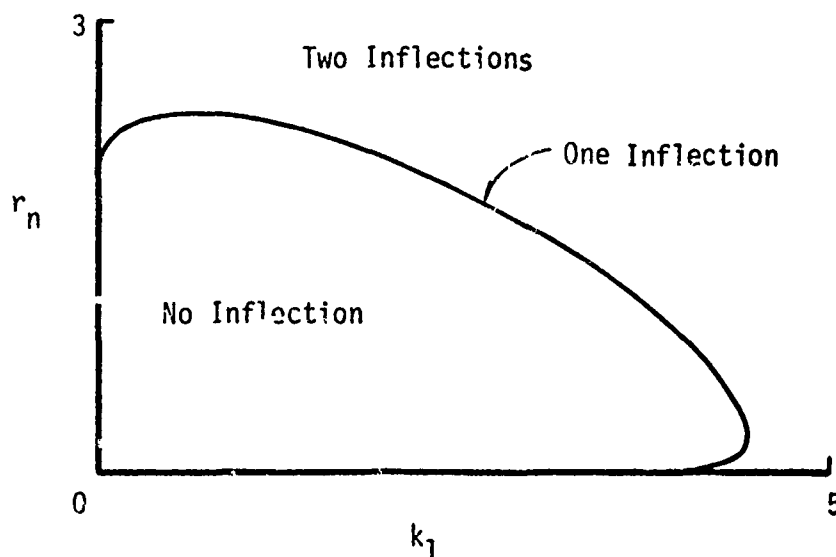
Figure 20. Feasible Region for Noninflected
Rounded-Nose Forebody Section.

Noninflected or Inflected Pointed Aftbody. The aftbody, which is described by a fifth-degree polynomial, may have zero, one, two, or three inflection points. The analysis [29] given in Appendix E leads to a set of two simultaneous nonlinear algebraic equations which must be solved by numerical iteration. A singularity leads to another set of equations which can be solved directly. The resulting s_t^2 versus $[(1 - x_m)/x_m]^2 k_1$ curves are shown in Figure 21. A nonconvexity arises when both noninflected and singly inflected aftbodies are allowed. The curved boundary represents the limiting inflection in that the second

derivative touches zero but does not change sign. The number of inflec-
tions in each region has been established by Granville [29].
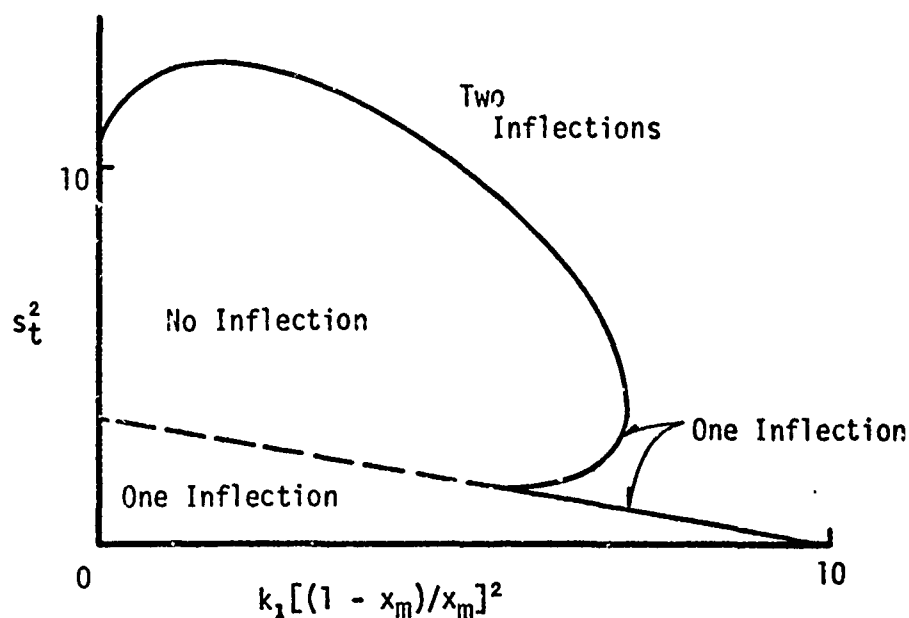
Figure 21. Feasible Region for Noninflected or Singly
Inflected Pointed Aftbody Section.

4.2 Eight-Parameter Rounded-Nose, Tailboom Body

An example of this body is shown in Figure 22. The forebody ($0 \leq X \leq X_m$) is described by a fourth-degree polynomial as in Section 4.1 above, the midbody ($X_m \leq X \leq X_i$) by a fifth-degree polynomial, and the tailboom aftbody ($X_i \leq X \leq L$) by a fifth-degree polynomial.
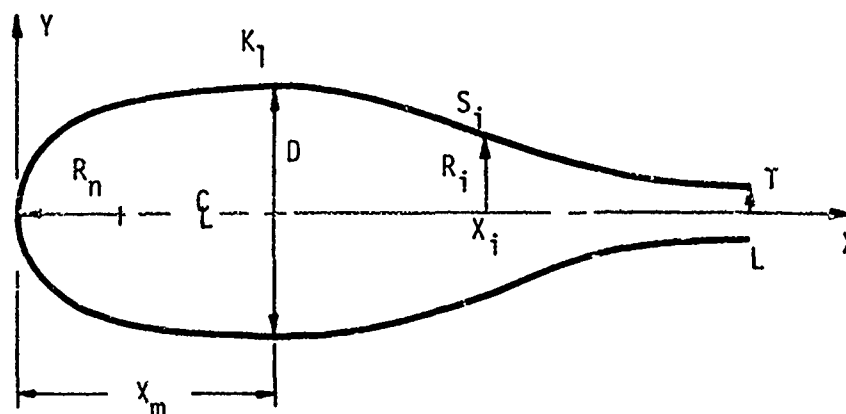
Figure 22. Rounded-Nose Tailboom Body.

The nine dimensional parameters shown in the figure are listed below:

1. R_n = Radius of curvature at nose

   = $1/[d^2X/dY^2]$ at $X = 0$

2. D = Maximum diameter

   = $Y(X_m)$

3. X_m = Axial location of maximum diameter D

4. K_1 = Curvature at X_m

   = $d^2Y(X_m)/dX^2$

5. X_i = Axial location of inflection point

6. R_i = Profile radius at X_i

     = $Y(X_i)$

7. S_i = Profile slope at X_i

     = $dY(X_i)/dX$

8. T = Terminal profile radius

     = $Y(L)$

9. L = Overall body length

The rounded-nose, i.e., infinite slope, is a built-in boundary condition as in Section 4.1 above, and $R_n = 0$ is allowed. The tailboom has built-in boundary conditions of zero slope and curvature, and $T = 0$ is mathematically allowable. The zero slope and curvature at X equal L implies that a cylindrical tailboom extension may be added without loss of profile continuity through the second derivative.

The nine parameters listed above can be reduced to eight which are nondimensional, hence the "eight-parameter" designation. These are listed below:

1. r_n = Nondimensional radius of curvature at nose

     = $(4X_m/D^2) R_n = (4x_m f_r^2) R_n/L$ (4.8a)

2. f_r = Fineness ratio

     = L/D (4.8b)

3. x_m = Nondimensional axial location of maximum diameter D

     = X_m/L (4.8c)

4. k_1 = Nondimensional curvature at X_m

     = $(-2X_m^2/D) K_1 = (-2x_m^2 f_r) K_1 L$ (4.8d)

5. x_i = Nondimensional axial location of inflection point

$$= X_i/L \qquad (4.8e)$$

6. r_i = Nondimensional profile radius at X_i

$$= (2/D)\, R_i = (2f_r)\, R_i/L \qquad (4.8f)$$

7. s_i = Nondimensional profile slope at X_i

$$= [-(X_i - X_m)/(D/2 - R_i)]S_i$$

$$= [-2f_r(x_i - x_m)/(1 - r_i)]S_i \qquad (4.8g)$$

8. t = Nondimensional terminal profile radius

$$= (2/D)\, T = (2f_r)\, T/L \qquad (4.8h)$$

All nondimensional parameters are defined so that they are normally non-negative. The particular nondimensionalizing expressions emerge during the derivations given in Appendix E. The length L is not a free parameter to be manipulated since it must be scaled to satisfy the fixed Reynolds number.

The analytical expressions for this eight-parameter body are given below. The expressions for the forebody $(0 \le X \le X_m)$ are identical to those given by equations (4.3) and (4.4) in Section 4.1 above; they are not repeated here.

1. For $X_m \le X \le X_i$ (midbody):

$$\frac{Y(X)}{L} = \frac{1}{2f_r}\left\{ r_i + (1-r_i)\left[\frac{(x_i/x_m-1)^2}{(1-r_i)}\, k_1\, F_1(x) \right.\right.$$

$$\left.\left. + s_i\, F_2(x) + G(x) \right]\right\} \qquad (4.9)$$

$$\text{where} \quad x = (X_i - X)/(X_i - X_m) \tag{4.10a}$$

$$F_1(x) = -\tfrac{1}{2} x^3(x - 1)^2 \tag{4.10b}$$

$$F_2(x) = x - x^3(3x^2 - 8x + 6) \tag{4.10c}$$

$$G(x) = x^3(6x^2 - 15x + 10) \tag{4.10d}$$

2. For $X_i \le X \le L$ (tailboom aftbody):

$$\frac{Y(X)}{L} = \frac{r_i}{2f_r} \left[1 + (\frac{t}{r_i} - 1) F_1(x) + \frac{(1-r_i)(1-x_i)}{(x_i-x_m)(r_i)} s_i F_2(x) \right]$$

$$\tag{4.11}$$

$$\text{where} \quad x = (L - X)/(L - X_i) \tag{4.12a}$$

$$F_1(x) = 1 - x^3(6x^2 - 15. + 10) \tag{4.12b}$$

$$F_2(x) = -x^3(3x^2 - 7x + 4) \tag{4.12c}$$

The constraint boundaries imposed on the eight ndimensional parameters are listed below. Because the forebody is identical to that for the five-parameter body, some of the constraints listed here are duplicates of those found in Section 4.1.

1. Non-negative radius of curvature R_n at nose, or

$$r_n \ge 0 \tag{4.13a}$$

2. Nonpositive curvature K_1 at maximum diameter, or

$$k_1 \ge 0 \tag{4.13b}$$

3. Compatible locations of maximum diameter and inflection point so that

$$0 \quad x_m < x_i < 1 \tag{4.13c}$$

4. Reasonable fineness ratios, i.e., not conducive to separation, so that

$$f_r \geq \text{some positive constant, say 2.5} \qquad (4.13d)$$

5. Compatible radii at maximum diameter, inflection point, and trailing edge, so that

$$0 \leq t \leq r_i \leq 1 \qquad (4.13e)$$

6. Nonpositive profile slope S_i at inflection point, or

$$s_i \geq 0 \qquad (4.13f)$$

7. No inflection points on body except at X_i and L

The low degree polynomials for the three body sections together with constraints 1 through 7 above imply that the body profile is always non-negative. The inflection point requirement, item 7, implies that all three body sections are noninflected except at X_i and L. The analysis for the noninflected forebody is identical to that for the five-parameter body so that Figure 21 applies.

Noninflected Midbody. The midbody, which is described by a fifth-degree polynomial, may have zero, one, two, or three inflection points, but no more than two on the interval $X_m < X < X_i$ since one is fixed at X equal X_i. The analysis in Appendix E leads to a boundary curve defined by two explicit parametric equations. A singularity leads to an additional equation. The resulting convex s_i versus $[(x_i/x_m - 1)^2/(1 - r_i)]k_1$ curves are shown in Figure 23. The number of inflections in each region is established by a general analytical demonstration.

Noninflected Tailboom Aftbody. The tailboom aftbody, which is described by a fifth-degree polynomial, may have zero, one, two, or three inflection points, but no more than one on the interval $X_i < X < L$ since one is fixed at X equal X_i and another at X equal L. The
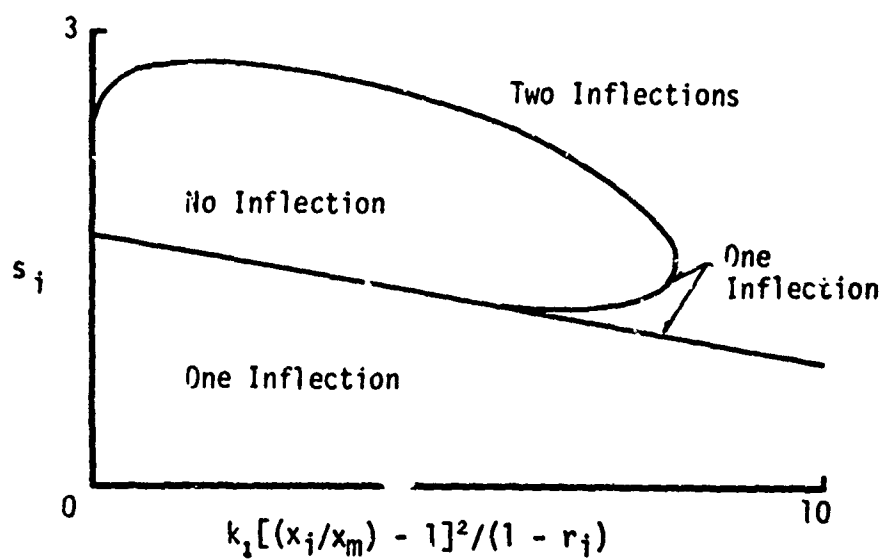
Figure 23. Feasible Region for Noninflected Midbody Section.
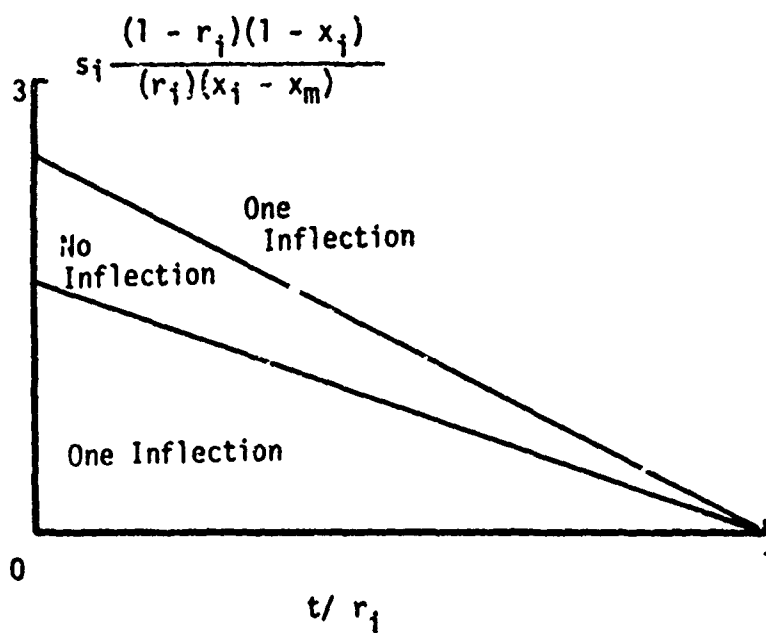
Figure 24. Feasible Region for Noninflected
Tailboom Aftbody Section.

analysis in Appendix E gives the linear convex $[(1 - r_i)(1 - x_i)/(x_i - x_m)(r_i)]s_i$ versus t/r_i boundaries shown in Figure 24. The number of inflections in each region is established by a general analytical treatment.

4.3 Closing Comment

It is apparent that the two classes of bodies considered in this study are constrained in advance to be well behaved according to previous hydrodynamic experience. The profiles are continuous through all derivatives except at a finite number of points which join body sections; at such points the profiles are continuous through second derivatives. The discontinuous third derivative at these points implies that the curvature, while continuous, may change rapidly. Such behavior causes local regions of accelerated flow. It is interesting to note that the search strategies described in Chapter 3 have exploited this phenomenon to help minimize drag, as shown in the next chapter.

CHAPTER 5

RESULTS AND COMPARISONS

This chapter presents results obtained using the drag model and search strategies described in the preceding chapters. Some attention is also given to the hydrodynamic performance of powerful swimmers found in nature. Overall conclusions are reserved for Chapter 6.

5.1 Body D-54 and the "Dolphin"

The impressive performance of the "Dolphin" [2], discussed in Chapters 1 and 2, represents the standard of comparison for the eight-parameter tailboom body. It is of interest to know whether or not a body superior (lower C_D) to the "Dolphin" can be found. Using the Complex Method, an optimization run made early in the study has produced a body with a drag coefficient C_D about 25 percent lower than that of the "Dolphin" at similar Reynolds numbers. The resulting body, called "D-54," and its velocity distribution are shown in Figure 25 along with the "Dolphin" profile. Body D-54 is the 54th function (C_D) evaluation of the optimization run.

Body D-54 is characterized by a long run of laminar boundary layer flow over the forward two-thirds of the body. The small velocity gradients over the forebody help to reduce skin friction; however, the same near-zero gradients have a neutrally stabilizing effect on the laminar boundary layer, i.e., the absence of an accelerating boundary layer increases the chances of early transition. At the midsection the laminar boundary layer is approaching conditions for transition as indicated by the R_θ versus R_S trajectory in Figure 26. Transition is
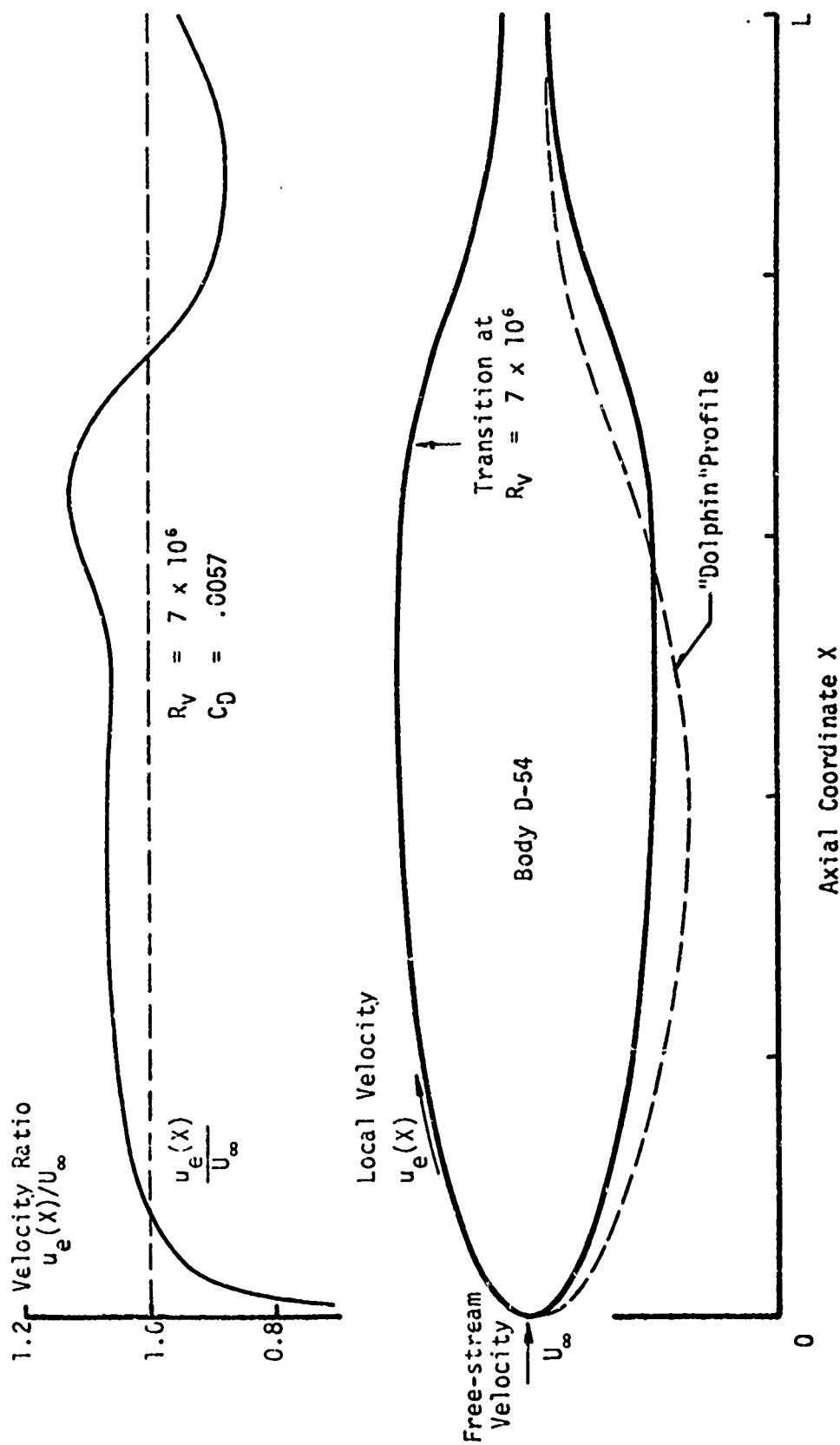
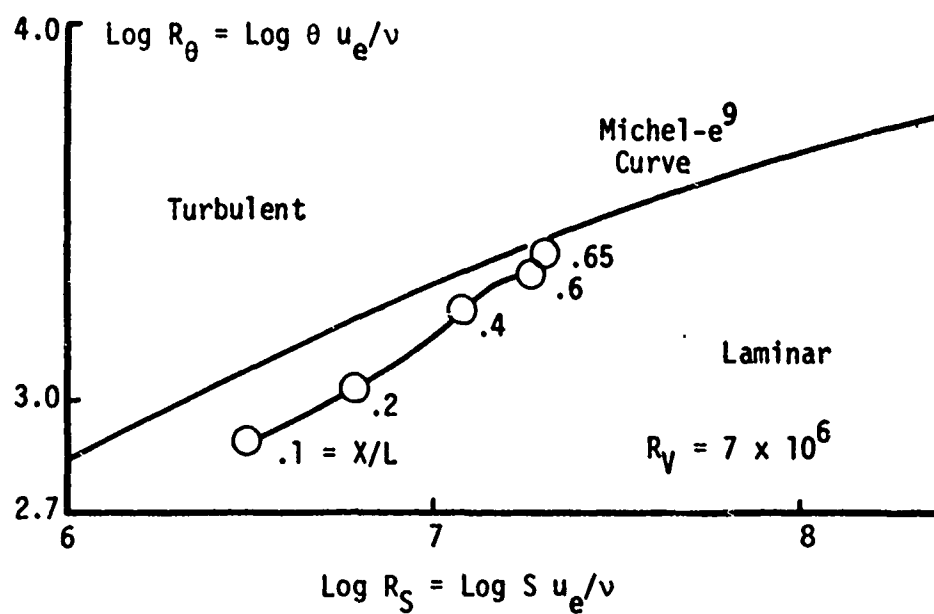Figure 25.. Body D-54 with Velocity Distribution.

Figure 26. R_θ versus R_S for Body D-54.

suppressed, however, by locally accelerating the flow; this is accomplished by allowing the body curvature to change rapidly. After transition, which is indicated by laminar separation/turbulent reattachment, the turbulent boundary layer survives the run of adverse velocity gradient and enters the terminal accelerating region. Such a region helps to suppress boundary layer separation as suggested by the skin friction distribution plotted in Figure 27; we are equating nonzero skin friction and nonseparating flow.

Perturbation studies on body D-54 have been made. The procedure is to randomly generate orthonormal direction vectors $\underline{\delta}$ in Euclidean 8-space. For example, all components of $\underline{\delta}_1$ are randomly generated; each succeeding vector has one less random component so that the remaining components may be used to satisfy orthogonality requirements. Three orthonormal vectors used in this study are shown in Table 1. The reported optimum body shape is represented by the set of parameters $\underline{a}^*$, where for the eight-parameter tailboom body

$$\underline{a}^* = (a_1^*, a_2^*, a_3^*, a_4^*, a_5^*, a_6^*, a_7^*, a_8^*)$$

$$= (f_r^*, x_m^*, k_1^*, r_n^*, r_j^*, s_j^*, x_j^*, t^*) \tag{5.1}$$

Perturbations $\underline{a}'$ about the reported optimum $\underline{a}^*$ are generated by

$$a_j' = a_j^* (1 \pm R\delta_j), \quad j = 1, \ldots, 8 \tag{5.2}$$

where R is the magnitude of the perturbation and δ_j, $j = 1, \ldots, 8$, are the perturbation direction components. Body D-54 and six 3% perturbations are given in Table 2 using the directions of Table 1 and R = .03.

The perturbed drag coefficient values, which include two 6% perturbations not included in Table 2, are shown in Figure 28; it is obvious that body D-54 is suboptimal, a result of prematurely stopping the search after 65 function evaluations. Since the normalized gradients $\partial C_D/\partial$(perturbation direction) are on the order of one, significant improvements in the minimum C_D should be possible.

Table 1. Three Random Orthonormal Directions in Euclidean 8-Space.

Component Number j	Corresponding Parameter	δ_{1j}	δ_{2j}	δ_{3j}
1	f_r	.51355	-.33699	-.14686
2	x_m	-.22359	-.01275	-.08439
3	k_1	.28264	-.33745	.01052
4	r_n	-.06892	-.08269	.09090
5	r_i	.43429	-.11124	.10892
6	s_i	.52863	-.01050	.14185
7	x_i	.08208	.06685	-.96372
8	t	.35616	.86507	.04677
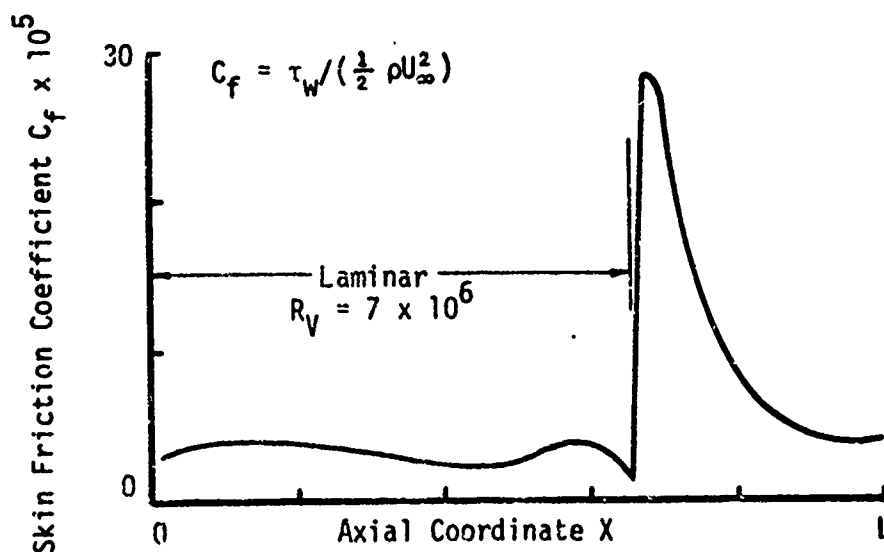
Figure 27. Skin Friction Distribution for Body D-54.

Table 2. Body D-54 with Six 3% Perturbations.

Parameter	Body D-54	Perturbation Corresponding					
		$+\delta_1$	$-\delta_1$	$+\delta_2$	$-\delta_2$	$+\delta_3$	$-\delta_3$
f_r	4.9620	5.0384	4.8855	4.9118	5.0021	4.9401	4.9838
x_m	.5113	.5079	.5148	.5111	.5115	.5100	.5126
k_1	.0961	.0969	.0953	.0952	.0571	.0962	.0961
r_n	.9473	.9453	.9492	.9449	.9496	.9498	.9447
r_i	.6575	.6661	.6490	.6554	.6597	.6557	.6554
s_i	2.4018	2.4399	2.3638	2.4011	2.4025	2.4121	2.3910
x_i	.7482	.7500	.7463	.7497	.7466	.7265	.7698
t	.1833	.1852	.1813	.1880	.1785	.1835	.1830
$*k_{1m}$	.0602	.0660	.0549	.0601	.0603	.0509	.0702
$*si_a$	1.3302	1.2529	1.4008	1.3248	1.3356	1.5718	1.1257
t/r_i	.2787	.2781	.2794	.2869	.2706	.2762	.2792

$$* \; k_{1m} = \left(\frac{x_i}{x_m} - 1\right)^2 k_1/(1 - r_i)$$

$$* \; si_a = (1 - r_i)(1 - x_i) \, s_i/[r_i(x_i - x_m)]$$
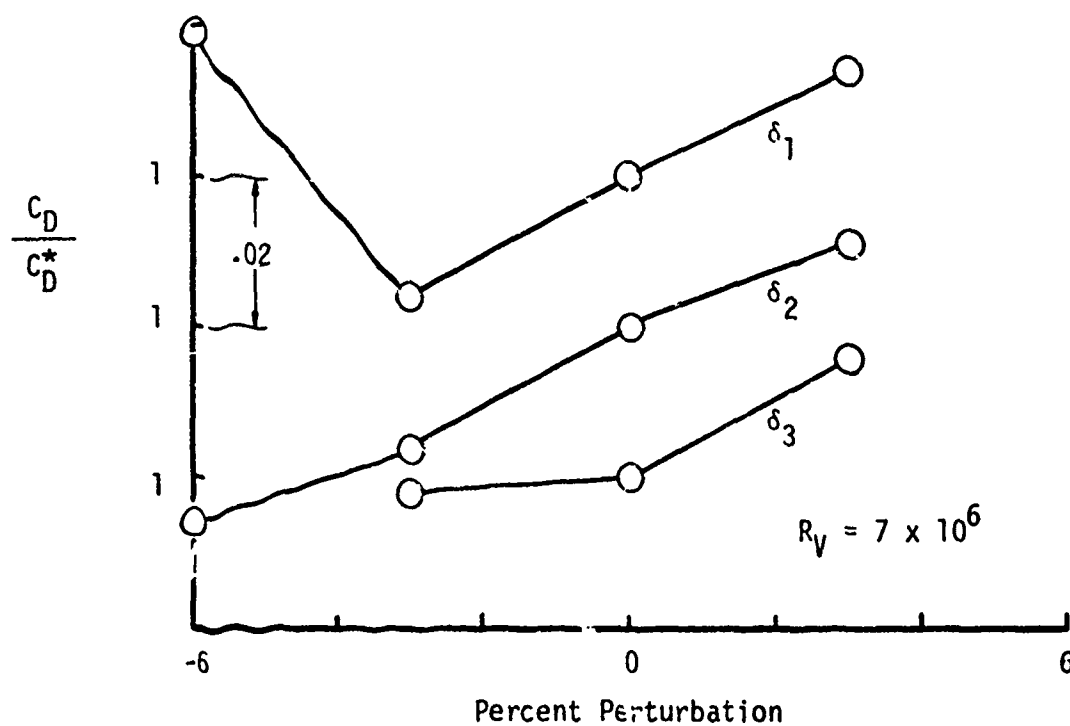
Figure 28. Perturbation Results for Body D-54.

5.2 All-Turbulent Body I-36 and the Series 58 Study

The philosophy of the Series 58 study [3], discussed in Chapters 1 and 2, is to design low drag bodies on the assumption that laminar flow cannot exist in the operating environment at submarine-type Reynolds numbers. No attempt is made here to judge the validity of this assumption; rather, it is of interest to know whether or not an all-turbulent body can be found with a C_D lower than that of the best of the Series 58 bodies.

Using the Complex Method and the five-parameter pointed tail body, three optimization runs with different initial complex figures have been made. The boundary layer is tripped at X/L equals .05; for all three runs the Reynolds number is fixed at R_V equals 5×10^6 which is the upper end of the Series 58 test R_V values. Two of the three runs converged after 27 function evaluations; the third run was near convergence but was aborted prematurely after 38 function evaluations due to reasons external to the search strategy.

The significant result of the three runs is the fact that the response surface for all-turbulent bodies is quite flat. That is, for fairly wide variations in the parameters, the drag coefficient varies little. This is evident in Figure 29 which shows nine parameter sets plotted in the parameter space. All parameter sets have corresponding C_D values within one percent of the best design. It is evident that low drag all-turbulent bodies are not critically dependent on shape. Hence, if laminar boundary layers cannot be exploited to minimize drag, then means other than profile shaping must be used to reduce drag, e.g., polymer injection.

The best design, body "I-36," and its velocity distribution are shown in Figure 30 along with the profile of model 4165, the best of the Series 58 study. The C_D value for body I-36 is 0.020, which is about the same as that of model 4165 according to the drag model used in this study The streamwise velocity gradient is small over most of the body length to reduce skin friction.
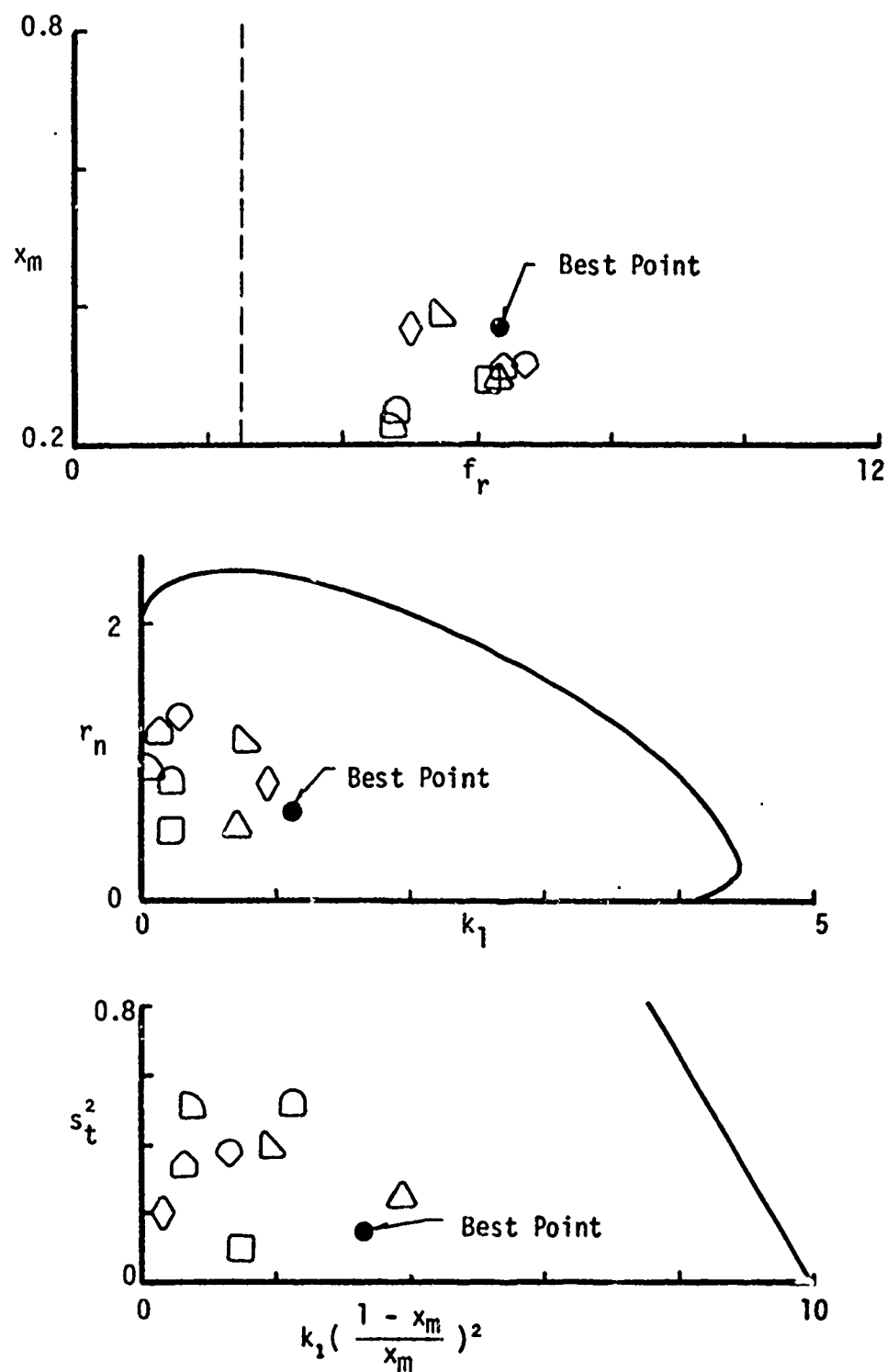
Figure 29. Parameters for Nine All-Turbulent Bodies within One Percent of Best C_D Value at $R_V = 5 \times 10^6$.
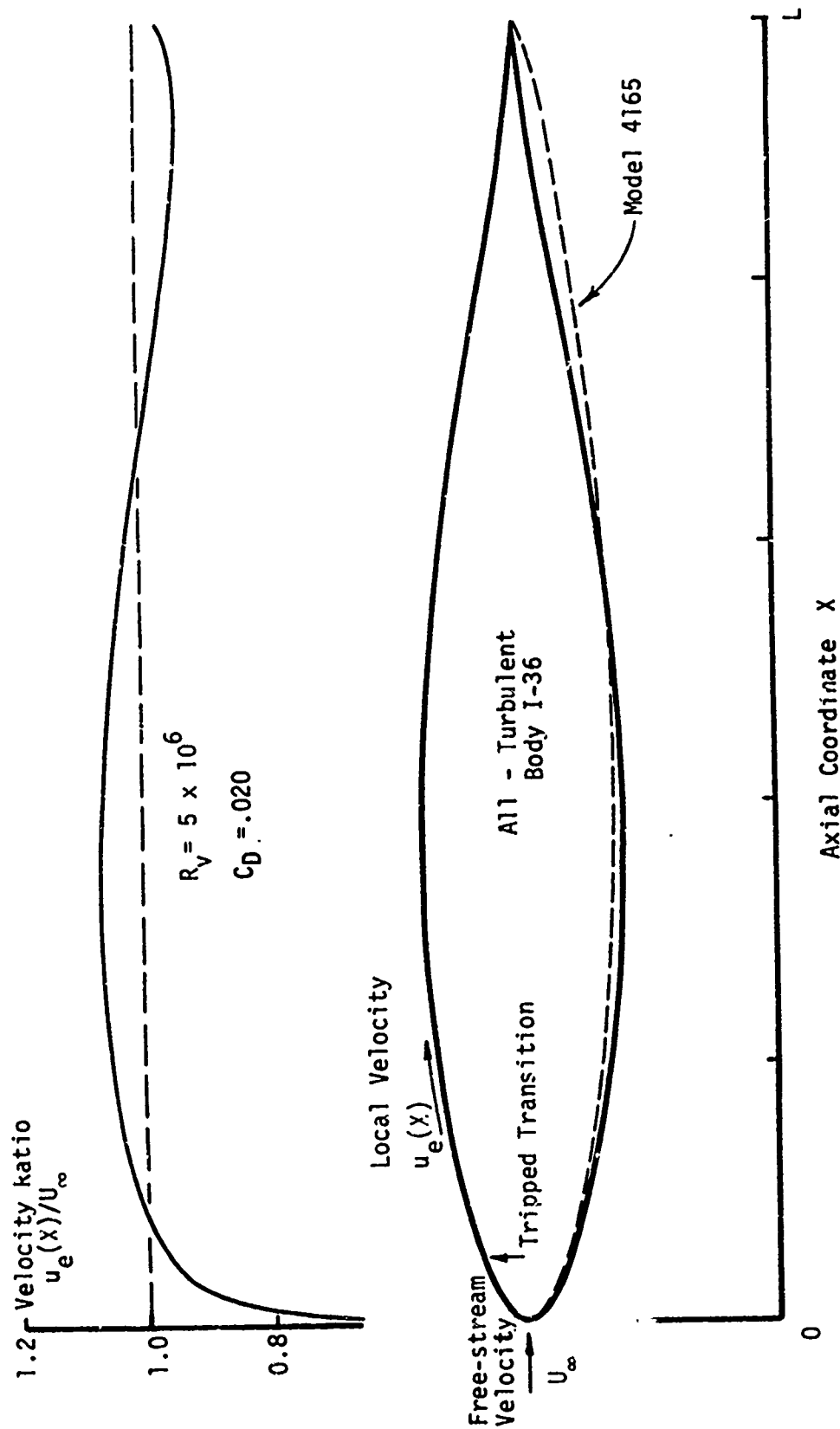
Figure 30. All-Turbulent Body I-36 with Velocity Distribution.

5.3 A Series of Laminar Bodies at Three Reynolds Numbers

Of primary interest is the change of minimum drag shape over a wide range of Reynolds numbers. An underlying topic of fundamental importance is the uniqueness of a minimum drag shape at its design Reynolds number. In this section we report the results of optimization runs made at three Reynolds numbers using the five-parameter pointed-tail body described in Chapter 4. The selected Reynolds numbers are $R_V = 5 \times 10^6$, 1.6×10^7, and 5×10^7 which correspond to nominal vehicle volumes of 1.1, 37, and 1130 cubic feet traveling at a speed of 35 knots in water.

Low R_V Body G-35. Using the Complex Method a low drag body shape has been obtained at $R_V = 5 \times 10^6$. The optimization run terminates prematurely after 43 function evaluations due to reasons external to the search strategy. The best body shape occurs on the 35th function evaluation of the run; its predicted C_D value is 0.0054 at the design R_V.

Body G-35 and its velocity distribution are shown in Figure 31. The body is quite streamlined and has a long run of laminar boundary layer flow over the forward three-quarters of the body. The forebody is essentially of the Reichardt type since the velocity gradient is nearly zero over most of the forward half of the body. In a manner similar to the tailboom body D-54, the flow is locally accelerated starting at about X/L equal 0.6 to suppress transition, which is predicted by laminar separation/turbulent reattachment. The effect is readily seen in the R_θ versus R_S trajectory plotted in Figure 32. The skin friction distribution plotted in Figure 33 suggests that the turbulent boundary layer is on the verge of separating near the trailing edge.

Perturbation studies have been made to determine if body G-35 is near a local minimum. The parameters of the reported optimum in a Euclidean 5-space are

$$\underline{a}^* = (a_1^*, a_2^*, a_3^*, a_4^*, a_5^*)$$
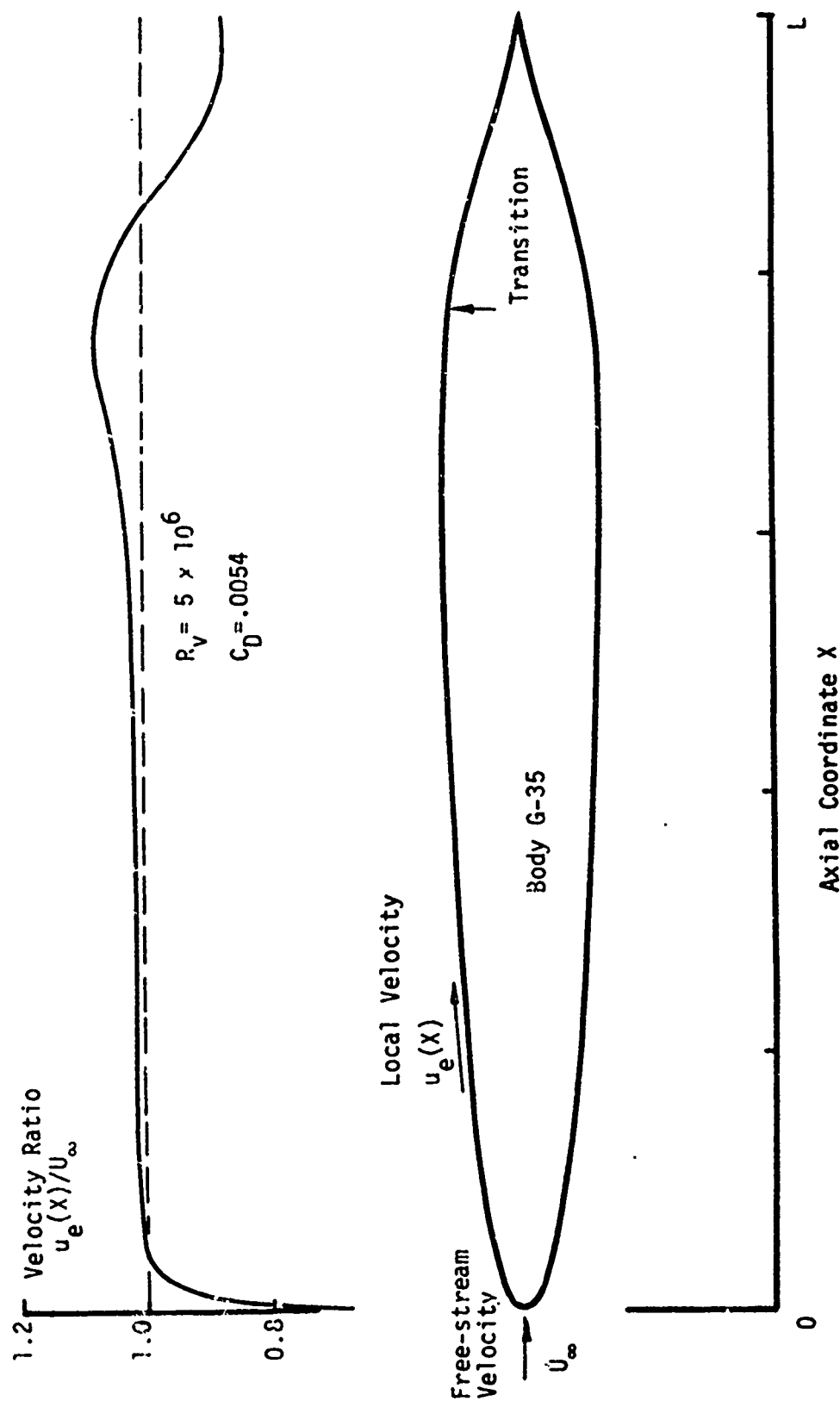$$= (f_r^*, x_m^*, k_1^*, r_n^*, s_t^{*2}) \tag{5.3}$$

Figure 31. Body G-35 with Velocity Distribution.
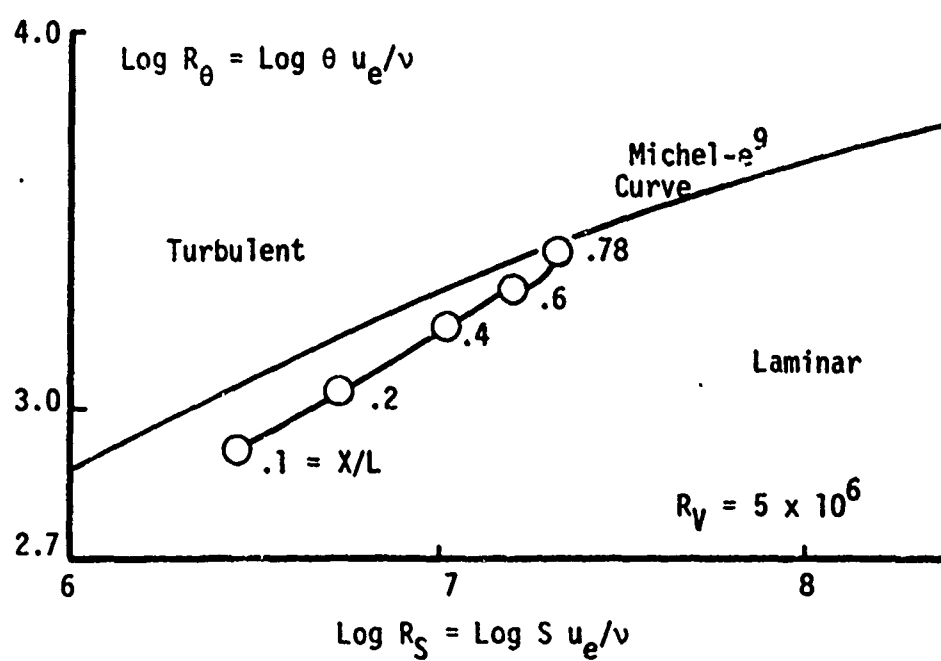
Figure 32. R_θ versus R_S for Body G-35.
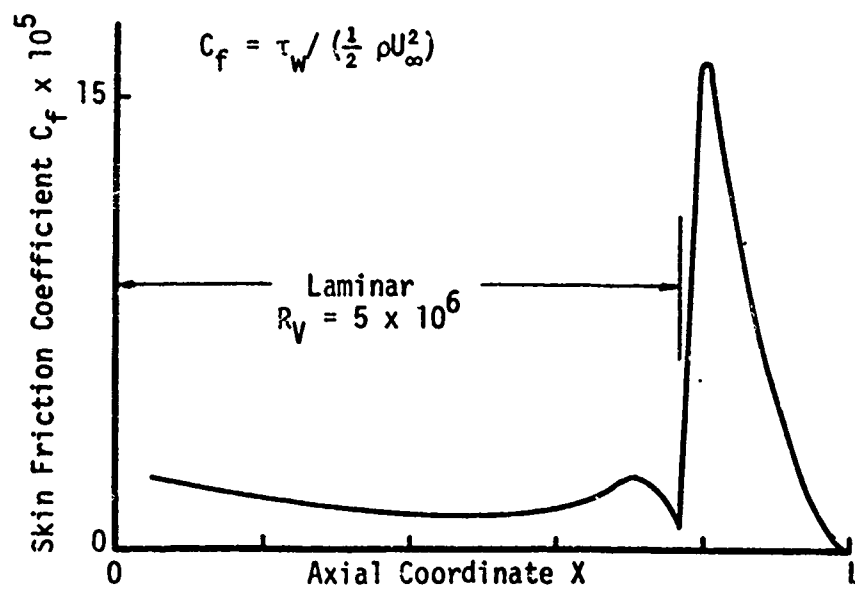
Figure 33. Skin Friction Distribution for Body G-35.

As for the eight-parameter body D-54, random orthonormal directions, shown in Table 3, are used to generate perturbations

$$a'_j = a^*_j(1 \pm R\delta_j), \quad j = 1, \ldots, 5 \tag{5.4}$$

where R is the perturbation magnitude and the δ_j, $j = 1, \ldots, 5$, are the components of the perturbation direction. The parameters for body G-35 and six 3% perturbations (R = .03) using the directions in Table 3 are shown in Table 4. The perturbation results, shown in Figure 34, reveal immediately that body G-35 is suboptimal. The normalized gradients $\partial(C_D)/\partial$(perturbation direction) are on the order of one so that significant improvement in the minimum C_D should be possible.

Midrange R_V Body H-62.

Using the Complex Method a low drag body shape has been obtained at $R_V = 1.6 \times 10^7$. The optimization run terminates after 80 function evaluations, the last improvement occurring on the 62nd evaluation.

Body H-62 and its velocity distribution are shown in Figure 35; the C_D value is .0059 at the design R_V value. The body is somewhat "fatter" and more pointed than the low R_V body G-35. A long run of laminar boundary layer flow is maintained by continuously but mildly accelerating the flow over the forward two-thirds of the body. Transition is predicted by the Michel-e[9] correlation, as indicated by the R_θ versus R_S trajectory plotted in Figure 36. The skin friction distribution shown in Figure 37 suggests that the turbulent boundary layer is on the verge of separating near the trailing edge in a manner similar to body G-35.

Perturbation studies have been made on body H-62 using the perturbation directions given in Table 3. The procedure is the same as for body G-35. The parameters for body H-62 and six 3% perturbations (R = .03) are shown in Table 5. The perturbation results are shown in Figure 38; direction $\underline{\delta}_1$ reveals that body H-62 is suboptimal and that improvement in the minimum C_D value is possible.

High R_V Bodies F-57 and F2-49.

Using both the Complex Method and Powell's Method two distinct low drag shapes have been obtained at

Table 3. Three Random Orthonormal Directions in Euclidean 5-Space.

Component Number j	Corresponding Parameter	δ_{1j}	δ_{2j}	δ_{3j}
1	f_r	.03552	.29310	-.37469
2	x_m	.67730	.33316	.15350
3	k_1	.47704	.35274	-.38945
4	r_n	-.16526	-.16275	-.82370
5	s_t^2	-.53397	.80758	.07677

Table 4. Body G-35 with Six 3% Perturbations.

Parameter	Body G-35	Perturbation Corresponding to					
		$+\delta_1$	$-\delta_1$	$+\delta_2$	$-\delta_2$	$+\delta_3$	$-\delta_3$
f_r	8.0037	8.0122	7.9952	8.0741	7.9333	7.9137	8.0937
x_m	.6808	.6946	.6669	.6876	.6740	.6839	.6776
k_1	1.3360	1.3551	1.3169	1.3501	1.3219	1.3204	1.3516
r_n	1.2437	1.2375	1.2499	1.2376	1.2498	1.2130	1.2744
s_t^2	.1211	.1192	.1231	.1241	.1182	.1214	.1209
$* k_{1a}$	.2938	.2620	.3284	.2788	.3094	.2821	.3059

$$* \ k_{1a} = k_1 \left(\frac{1 - x_m}{x_m} \right)^2$$
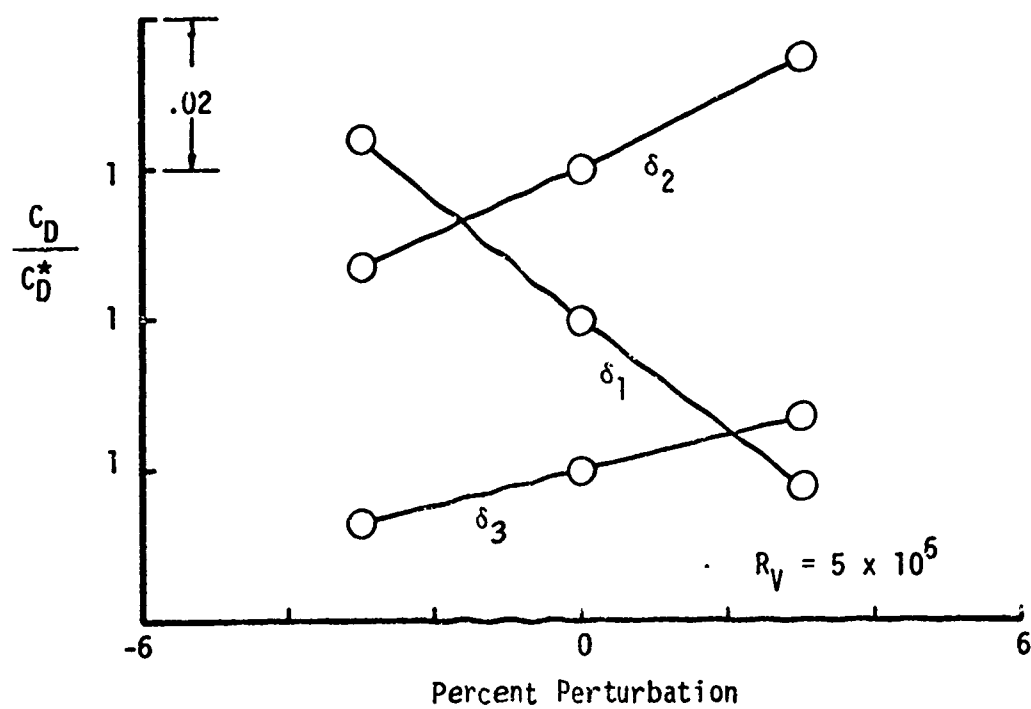
Figure 34. Perturbation Results for Body G-35.
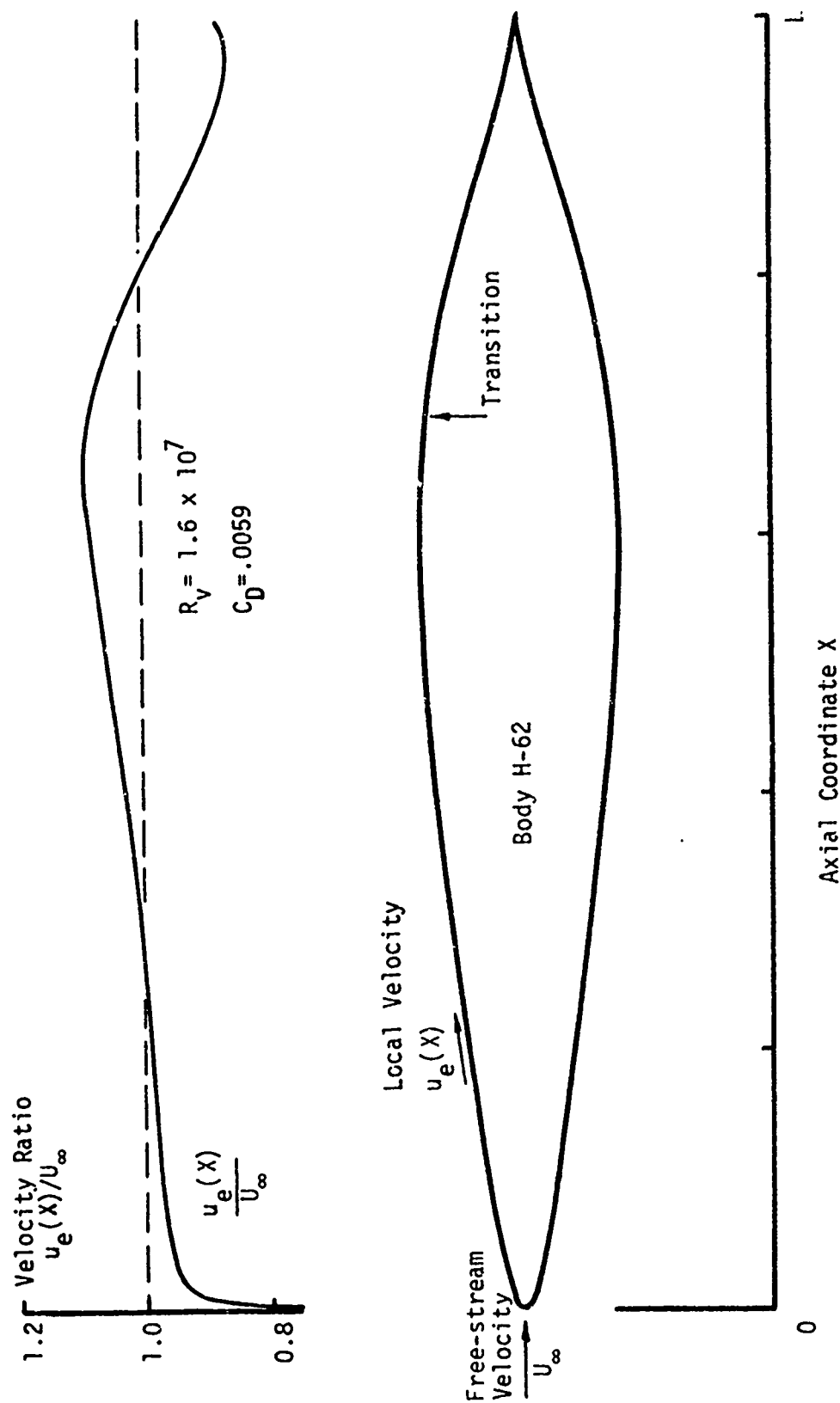
Figure 35. Body H-62 with Velocity Distribution.
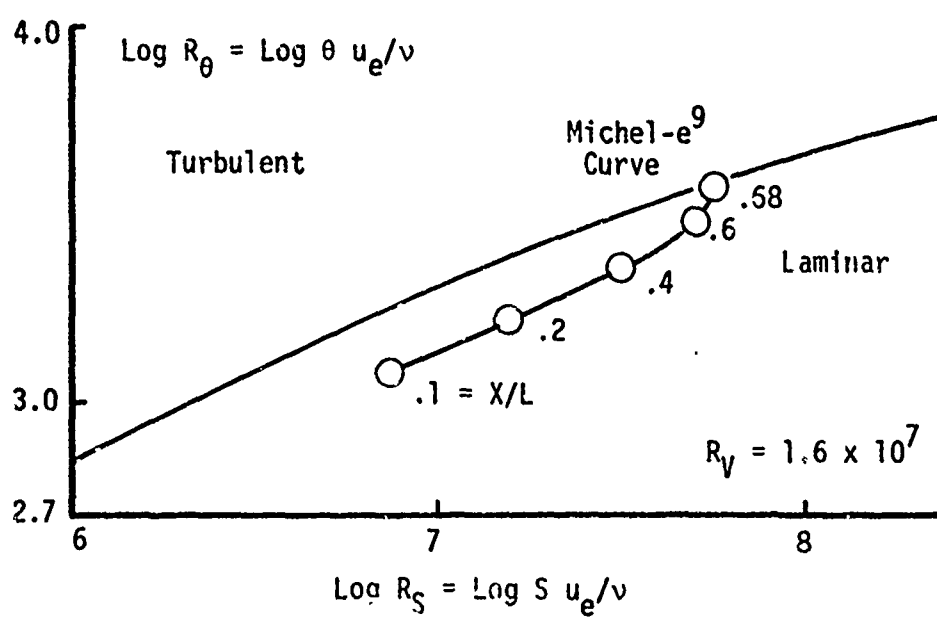
Figure 36. R_θ versus R_S for Body H-62.
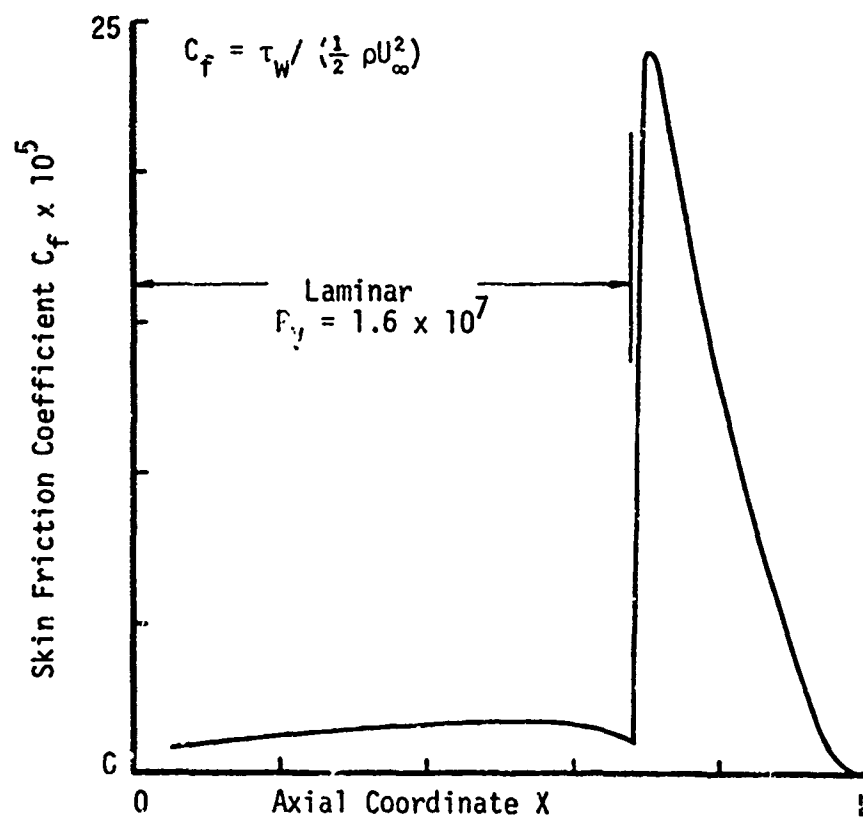
Figure 37. Skin Friction Distribution for Body H-62.

Table 5. Body H-62 with Six 3% Perturbations.

Parameter	Body H-62	Perturbation Corresponding to					
		$+\delta_1$	$-\delta_1$	$+\delta_2$	$-\delta_2$	$+\delta_3$	$-\delta_3$
f_r	6.4059	6.4127	6.3991	6.4622	6.3496	6.3339	6.4779
x_m	.5995	.6116	.5873	.6055	.5935	.6022	.5967
k_1	3.4942	3.5442	3.4442	3.5312	3.4572	3.4534	3.5350
r_n	.2672	.2658	.2685	.2659	.2685	.2640	.2703
s_t^2	.3409	.3355	.3464	.3492	.3327	.3417	.3401
$*\,k_{1a}$	1.5600	1.4289	1.7010	1.4996	1.6222	1.5067	1.6149

$$* \; k_{1a} = k_1 \left(\frac{1 - x_m}{x_m} \right)^2$$
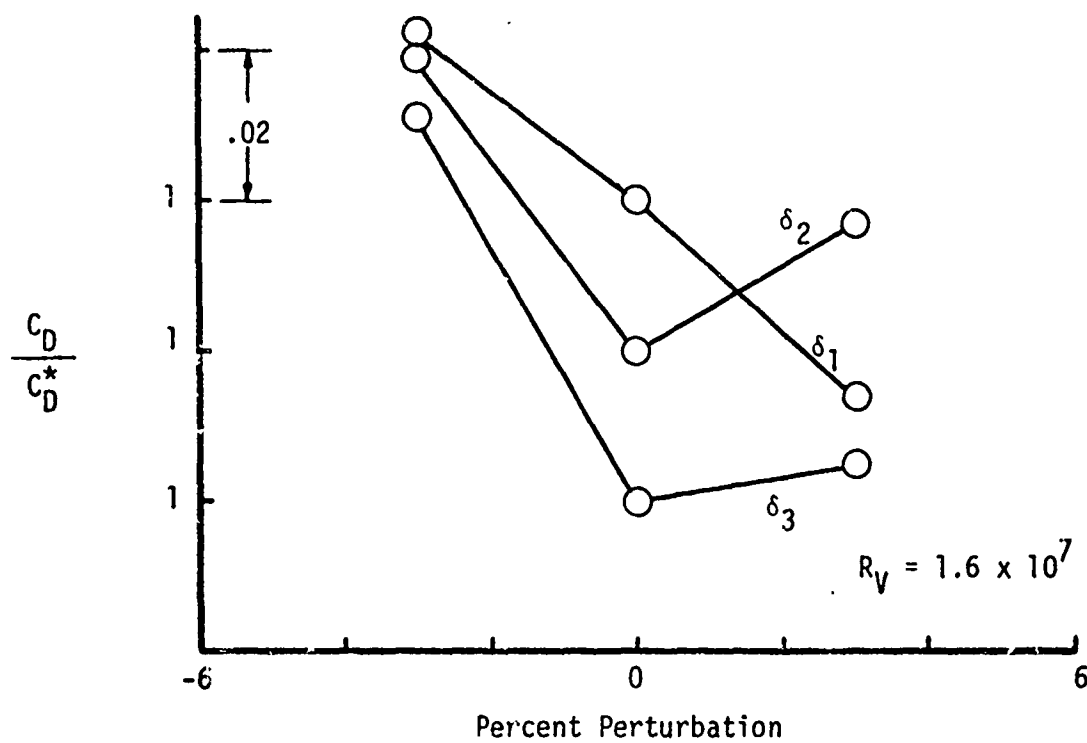
Figure 38. Perturbation Results for Body H-62.

$R_V = 5 \times 10^7$. One optimization run using the Complex Method is terminated after 90 function evaluations, the best design occurring on the 57th iteration (body F-57). A second run using the Complex Method is terminated after 70 function evaluations producing a different best shape on the 49th iteration (body F2-49). A third run using Powell's Method is terminated after 75 function evaluations with a best shape quite similar to body F2-49. None of the three runs converges according to the formal definitions associated with the methods.

Body F-57 and its velocity distribution are given in Figure 39; the drag coefficient is .0076. This "fat" body has some hydrodynamic similarity to body H-62 in that it is pointed and has a long run of accelerated laminar flow over the forward two-fifths of the body. Unlike the lower R_V body shapes, there is no dominant locally accelerated flow to suppress transition. The absence of the effect is seen in Figure 40 in which the R_θ versus R_S trajectory approaches the Michel-e[9] correlation curve in a monotonic manner, ultimately crossing the curve to predict transition. The skin friction distribution shown in Figure 41 suggests that the turbulent boundary layer is on the verge of separating near the trailing edge.

Body F2-49 and its velocity distribution are given in Figure 42; the drag coefficient is .0073 so that it is superior to body F-57 on the basis of minimum C_D. This shape also has hydrodynamic similarity to body H-62 in that a small run of nearly constant velocity flow precedes a large region of accelerated flow which helps to suppress transition. This effect is seen in Figure 43 in which the R_θ versus R_S trajectory approaches, veers away, and approaches again the Michel-e[9] correlation curve; its ultimate crossing predicts transition. In a manner similar to all the preceding pointed tail bodies, the skin friction distribution shown in Figure 44 suggests that the turbulent boundary layer is on the verge of separating near the trailing edge.

It is interesting to note that each of the two low drag shapes exploits a different feature of the midrange R_V body H-62 to minimize drag. That is, the pointed-nose body F-57 maintains laminar flow by continuously accelerating the flow over the forebody; the rounded-nose body F2-49 suppresses transition by locally accelerating the flow
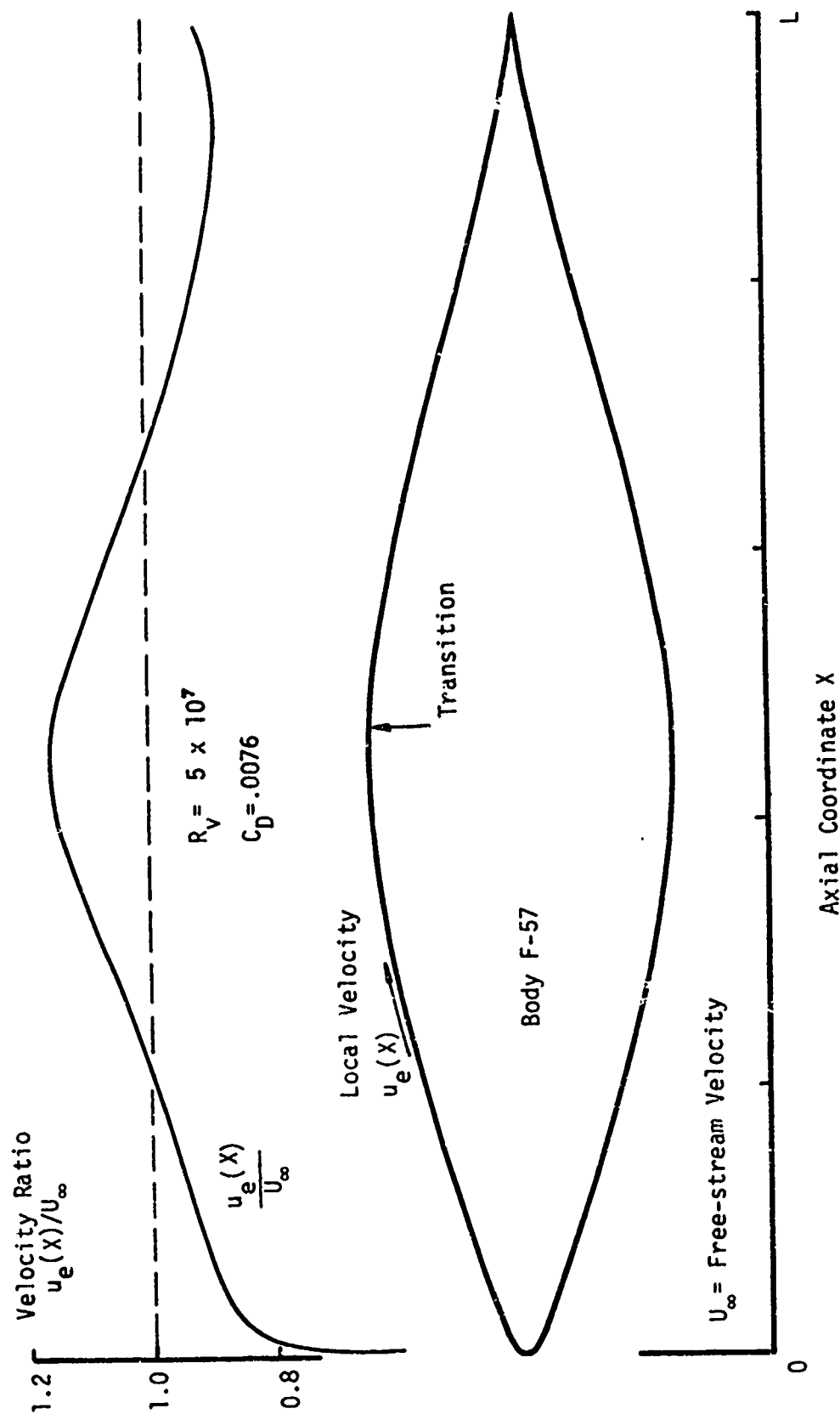
Figure 39. Body F-57 with Velocity Distribution.
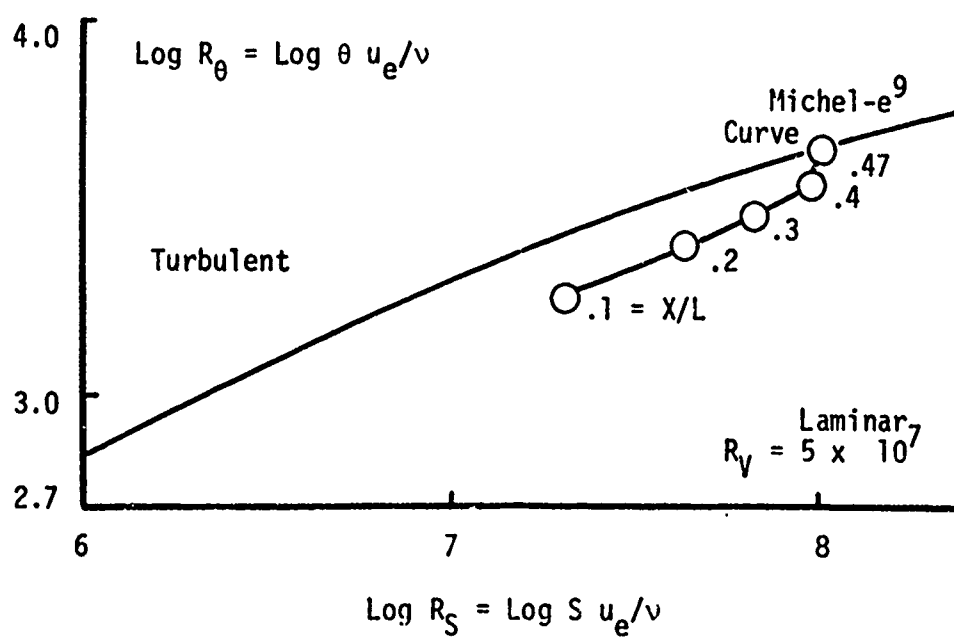
Figure 40. R_θ Versus R_S for Body F-57.
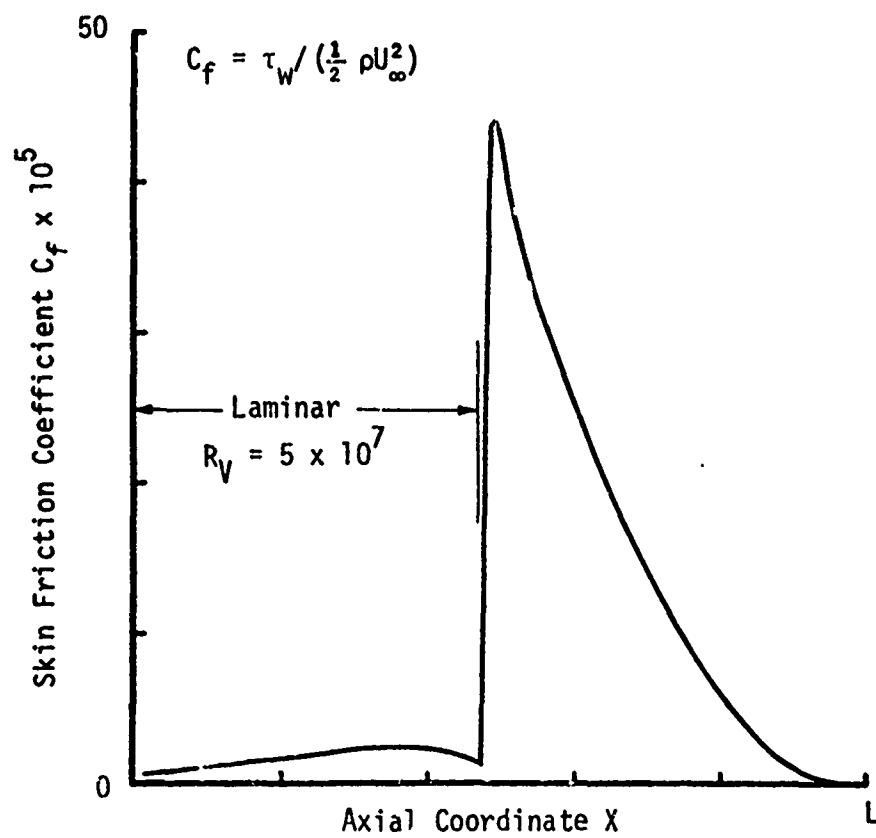
Figure 41. Skin Friction Distribution for Body F-57.
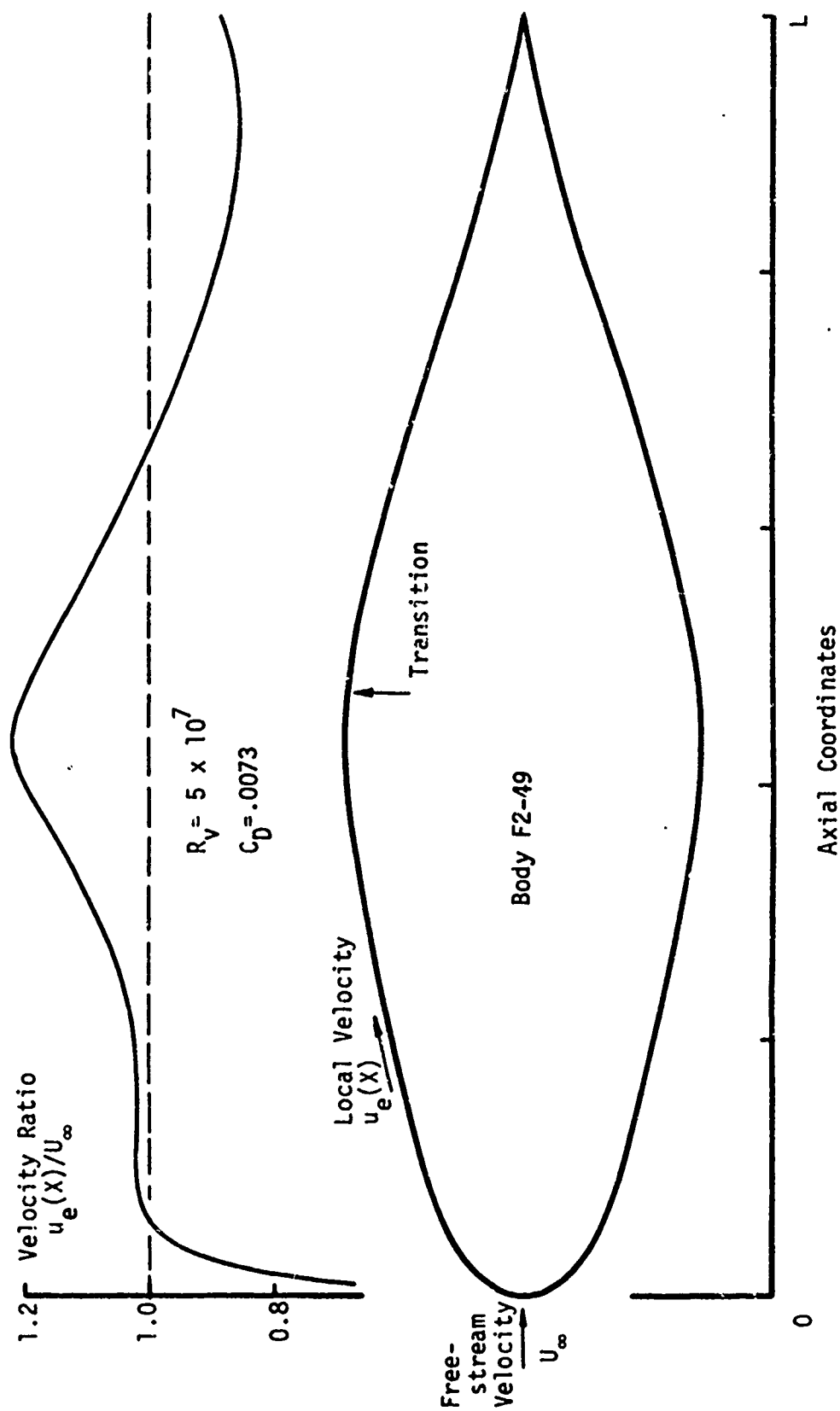
Figure 42. Body F2-49 with Velocity Distribution.
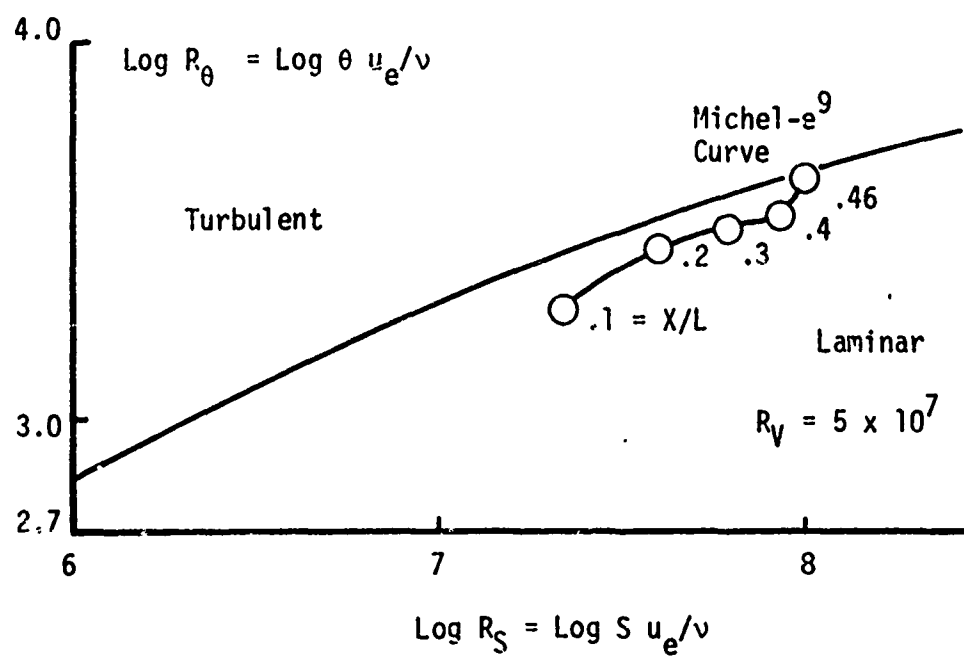
Figure 43. R_θ Versus R_S for Body F2-49.
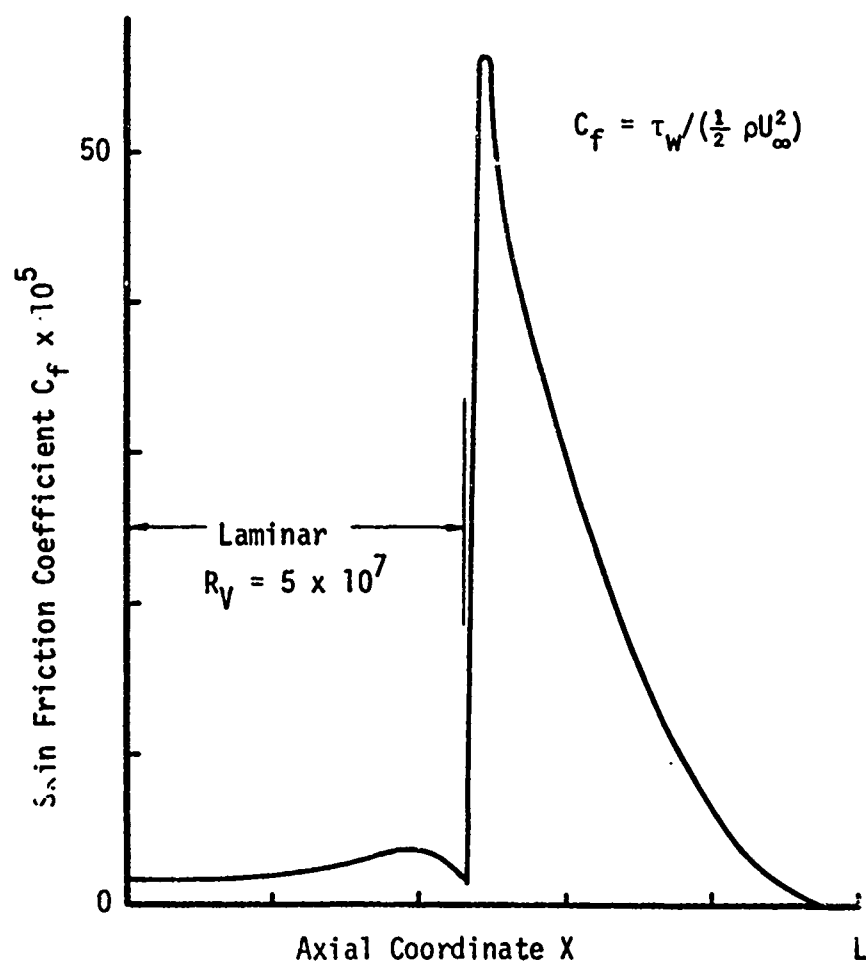
Figure 44. Skin Friction Distribution for Body F2-49.

starting at about X/L equal 0.2. Even though the hydrodynamic means are somewhat different, transition occurs at about the same axial location for both bodies.

The existence of these two distinct low drag shapes brings the question of uniqueness into the foreground. In an attempt to establish uniqueness, i.e., the existence of a finite number of distinct low drag shapes, a third optimization run has been made using Powell's Method; the idea is to see whether a different search strategy converges to an existing solution or produces yet another low drag design. If the former occurs, then confidence in the uniqueness of the solutions has increased. If the latter occurs, then nonuniqueness appears likely and further testing is required.

The results of the Powell run are best seen by observing the overall parameter migrations of all three optimization runs as shown in Figure 45. The data shown are the initial and final designs for each run; the arrowhead indicates direction of overall movement. For the runs using the Complex Method, the initial design shown is the best vertex of the initial complex figure. It can be seen that both final designs are similar in their parameter values except for the radius of curvature at the nose r_n. It should be noted that small differences in x_m are exaggerated on the $k_1[(1 - x_m)/x_m]^2$ axis. The result of the Powell search is quite close to body F2-49 and appears to be converging on the r_n - k_1 boundary. The conclusion to be drawn is that the low drag designs are distinct local minima, finite in number, and hence unique.

Variation of C_D with Reynolds Number. One sensitivity analysis of interest to the hydrodynamic designer is the variation of drag coefficient with Reynolds number. The variation of C_D over a wide range of R_V is shown in Figure 46 for low, midrange, and high R_V bodies. At its own design point each low drag body has the lowest C_D of the three values. The designs are not sensitive to reasonably wide variations in R_V, at least according to predictions of the drag model used in this study.
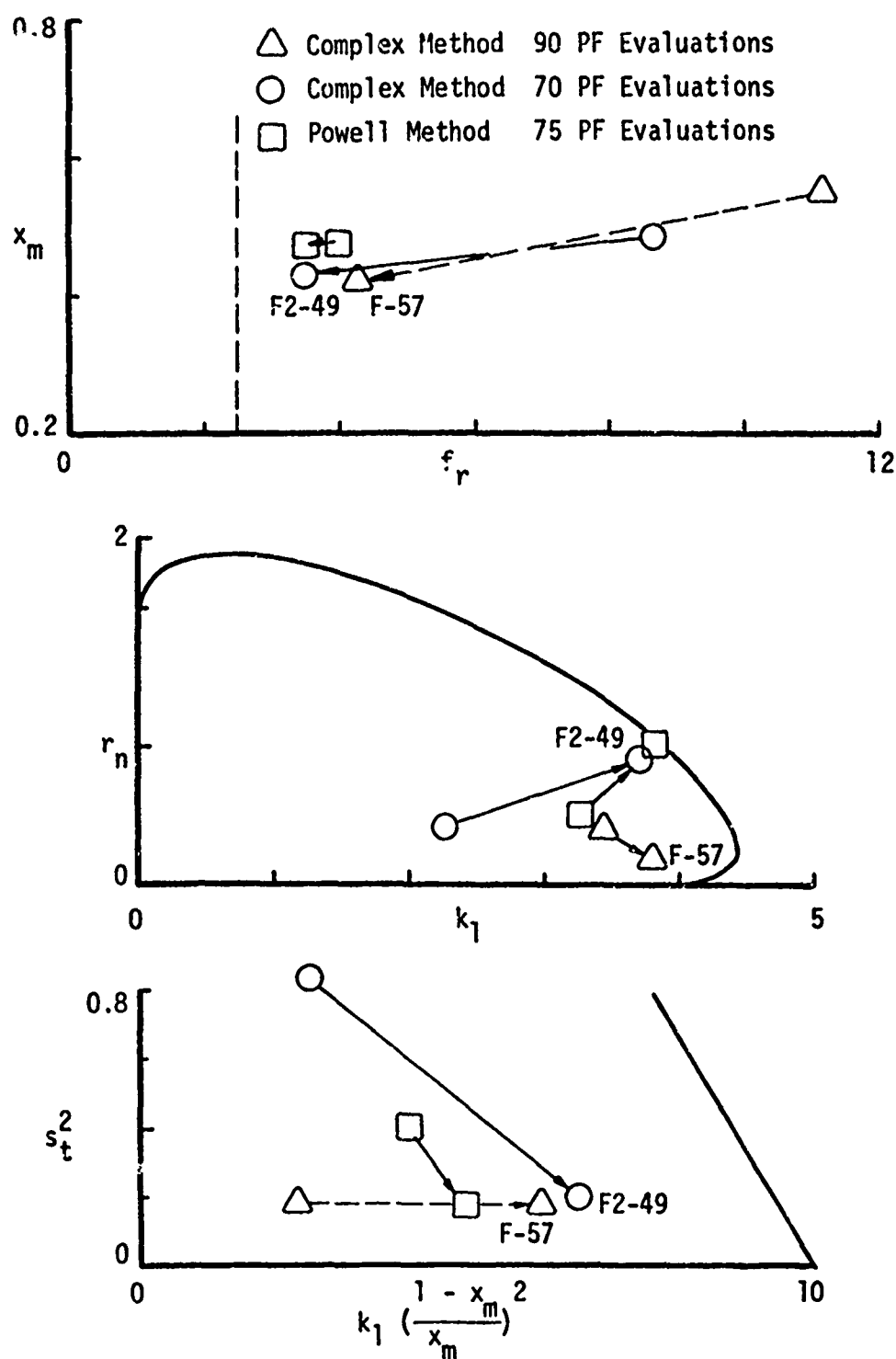
Figure 45.   Parameter Migrations during Three
Optimization Runs at $R_V = 5 \times 10^7$.
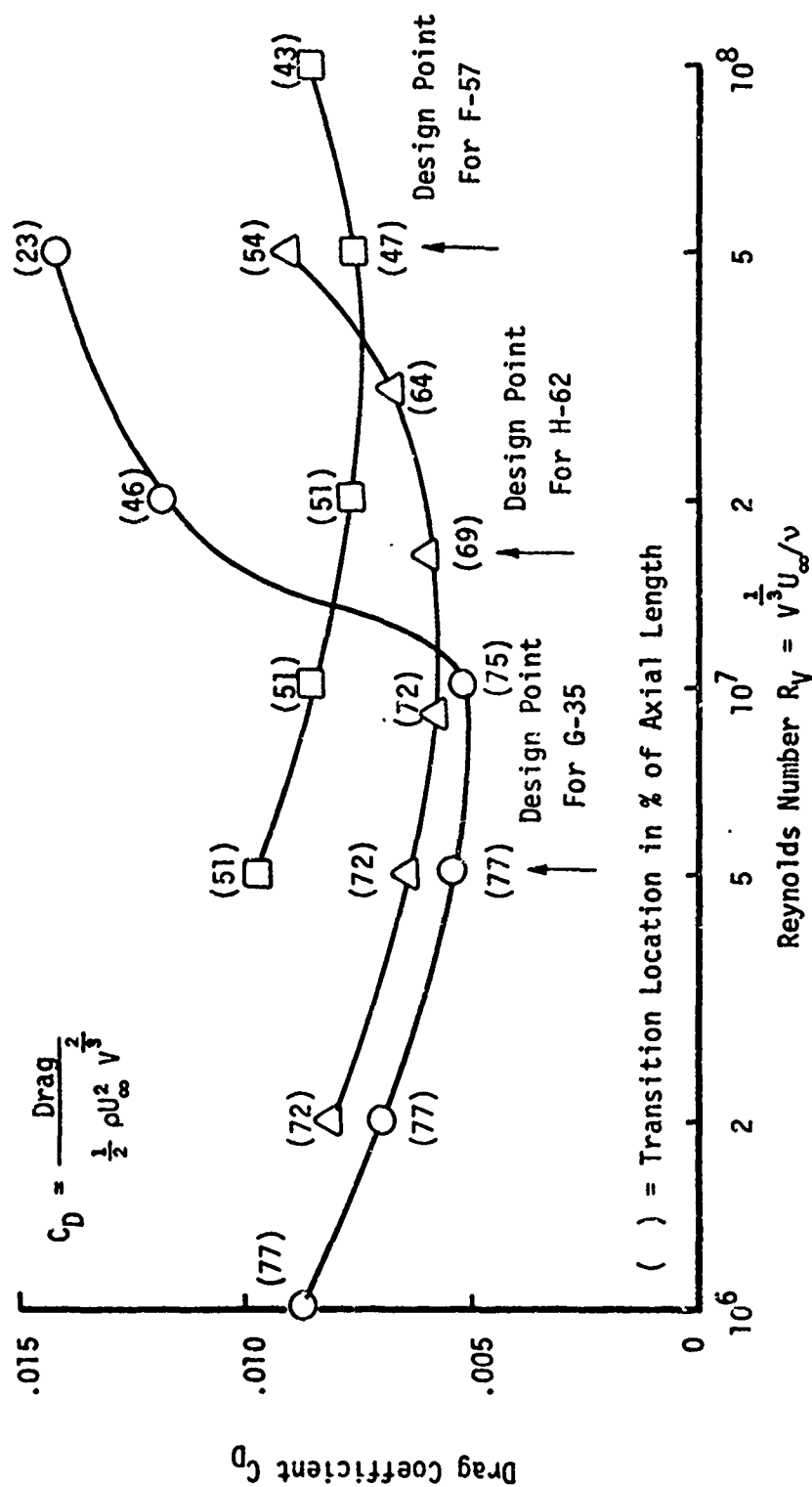
Figure 46. Variation in C_D with R_V for Three Low Drag Bodies.

5.4 Hydrodynamic Performance of Powerful Swimmers

Data on the swimming speeds of dolphins (porpoises) have appeared
in the literature since the mid 1930's. Until the early 1960's all
data indicated that dolphins either 1) produced several times the power
believed possible by their musculature, or 2) were able to reduce their
flow resistance by unknown means to values several times lower than
those of similar man-made devices [31, 32]. However, recent studies
[33, 34] have shown through reasonably well controlled experiments that
the dolphin does not have low resistance to flow; indeed, typical drag
coefficients are about the same as that of a torpedo with an all-turbu-
lent boundary layer. Stated another way, there are rigid laminar flow
bodies with drag coefficients about half that of the dolphin animal.
A tested example of such a man-made device is the "Dolphin" [2] dis-
cussed in Chapters 1 and 2.

Table 6 compares drag data taken from the references indicated for
a nominal R_V of 5 x 10^6. Data for the porpoise species are usually
reported on a dimensional basis so that direct comparisons are difficult
to make, item 1 of Table 6 being a rare exception. It is apparent from
the table that the Stenella attenuata has a drag coefficient more like
torpedoes and all-turbulent bodies than like laminar flow devices. It
must be concluded that porpoises, as hydrodynamic performers, are
mediocre.

There are at least three reasons why the earlier conclusions con-
cerning the hydrodynamic abilities of the dolphin are erroneous [33, 34].
Unusually high speeds of dolphins swimming near moving ships may be
explained by assisted locomotion since it is known that dolphins are able
to derive thrust from the moving fluid near the ship. Some speeds have
been deduced from dolphin sightings by observers on moving ships over a
quarter-mile distance [32]. However, the combination of ship motion and
wave motion creates an illusion of fast speed which has been estimated
to cause errors of 25% [34]. A more subtle source of error is the
duration of time over which the speeds are recorded. Dolphins are
capable of high power output and hence high speeds for short periods of
time, perhaps 5 to 10 seconds, during which the muscle tissue goes into

Table 6.   Porpoise Drag Data Compared with Rigid
Devices for Nominal R_V of Five Million

Animal or Device	$\dfrac{\text{Drag *}}{\frac{1}{2}\,\rho U_\infty^2 A}$	$\dfrac{\text{Drag}}{\frac{1}{2}\,\rho U_\infty^2 V^{\frac{2}{3}}}$	Comments and References
1. Porpoise, <u>Stenella attenuata</u>	.00239 to .00401	-	Drag due to appendages subtracted out. Data from coasting tests (1966) [34].
2. Typical Torpedo	-	.0196	[2]
3. Model 4165 of Series 58	.00255	.0186	All turbulent boundary layer. Tow tank data [3].
4. Laminar Flow "Dolphin"	.00109 to .00164	.0092 to .0138	Data from gravity-powered drop tests [2].

* A = body wetted surface area

oxygen debt. One series of tests [33] showed that the dolphin attained a speed of 16.1 knots for 7.5 seconds but only 6 knots on a continuous basis. For this example the ratio of peak power to continuous power is approximately $(16.1/6)^3 = 19.2$. Apparently the concept of peak power has not been considered, or at least has not been stated, in earlier work.

In comparing the shapes of powerful swimmers to those of rigid low drag bodies, one important fact must be emphasized: the optimum shape for swimming animals will be different from the optimum shape of low drag man-made devices. The underlying reason is that the animals and devices are optimally shaped with respect to different performance functions. The animal is shaped so as to maximize its chances for survival, which is a rather complex performance function indeed! On the other hand, the shapes of similar man-made devices, as proposed to date, are optimal with respect to the relatively uncomplicated performance function of drag. The powerful swimmer is shaped so as to attempt to simultaneously minimize drag, maximize propulsion, maximize energy reserves, minimize the effect of interfering objects such as eyes, mouth, and gills, and minimize its metabolism rate while swimming quickly. To extremize any one of these items without regard for the others would certainly change the shape of the animal.

Of equal importance is the fact that the powerful swimmers are optimally shaped subject to a different set of constraints than those for man-made devices. Animals are constrained to utilize propulsion mechanisms which oscillate rather than rotate since all parts of the animal must be connected with blood vessels and nerves. There is also the subtle constraint of maintaining a favorable surface-area-to-volume ratio so that the organism may function properly [35]. Man-made devices are practically constrained to use rotating mechanisms for propulsion since oscillating mechanisms of rigid parts apparently cannot be made to operate efficiently. Implied here is the additional practical constraint of rigid construction and structural integrity.

The point to be made here is that it is not particularly meaningful to compare the shapes of powerful swimmers and low drag rigid devices. Each is the result of attempting to extremize different performance functions subject to different constraints.

CHAPTER 6

CONCLUSIONS AND RECOMMENDATIONS

Conclusions and recommendations given in this chapter are based
on results reported in Chapter 5 and Appendix F. At the outset it must
be said that significant vehicle drag reduction is possible through shape
manipulation. The present method has produced low drag bodies with drag
coefficients one-fourth to one-third below that of the low drag "Dolphin"
at similar Reynolds numbers. Of equal significance is the fact that the
minimum drag shape is a strong function of Reynolds number. For the
five-parameter body over a one order-of-magnitude range of Reynolds
number ($5 \times 10^6 < R_V < 5 \times 10^7$) the corresponding optimum fineness ratio
(L/D) ranges nominally from 8.5 to 3.5. The corresponding location of
maximum diameter ranges nominally from X_m/L = .75 to .45.

Over the reported R_V range all optimum body shapes exploit laminar
boundary layers to reduce drag. The experimental evidence of the "Dol-
phin" [2] demonstrates that substantial laminar flow does exist in the
ocean environment at speeds up to 60 knots (R_V above 10^7). It must be
concluded that laminar flow is a practical means for reducing drag at
these Reynolds numbers and that proper body shaping can use laminar
flow effectively.

If laminar flow is prevented due to extraneous factors, such as
body roughness, then it appears that the body shape is not particularly
critical in reducing drag so long as it is reasonably streamlined. This
conclusion is based on the all-turbulent drag minimization study at
$R_V = 5 \times 10^6$ in which nothing better than the best of the Series 58
study [3] is obtained. Stated another way, if laminar flow cannot be
exploited to reduce drag, then further drag reduction below present
design values must be accomplished by means other than profile shaping

alone. One alternate means is polymer injection in the boundary layer.

Numerous optimization runs made at $R_V = 5 \times 10^7$ using two search strategies produced a number of low drag shapes. Fine tuning by hand reveals that there is apparently a unique global minimum drag shape. The global minimum has high sensitivity to early transition; hence, sub-optimal solutions without this sensitivity are more desirable from the hydrodynamic design point of view. Alternatively, additional constraints may be imposed on the problem to avoid such undesirable characteristics.

The modified Complex Method used in this study has performed well. It operates in a constrained environment without difficulty. Since it moves on global information, the method can cope with errors in the performance function which do not obliterate global trends. The method is well suited for design problems without critical convergence tolerances. For the drag minimization problem, one may expect to use 10N to 15N minutes of CDC 6500 computer time to obtain a minimum drag body using the recommended 30-station solutions, where N is the number of parameters.

Powell's Method along with the penalty function used in this study can only be used effectively with 99-station (3 minute) solutions since the normal 30-station (1 minute) solutions introduce enough error to confuse this locally moving method. The method's primary use for the present problem is fine tuning; one may expect to use 9N to 12N minutes of CDC 6500 computer time for each cycle of fine tuning using the recommended 99-station solutions, where N is the number of parameters. Normally, fine tuning by this method is not necessary; when it is required, one cycle is adequate.

Several recommendations for future research can be made concerning the drag minimization problem. The two classes of bodies considered in this study are constrained to be well behaved according to previous hydrodynamic experience. The analyses for the various constraint boundaries are complicated and lack generality. It may prove beneficial to develop a more general class of bodies using orthogonal polynomials, for example. Rather than deriving constraint boundaries, it would be simpler to make a direct check of the profile and its derivatives; however, knowledge of the constraint boundaries does provide insight into the nature of the problem.

The one outstanding weakness of the modified Complex Method is its stopping condition. The problem is that a large number of function evaluations are wasted in the process of deciding that the best design is sufficiently near a local minimum. A more sophisticated terminating strategy would be beneficial.

In the area of drag prediction, the major weakness appears to be the modeling of the transition region. The assumption of point transition may be poor at low Reynolds numbers for which there is no abrupt increase in skin friction as predicted by the drag model used in this study. The use of the planar flow Michel-e^9 correlation to predict transition of axisymmetric boundary layers probably introduces some error. Experimental verification of the results of this study is certainly desirable.

As far as hydrodynamic design is concerned, the next logical step is to include the propeller or propulsive jet effects in the drag model. This would change the problem from drag to power minimization. Since the presence of the propeller or propulsive jet will change the flow field, it is expected that the minimum power body shapes will differ from those for minimum drag. As mentioned above, it seems desirable to further constrain the problem to avoid high sensitivity to early transition.

LIST OF REFERENCES

1. Granville, P. S., "Progress in Frictional Drag Reduction, Summer 1968 to Summer 1969," Naval Ship Research and Development Center, Hydromechanics Laboratory Technical Note 143 (August 1969).

2. Carmichael, B. H., "Underwater Vehicle Drag Reduction through Choice of Shape," AIAA Paper #66-657 (June 1966).

3. Gertler, M., "Resistance Experiments on a Systematic Series of Streamlined Bodies of Revolution -- For Application to the Design of High-Speed Submarines," David Taylor Model Basin Report No. C-297 (1950).

4. Cebeci, T., and Mosinskis, G. J., "Calculation of Viscous Drag and Turbulent Boundary-Layer Separation of Two-Dimensional and Axisymmetric Bodies in Incompressible Flows," Douglas Aircraft Company Report MDC-J0973-01 (November 1970).

5. Smith, A. M. O., and Gamberoni, N., "Transition, Pressure Gradient, and Stability Theory," Douglas Aircraft Company Report ES26388 (August 31, 1956).

6 Schlichting, H., Boundary Layer Theory, Sixth Edition, McGraw-Hill Book Company, New York (1968).

7. Cebeci, T., Smith A. M. O., and Wang, L. C., "A Finite-Difference Method for Calculating Compressible Laminar and Turbulent Boundary Layers," Douglas Aircraft Company Report DAC-67131 (March 1969).

8. Sandborn, V. A., "Characteristics of boundary Layers at Separation and Reattachment," Research Memorandum No. 14, Fluid Dynamics and Diffusion Laboratory, Colorado State University (February 1969).

9. VanWagonen, R. G., ., "A Study of Axially-Symmetric Subsonic Base Flow," Ph.D. Thesis, University of Washington (June 1968).

10. Smith, A. M. O., and Pierce, J., "Exact Solution of the Neumann Problem. Calculation of Non-Circulatory Plane and Axially Symmetric Flows about or within Arbitrary Boundaries," Douglas Aircraft Company Report 26988 (April 25, 1958).

11. Faulkner, S., Hess, J. L., and Giesing, J. P., "Comparison of Experimental Pressure Distributions with Those Calculated by the Douglas Neumann Program," Douglas Aircraft Company Report LB31831 (December 1, 1964).

12. Young, A. D., "The Calculation of the Total and Skin Friction Drags of Bodies of Revolution at Zero Incidence," R. and M. No. 1874 (April 1939).

13. Murphy, J. S., "The Separation of Axially Symmetric Turbulent Boundary Layers," Douglas Aircraft Company Report ES17513 (March 1954).

14. Granville, P. S., "Comparison of Existing Methods for Predicting Transition from Laminar to Turbulent Flow on Bodies of Revolution," Naval Ship Research and Development Center, Hydromechanics Laboratory Technical Note 111 (August 1968).

15. Rao, K. N., Narasimha, R., and Narayanan, M. A. B., "The 'Bursting' Phenomenon in a Turbulent Boundary Layer," Journal of Fluid Mechanics, Vol. 48, Part 2, pp. 339 - 352 (1971).

16. Liebeck, R. H., and Ormsbee, A. I., "Optimization of Airfoils for Maximum Lift," AIAA No. 69-739 (July 1969).

17. Marshall, F. J., "Design Problem in Hydrodynamics," Journal of Hydronautics, Vol. 4, No. 4, pp. 136 - 139 (October 1970).

18. Weinstock, R., Calculus of Variations, McGraw-Hill Book Company, Inc., New York (1952).

19. Gelfand, I. M., and Fomin, S. V., Calculus of Variations, translated from the Russian and edited by R. A. Silverman, Prentice-Hall, Inc., Englewood Cliffs, New Jersey (1963).

20. Beveridge, G. S. G., and Schechter, R. S., Optimization: Theory and Practice, McGraw-Hill Book Company, Inc., New York (1970).

21. Rosenbrock, H. H., "An Automatic Method for Finding the Greatest or Least Value of a Function," The Computer Journal, Vol. 3, No. 3, pp. 175 - 184 (October 1960).

22. Box, M. J., "A New Method of Constrained Optimization and a Comparison with Other Methods," The Computer Journal, Vol. 8, No. 1, pp. 42 - 52 (April 1965).

23. Guin, J. A., "Modification of the Complex Method of Constrained Optimization," The Computer Journal, Vol. 10, No. 4, pp. 416 - 417 (February 1968).

24. Hooke, R., and Jeeves, T. A., "Direct Search Solution of Numerical and Statistical Problems," Journal of the ACM, Vol. 8, No. 2, pp. 212 - 229 (April 1961).

25. Powell, M. J. D., "An Efficient Method for Finding the Minimum of a Function of Several Variables without Calculating Derivatives," The Computer Journal, Vol. 7, No. 2, pp. 155 - 162 (July 1964).

26. Wozny, M. J., and Heydt, G. T., "A Directed Random Search," ASME Paper 70-WA/Aut-7 (1970). Also available under the same title as a Ph.D. thesis by Heydt, School of Electrical Engineering, Purdue University, Lafayette, Indiana (August 1970).

27. Masters, C. O., and Drucker, H., "Observations on Direct Search Procedures," correspondence in IEEE Transactions on Systems, Man, and Cybernetics, pp. 182 - 184 (April 1971).

28. Fletcher, R., "Function Minimization without Evaluating Derivatives — A Review," The Computer Journal, Vol. 8, No. 1, pp. 33 - 41 (April 1965).

29. Granville, P. S., "Geometrical Characteristics of Streamlined Shapes," Naval Ship Research and Development Center Report No. 2962 (March 1969).

30. Aird, T. J., system subroutine available on Purdue CDC 6500 computer. Documentation includes Purdue Computing Center Document C4 SECANT. Original publication of the Secant Method given by Wolfe, P., "The Secant Method for Simultaneous Nonlinear Equations," Communications of the ACM, Vol. 2, pp. 12 - 13 (1959).

31. Gray, Sir James, "How Fishes Swim," Scientific American, pp. 48 - 54 (August 1957).

32. Johannessen, C. L., and Harder, J. A., "Sustained Swimming Speeds of Dolphins," Science, Vol. 133, p. 952+ (March 24, 1961).

33. Lang, T. G., and Norris, K. S., "Swimming Speed of a Pacific Bottlenose Porpoise," Science, Vol. 151, pp. 588 - 590 (February 4, 1966).

34. Lang, T. G., and Pryor, K., "Hydrodynamic Performance of Porpoises, stenella attenuata," Science, Vol. 152, pp. 531 - 533 (April 22, 1966).

35. Haldane, J. B. S., "On Being the Right Size," from The World of Mathematics, Vol. 2, pp. 952 - 957, with commentaries and notes by J. R. Newman, Simon and Schuster, New York (1957; essay written about 1930).

APPENDIX A

DERIVATION OF DISPLACEMENT THICKNESS FOR MASS CONSERVATION IN AN EXTERNAL AXISYMMETRIC FLOW

This appendix presents the derivation of the displacement thickness δ^*_{ax} for mass conservation in an external axisymmetric flow. The principal notation is shown in Figure A1. The zero incidence flow with
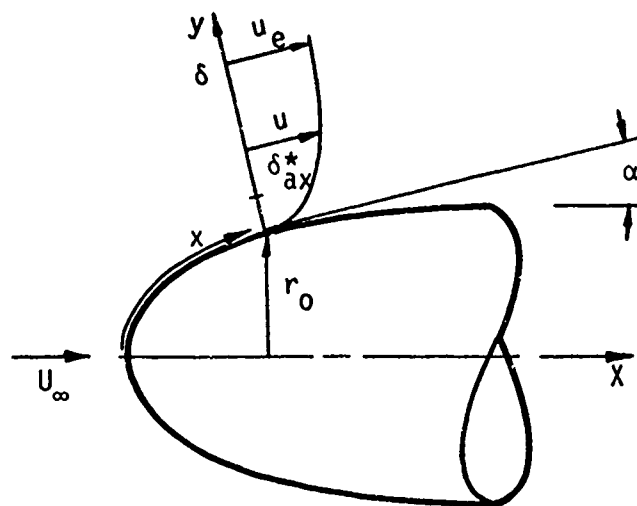
Figure A1. External Axisymmetric Flow Notation.

reference velocity U_∞ is parallel to the centerline X-axis. The boundary layer is specified in terms of the curvilinear x-y coordinate system. At a point in the boundary layer the velocity is $u = u(x, y)$,

which approaches the external value $u_e(x)$ as y approaches the boundary layer thickness δ. The local tangent has angle α; the local wall radius is r_0. It is also convenient to use the relationship $r = r_0 + y \cos \alpha$, where r is the radial coordinate of a point in the flow. The local density $\rho(x, y)$ and external density $\rho_e(x)$ are retained in the derivation to follow.

The displacement thickness concept equates the retarded boundary layer mass flow to a displaced inviscid mass flow of constant local velocity $u_e(x)$. This may be written as

(Viscous Mass Flux) = (Inviscid Mass Flux)

$$\int_0^\infty \rho u \, 2\pi r \, dy = \int_{\delta_{ax}^*}^\infty \rho_e u_e \, 2\pi r \, dy \qquad (A.1)$$

We assume that outside the boundary layer, i.e., for $y \geq \delta$, that $\rho u = \rho_e u_e$ so that equation (A.1) reduces to

$$\int_0^\delta \rho u r \, dy = \int_{\delta_{ax}^*}^\delta \rho_e u_e r \, dy \qquad (A.2)$$

This may be written as

$$\int_0^\delta \rho u r \, dy = \int_0^{\delta_{ax}^*} \rho_e u_e r \, dy + \int_{\delta_{ax}^*}^\delta \rho_e u_e r \, dy - \int_0^{\delta_{ax}^*} \rho_e u_e r \, dy \qquad (A.3)$$

which reduces to

$$\int_0^{\delta_{ax}^*} r \, dy = \int_0^\delta (1 - \frac{\rho u}{\rho_e u_e})r \, dy \tag{A.4}$$

Replacing r by $r_0 + y \cos \alpha$ in the left-hand side of equation (A.4) and dividing through by r_0 gives

$$\int_0^{\delta_{ax}^*} (1 + \frac{\cos \alpha}{r_0}y)dy = \int_0^\delta (1 - \frac{\rho u}{\rho_e u_e})\frac{r}{r_0} \, dy \tag{A.5}$$

for $r_0 \neq 0$. If $y \cos \alpha/r_0 \ll 1$, then we obtain

$$\delta_{ax}^* \simeq \int_0^\delta \frac{r}{r_0} (1 - \frac{\rho u}{\rho_e u_e}) \, dy \tag{A.6}$$

which is the definition of δ^* as given by equation (2.17) where $\rho = \rho_e$ is constant.

When $y \cos \alpha/r_0$ cannot be neglected, then integration of the left hand side of equation (A.5) gives

$$\delta_{ax}^* + \frac{\cos \alpha}{2r_0}(\delta_{ax}^*)^2 = \delta^* \tag{A.7}$$

where δ^*, as defined by equation (2.17), has replaced the integral on the right-hand side of equation (A.5). Equation (A.7) is quadratic in δ_{ax}^*; applying the quadratic formula gives

$$\delta_{ax}^* = \frac{r_0}{\cos \alpha} \left[-1 + (1 + \frac{2 \cos \alpha}{r_0} \delta^*)^{\frac{1}{2}} \right] \tag{A.8}$$

which is the desired result.

APPENDIX B

DERIVATION OF YOUNG'S FORMULA FOR DRAG OF
AXISYMMETRIC BODIES AT ZERO INCIDENCE

Young's formula is based on the boundary layer momentum integral equation. If the pressure gradient across the boundary layer and wake is negligible, the momentum integral equation for axisymmetric bodies may be written

$$\frac{\partial \chi}{\partial x} + \frac{u_e'}{u_e} (H + 2)\chi = \frac{\tau_w}{\rho u_e^2} 2\pi r \qquad (B.1)$$

where x is the streamwise coordinate along the body surface, u_e is the velocity at the edge of the boundary layer, u_e' is du_e/dx, τ_w is the shear stress at the wall, ρ is the fluid density, r is the radial coordinate measured from the body axis and $r = r_0 + y \cos \alpha$, where r_0 is the wall radius, α is the angle between the surface tangent and the body axis in a meridional plane, y is the coordinate normal to the wall, χ is the momentum area, and H is the shape factor.

For the non-separating wake, the momentum integral equation is assumed to apply and the skin friction τ_w is zero so that equation (B.1) may be written

$$\frac{d\chi}{dx} + \frac{u_e'}{u_e} (H + 2)\chi = 0 \qquad (B.2)$$

where for the wake region x is the streamwise coordinate measured from the tail along the axis of symmetry, $\partial \chi/\partial x$ is replaced by $d\chi/dx$, and the radial coordinate r reduces to y.

The momentum area of the wake is defined as

$$\chi \;=\; 2\pi \int_{0}^{\infty} \frac{u}{u_e} \left(1 - \frac{u}{u_e}\right) y \; dy \tag{B.3}$$

and the displacement area of the wake is defined as

$$\Lambda \;=\; 2\pi \int_{0}^{\infty} \left(1 - \frac{u}{u_e}\right) y \; dy \tag{B.4}$$

so that the shape factor is defined as

$$H \;=\; \Lambda/\chi \tag{B.5}$$

Rearranging equation (B.2) and using the fact that

$$d(\ell n \; u_e) \;=\; \frac{du_e}{u_e} \tag{B.6}$$

so that

$$\frac{d}{dx}\left(\ell n \; \frac{u_e}{U_\infty}\right) \;=\; \frac{d}{dx}\left(\frac{u_e}{U_\infty}\right) \frac{1}{u_e/U_\infty} \tag{B.7}$$

we may write

$$\frac{1}{\chi}\frac{d\chi}{dx} \;=\; -\,(H + 2)\frac{d}{dx} \, \ell n \, \frac{u_e}{U_\infty} \tag{B.8}$$

or

$$d(\ln \chi) = - (H + 2) d(\ln \frac{u_e}{U_\infty}) \qquad (B.9)$$

Integrating from the tail downstream to infinity we obtain

$$\int_{()_1}^{()_\infty} d \ln \chi = - \int_{()_1}^{()_\infty} (H + 2) d(\ln \frac{u_e}{U_\infty}) \qquad (B.10)$$

$$\ln \chi_\infty - \ln \chi_1 = - (H + 2) \ln \frac{u_e}{U_\infty} \Big]_{()_1}^{()_\infty} + \int_{H_1}^{1} \ln \frac{u_e}{U_\infty} dH \qquad (B.11)$$

where subscripts $()_\infty$ and $()_1$ denote quantities at infinity downstream and at the tail, respectively, and we have used integration by parts on the right-hand side of equation (B.10). The value of H at infinity is unity [12]. Since $\frac{u_e}{U_\infty}\Big]_\infty = 1$, we have that

$$\ln \chi_\infty = \ln \chi_1 + \ln(\frac{u_e}{U_\infty})_1^{(H_1+2)} + \int_{H_1}^{1} \ln \frac{u_e}{U_\infty} dH \qquad (B.12)$$

which can be written

$$\chi_\infty = \chi_1 (\frac{u_e}{U_\infty})_1^{(H_1+2)} \exp \left[\int_{H_1}^{1} \ln \frac{u_e}{U_\infty} dH \right] \qquad (B.13)$$

The exponential term may be written

$$\exp\left[\int_{H_1}^{1} \ln\frac{u_e}{U_\infty} \, dH \right] = \exp\left[\int_{1}^{H_1} \ln\frac{U_\infty}{u_e} \, dH \right] \qquad (B.14)$$

At this point Young assumes that $\ln\dfrac{u_e}{U_\infty}$ varies linearly with H so that the integral in equation (B.14) is approximately the area of a triangle. This gives

$$\int_{1}^{H_1} \ln\left(\frac{U_\infty}{u_e} \right) \, dH \simeq \frac{H_1 - 1}{2} \ln\left(\frac{U_\infty}{u_e} \right)_1 \qquad (B.15)$$

or

$$\exp\left[\int_{1}^{H_1} \ln\frac{U_\infty}{u_e} \, dH \right] \simeq \left(\frac{U_\infty}{u_e} \right)_1^{\left(\frac{H_1-1}{2}\right)} \qquad (B.16)$$

Using equation (B.16) in equation (B.13) and replacing $\simeq$ with $=$ gives

$$\chi_\infty = \chi_1 \left(\frac{u_e}{U_\infty} \right)_1^{\left(\frac{H_1+5}{2}\right)} \qquad (B.17)$$

Equation (B.17) relates the momentum area of the wake at infinity χ_∞ to the momentum area of the wake at the tail χ_1 and other trailing edge

parameters. The drag coefficient is computed considering the momentum flux across a closed control volume surface. The result is that

$$C_D = \frac{2}{V^{\frac{2}{3}}} \chi_\infty = \frac{2}{V^{\frac{2}{3}}} \chi_1 \left(\frac{u_e}{U_\infty} \right)_1^{\left(\frac{H_1+5}{2}\right)} \tag{B.18}$$

Since $\chi_1 = 2\pi r_0 \theta$, where θ is the momentum thickness defined as

$$\theta = \int_0^\infty \frac{r}{r_0} \frac{u}{u_e} \left(1 - \frac{u}{u_e} \right) dy \tag{B.19}$$

then we may write finally that

$$C_D = \frac{4\pi}{V^{\frac{2}{3}}} r_0 \, \theta \left(\frac{u_e}{U_\infty} \right)_1^{\left(\frac{H_1+5}{2}\right)} \tag{B.20}$$

which is identical to equation (2.15). We have tacitly assumed here also that the wake momentum area at the tail is equal to that of the boundary layer there. This seems reasonable since the momentum defect of viscous flows must change in a continuous manner.

APPENDIX C

DETAILED STRATEGY OF MODIFIED COMPLEX METHOD

The word flow chart given below gives the detailed strategy of the Complex Method [22] as used in the present study. The strategy includes modifications due to Guin [23] to cope with nonconvex boundaries as well as the generation of new search directions when the primary direction fails. The starting procedure is a modification of Box's original method.

A. Input

    1. Number of independent parameters N.

    2. Number of vertices in complex figure K.

    3. Maximum number or performance function evaluations IPMAX.

    4. Tolerances ϵ_1, ϵ_2, ϵ_3.

    5. Expansion factor α.

    6. Contraction factor β.

    7. Lower constant boundaries a_{L_i}, $i = 1, \ldots, N$, used during initial complex generation.

    8. Upper constant boundaries a_{U_i}, $i = 1, \ldots, N$, used during initial complex generation.

B. Initial Complex Generation

    1. Set j = 1.

    2. Does j exceed K?

       a. Yes: Go to B.4.

       b. No: Randomly generate jth vertex using next N elements of random number sequence indicated by (rn_i), $i = 1, \ldots, N$.

$$a_i]_j = (rn_i)(a_{U_j} - a_{L_j}), \quad 0 \leq rn_i \leq 1$$
$$i = 1, \ldots, N$$

3. Is random vertex $\underline{a}_j$ feasible?

    a. Yes: Evaluate performance function PF_j for vertex $\underline{a}_j$.
            Set $j = j + 1$.
            Go to B.2.

    b. No: Has random generation of vertex $\underline{a}_j$ failed more than 1000 times?

        1) Yes: Abort program.
               CALL EXIT.

        2) No: Try another random generation of vertex $\underline{a}_j$.
              Go to B.2.b.

4. Set $\underline{a}_{best}$ = best vertex of initial complex.
    Set PF_{best} = PF value of $\underline{a}_{best}$.
    <u>Go to C.4.</u>

C. Search Procedure

1. Is newest vertex better than $\underline{a}_{best}$?

    a. Yes: An improvement has occurred.
            Increment improvement counter IMPRV = IMPRV + 1
            Set $\underline{a}_{best}$ = new vertex.
            Set PF_{best} = PF value for new $\underline{a}_{best}$.
            Go to C.2.

    b. No: Continue.

2. Check stopping condition: Are five best PF values within relative ϵ_3-neighborhood of PF_{best}?

    a. Yes: Tentative convergence. Are corresponding five best vertices within relative ϵ_3-neighborhood of $\underline{a}_{best}$?

        1) Yes: Convergence achieved. Go to C.11.

        2) No: Try one more vertex rejection, i.e., if the previous vertex rejection originated from this point in program, assume convergence and go to C.11. Otherwise, go to C.3.

    b. No: No convergence. Continue.

3. Will next performance function evaluation exceed maximum number IPMAX allowed?

    a. Yes: Output results obtained so far.
            CALL EXIT.

   b. No: Continue.

4. Reject worst vertex. Rejected vertex is $\underline{a}_r$.

5. Compute centroid $\underline{cgr}$ of remaining vertices.

$$cgr_i = \frac{1}{(K-1)} \sum_{\substack{j=1 \\ j \neq r}}^{K} a_i]_j \, , \quad i = 1, \ldots, N$$

6. Is $\underline{cgr}$ in feasible region?

   a. Yes: Set NCGVIO = 0
            Go to C.7.

   b. No: Set NCGVIO = 1

7. Generate trial vertex $\underline{a}_t$.

   $$\underline{a}_t = \underline{cgr} + \alpha(\underline{cgr} - \underline{a}_r)$$

8. Is trial vertex $\underline{a}_t$ in feasible region?

   a. Yes: Evaluate trial vertex performance function PF_t.
            Go to C.10.

   b. No: Does NCGVIO = 1?

      1) Yes: Go to C.9.

      2) No: Is trial vertex $\underline{a}_t$ within relative ε_2-neighborhood of $\underline{cgr}$?

         a) Yes: Set $\underline{a}_t = \underline{cgr}$ which is feasible.
                   Evaluate PF_t. Go to C.10.

         b) No: Move trial vertex $\underline{a}_t$ amount β toward $\underline{cgr}$. New $\underline{a}_t = \beta(\text{old } \underline{a}_t + \underline{cgr})$.
                   Go to C.8.

9. Both centroid $\underline{cgr}$ and trial vertex $\underline{a}_t$ are not feasible. Reject entire complex figure. Have more than 10 complex rejections occurred?

   a. Yes: Abort search.
            CALL EXIT.

   b. No: Reset lower bounds a_{L_i} and upper bounds a_{U_i}, $i = 1$, ..., N, to coincide with unfeasible centroid $\underline{cgr}$ and best previous vertex $\underline{a}_{best}$. Swap components if necessary to insure that $a_{L_i} \leq a_{U_i}$, $i = 1, \ldots, N$. Go to B.1.

10. Is trial vertex performance function PF_t better than second worst PF value?

a. Yes: Replace worst vertex with vertex $\underline{a}_t$.
Go to C.1.

b. No: Is trial vertex $\underline{a}_t$ within relative ε_2-neighborhood of centroid $\underline{cgr}$?

1) Yes: Try a new search direction. Reject the next worst vertex and retain previously rejected vertex. Rejected vertex is $\underline{a}_r$. Have all K vertices been successively rejected?

a) Yes: Abort search.
CALL EXIT.

b) No: Go to C.5.

2) No: Move trial vertex $\underline{a}_t$ amount β toward centroid $\underline{cgr}$. New $\underline{a}_t = \beta(\text{old } \underline{a}_t + \underline{cgr})$. Go to C.8.

11. Output optimum parameters $\underline{a}^*$.

$$\underline{a}^* = \underline{a}_{best}$$

12. END

APPENDIX D

DETAILED STRATEGY OF POWELL'S METHOD OF CONJUGATE DIRECTIONS

The word flow chart given below presents the strategy for Powell's Method of Conjugate Directions [25]. The only modification from Powell's original procedure is the procedure for computing the new step size STEP used in the linear search routine; see item B.15 in the outline below. Following Powell's method is a word flow chart for the linear search strategy involving a parabolic interpolation scheme.

D.1 Strategy for Powell's Method

A. Input

1. Number of independent parameters N.
2. Feasible initial guess vector $\underline{a}_0 = (a_{0_1}, a_{0_2}, \ldots, a_{0N})$.
3. Set of N linearly independent normalized search direction vectors $(\underline{\xi}_1, \underline{\xi}_2, \ldots, \underline{\xi}_N)$.
4. Lower and upper scaling vectors, $\underline{a}_L$ and $\underline{a}_U$, respectively, where $\underline{a}_L = (a_{L_1}, a_{L_2}, \ldots, a_{L_N})$ and $\underline{a}_U = (a_{U_1}, a_{U_2}, \ldots, a_{U_N})$.
5. Maximum number of search cycles ICYMAX.
6. Initial scaled step size STEP used in linear search routine.
7. Convergence tolerance ε_3.

B. Search Procedure

1. Initialization.
   a. Scale initial guess vector to $\underline{X}_0$, where $X_{0_i} = (a_{0_i} - a_{L_i}) / (a_{U_i} - a_{L_i})$, $i = 1, \ldots, N$.

    b. Evaluate performance function PF_0 of initial guess.

2. Start search cycle.

    a. Set maximum PF change $\Delta_m = 0$.

    b. Set direction number for maximum PF change $i_m = 1$.

    c. Set direction index $j = 1$.

3. CALL COGGIN (linear search routine): from base point $\underline{X}_{j-1}$

   perform linear minimization along direction vector $\underline{\xi}_j$. Find
   the minimum point $\underline{X}_j$ and its performance function value PF_j.

4. Test for maximum PF change. Is $|PF_j - PF_{j-1}|$ greater than
   Δ_m ?

    a. Yes: Set $\Delta_m = |PF_j - PF_{j-1}|$.
             Set $i_m = j$. Go to B.5.

    b. No: Go to B.5.

5. Increment direction index $j = j + 1$. Is $j \leq N$?

    a. Yes: Continue cycle, go to B.3.

    b. No: Cycle is complete.
            Go to B.6.

6. Set $\underline{X}_{best} = \underline{X}_N$ and $PF_{best} = PF_N$.

7. Compute new direction vector $\underline{\mu} = (\underline{X}_N - \underline{X}_0)$, that is, $\mu_i = X_{N_i} - X_{0_i}$, $i = 1, \ldots, N$.

8. Compute trial point $\underline{y}_t = \underline{X}_N + \underline{\mu}$, that is, $y_{t_i} = 2X_{N_i} - X_{0_i}$,

   $i = 1, \ldots, N$. Is $|\underline{y}_t - \underline{X}_0|$ less than $(.001)(\varepsilon_3)$?

    a. Yes: Convergence likely. Go to B.14.

    b. No: Compute $PF_t = PF(\underline{y}_t)$. Go to B.9.

9. Perform Powell's first inequality check on new direction. Is
   $(PF_t - PF_0) \geq 0$?

    a. Yes: New direction is not promising.
            Go to B.13.

    b. No: Go to B.10.

10. Perform Powell's second inequality check on new direction. Is
    $(PF_0 - 2PF_N + PF_t)(PF_0 - PF_N - \Delta_m) \geq \frac{1}{2}\Delta_m(PF_0 - PF_t)$?

    a. Yes: New direction is not promising.
            Go to B.13.

    b. No: Go to B.11.

11. New direction is promising. Remove direction vector of maximum PF change, $\underline{\xi}_{i_m}$. Put new direction vector in $\underline{\xi}_N$:

    a. For $i = 1, \ldots, i_m - 1$: new $\underline{\xi}_i$ = old $\underline{\xi}_i$.

    b. For $i = i_m - 1, \ldots, N - 1$: new $\underline{\xi}_i$ = old $\underline{\xi}_{i+1}$.

    c. For $i = N$: new $\underline{\xi}_N = \underline{\mu}/|\underline{\mu}|$.

12. CALL COGGIN (linear search routine): from base point $\underline{X}_N$ perform linear minimization along new direction vector $\underline{\xi}_N$. Find new minimum point $\underline{X}_{best}$ and its performance function value PF_{best}. Go to B.14.

13. New direction is not promising. Retain old search directions:

    a. For $i = 1, \ldots, N$: new $\underline{\xi}_i$ = old $\underline{\xi}_i$.

    b. Go to B.14.

14. Test for convergence.

    a. Is $\left| \dfrac{PF_0 - PF_{best}}{PF_0} \right| \leq \epsilon_3$?

        1) Yes: Go to B.14.b.

        2) No: Go to B.15.

    b. Is $\left| \dfrac{X_{0i} - X_{best\ i}}{X_{0i}} \right| \leq \epsilon_3$?

        $i = 1, \ldots, N$

        1) Yes: Convergence achieved.
            Go to B.17.

        2) No: Go to B.15.

15. No convergence yet. Compute new step size STEP:

    a. $\Delta X = \left| \underline{X}_{best} - \underline{X}_0 \right|$.

    b. $\Delta PF = \left| PF_{best} - PF_0 \right|$.

    c. $STEP = \sqrt{\Delta PF}$.

    d. Is $STEP < (0.1)(\Delta X)$?

        1) Yes: Set $STEP = (0.1)(\Delta X)$.
            Go to B.15.e.

        2) No: Go to B.15.e.

    e. Is STEP > (0.5)(old STEP)?

        1) Yes: Set STEP = (0.5)(old STEP).
                 Go to B.15.f.

        2) No: Go to B.15.f.

    f. Set $\underline{X}_0 = \underline{X}_{best}$, $PF_0 = PF_{best}$.

16. Will next cycle exceed maximum number ICYMAX of cycles allowed?

    a. Yes: Output results obtained so far.
             CALL EXIT.

    b. No: Go to B.2.

17. Convergence achieved.

    a. Scale optimum $\underline{X}^*$ back to $\underline{a}^*$: $a_i^* = a_{L_i} + X_i^* (a_{U_i} - a_{L_i})$,
        $i = 1, \ldots, N$.

    b. CALL EXIT.

18. END.

D 2 Strategy for Linear Search Routine

    The word flow chart below gives the detailed strategy for the parabolic interpolation scheme used for the linear search in the present study. The method always brackets the minimum along the line of search before applying the parabolic interpolation.

A. Input from Calling Program POWELL

1. Current base point is $\underline{X}$ with performance function value FX.
2. Current step vector is $\underline{S}$ = STEP $\underline{\xi}$, where $\underline{\xi}$ is the current normalized search direction and $\underline{S}$ = $(S_1, S_2, \ldots, S_N)$. S_i = $(STEP)(\xi_i)$, $i = 1, \ldots, N$.

B. Linear Search Procedure.

1. Initialization.
    a. Set step multiplier D = 1.
    b. Set distance DA = 0 for point A.
    c. Set distance DB = 0 for point B.

     d.   Set distance DC = 0 for point C.

     e.   Set performance function FA = FX for point A.

     f.   Set performance function FB = 0 for point B.

     g.   Set performance function FC = 0 for point C.

     h.   Set step counter K = -2.

     i.   Set linear search convergence tolerance TOL = $3\epsilon_3$.

2. Start linear search.

     a.   Compute point $\underline{y} = \underline{X} + D\underline{S}$, where $y_i = X_i + D\,S_i$, i = 1, ..., N.

     b.   Compute performance function F for $\underline{y}$.

     c.   Increment step counter K = K + 1.

3. Is $F \geq FA$?

     a.   Yes: A bracket point has been found.
               Go to B.4.

     b.   No: Performance function is still decreasing.

           1) Reset points A, B, and C

              DC = DB   FC = FB

              DB = DA   FB = FA

              DA = D   FA = F

           2) Compute new step
              For D > 0: new D = 2(old D) + 1.
              For D < 0: new D = 2(old D) - 1.

           3) Go to B.2.

4. A bracket point has been found. Is $K \geq 0$?

     a.   Yes: Both bracket points have been found.
               Set up points A, B, and C so that the minimum point
               B is bracketed by the points A and C:

              DC = DB   FC = FB

              DB = DA   FB = FA

              DA = D   FA = F

              Go to B.5.

     b.   No: First bracket point has been found after first step
               along line of search. Reverse direction and continue.

           1) Set point B

              FB = F   DB = D

           2) Change sign of step multiplier

              new D = - old D

           3) Go to B.2.

5. Proceed with parabolic interpolation.

   a. Compute location D of minimum on parabolic arc.

   b. Is point D between DA and DC?

     1) Yes: Go to B.5.c.

     2) No: Parabolic interpolation has failed. Use best point B as local minimum. Go to B.6.

   c. Perform parameter convergence check:

     Is $|D - DA| / |DA - DC| \leq$ TOL?

     1) Yes: Convergence achieved. Use point B as local minimum. Go to B.6.

     2) No: Go to B.5.d.

   d. Perform function convergence check. Compute point $\underline{y} = \underline{X} + D\,\underline{S}$ and its performance function value F. Is

     $|FB - F| / |FB_1| \leq$ TOL?

     1) Yes: Convergence achieved. Use smaller of FB or F as local optimum. Go to B.6.

     2) No: No convergence yet. Reset points so that minimum point B is bracketed by points A and C. Go to B.5.

6. Convergence to local minimum along line of search has been achieved. Compute approximate second derivative associated with present search direction, $\partial^2 PF / \partial \underline{\xi}^2$.

7. RETURN TO POWELL.

APPENDIX E

DERIVATION OF PARAMETRIC BODY PROFILES

This appendix presents the derivations for the parametrically defined body profiles considered in the present study. The pertinent constraint boundaries are also derived. The procedures follow those reported by Granville (1969) [29] in which the body is divided into sections at convenient axial locations, e.g., maximum diameter point.

E.1 Rounded-Nose Forebody Section [29]

The rounded-nose forebody and its dimensional parameters are shown in Figure E1. The maximum diameter D occurs at the axial location X_m; the curvature at this point is K_1. The nose radius of curvature is R_n.
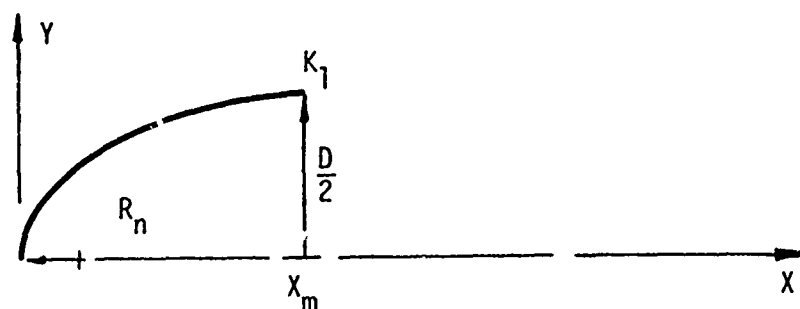
Figure E1. Rounded-Nose Forebody Section.

The boundary conditions for this profile $Y(X)$ are listed below where primes on $Y(X)$ denote differentiation with respect to X:

1. $Y(0) = 0$ (E.1a)

2. $Y'(0) = \infty$ or $dX/dY]_{X=0} = 0$ (E.1b)

3. $1/(d^2X/dY^2)]_{X=0} = R_n$ (E.1c)

4. $Y(X_m) = D/2$ (E.1d)

5. $Y'(X_m) = 0$ (E.1e)

6. $Y''(X_m) = K_1$ (E.1f)

where R_n, D, K_1, and X_m may all vary.

It is possible to reduce $Y(X)$ to a nondimensional profile with only two variable boundary conditions. We define the nondimensional profile to be

$$x = X/X_m$$ (E.2a)

$$y = 2Y/D$$ (E.2b)

so that the boundary conditions given by equations (E.1) become

1. $y(0) = 0$ (E.3a)

2. $dx/dy]_{x=0} = 0$ (E.3b)

3. $1/(d^2x/dy^2)]_{x=0} = 4X_m R_n/D^2 = r_n$ (E.3c)

4. $y(1) = 1$ (E.3d)

5. $y'(1) = 0$ (E.3e)

6. $y''(1) = 2X_m^2 K_1/D = -k_1$ (E.3f)

where primes on $y(x)$ denote differentiation with respect to x. The variable boundary conditions are r_n and k_1; two free parameters make it possible to conveniently plot constraint boundaries for the forebody.

The intent here is to derive the simplest polynomial expressions which satisfy the boundary conditions given by equations (E.3). Furthermore, we shall attempt to make the expressions linear in the free parameters r_n and k_1. For this purpose we define the "quadratic" polynomial

$$f(x) = y^2(x) = \sum_{i=0}^{n} b_i x^i \qquad (E.4)$$

where the b_i, $i = 0, ..., n$, are to be determined using the boundary conditions given by equations (E.3). Differentiating equation (E.4) with respect to x gives

$$f' = \frac{d}{dx} y^2 = 2yy' = \sum_{i=1}^{n} (i) b_i x^{i-1} \qquad (E.5)$$

$$f'' = \frac{d^2}{dx^2} y^2 = 2yy'' + 2y'^2 = \sum_{i=2}^{n} (i)(i-1) b_i x^{i-2} \qquad (E.6)$$

$$f''' = \frac{d^3}{dx^3} y^2 = 2yy''' + 6y''y' = \sum_{i=3}^{n} (i)(i-1)(i-2) b_i x^{i-3} \qquad (E.7)$$

where primes on $f(x)$ denote differentiation with respect to x. Equation (E.5) may be written as

$$2y = \left[\sum_{i=1}^{n} (i)\, b_i\, x^{i-1} \right] \frac{dx}{dy} \tag{E.8}$$

and differentiating equation (E.8) with respect to y gives

$$2 = \left[\sum_{i=2}^{n} (i)(i-1)\, b_i\, x^{i-2} \right] \left(\frac{dx}{dy}\right)^2 + \left[\sum_{i=1}^{n} (i)\, b_i\, x^{i-1} \right] \frac{d^2x}{dy^2} \tag{E.9}$$

For the case $x = 0$, equations (E.4), (E.8), and (E.9) reduce respectively to

$$y(0) = 0 = b_0 \tag{E.10}$$

$$2y(0) = 0 = b_1\, [dx/dy]_{x=0} \tag{E.11}$$

and

$$2 = 2b_2\, [dx/dy]^2_{x=0} + b_1\, [d^2x/dy^2]_{x=0} \tag{E.12}$$

where equation (E.10) has been inserted into equation (E.11). Equation (E.11) implies that b_1 or $[dx/dy]_{x=0}$ or both equal zero. If b_1 equals zero, then boundary condition (E.3c) cannot be satisfied by equation (E.12). Hence $b_1 \neq 0$ and boundary condition (E.3b) is automatically satisfied when $y(0) = 0$. This is the motivation for selecting the "quadratic" polynomial, equation (E.4), at the outset. From equations (E.10), (E.11), and (E.12) we obtain immediately that

$$b_1 = 2r_n \tag{E.13}$$

Using equations (E.10) and (E.13), the boundary conditions (E.3d, e, f) give

$$2r_n + \sum_{i=2}^{n} b_i = 1 \tag{E.14a}$$

$$2r_n + \sum_{i=2}^{n} (i)b_i = 0 \tag{E.14b}$$

$$\sum_{i=2}^{n} (i)(i-1)b_i = -2k_1 \tag{E.14c}$$

Setting $\cdot\cdot = 4$ yields a unique solution for equations (E.14).

Rather than solving for the b_i, $i = 2, 3, 4$, by direct elimination, we follow Granville [29] and postulate the existence of a function $y^2(x)$ which is linear in r_n and k_1. This is justified since y^2 is linear in the b_i, $i = 2, 3, 4$, which are linear in r_n and k_1. Thus we write

$$y^2(x) = r_n F_1(x) + k_1 F_2(x) + G(x) \tag{E.15}$$

where $F_1(x)$, $F_2(x)$, and $G(x)$ are polynomials of degree $n = 4$, and r_n and k_1 are independent and arbitrary for the moment. The six boundary conditions (E.3) imply the following five boundary conditions for $F_1(x)$, $F_2(x)$, and $G(x)$ for arbitrary values of r_n and k_1:

1. $y(0) = 0$ implies that $F_1(0) = F_2(0) = G(0) = 0$

2. $y(1) = 1$ implies that $F_1(1) = F_2(1) = 0$ and $G(1) = 1$

3. $dx/dy]_{x=0} = 0$ implies that

$$2y(0) \, y'(0) = b_1 = 2r_n = r_n F_1'(0) + k_1 F_2'(0) + G'(0)$$

so that $F_1'(0) = 2$ and $F_2'(0) = G'(0) = 0$

4. $y'(1) = 0$ implies that $F_1'(1) = F_2'(1) = G'(1) = 0$

5. $y''(1) = -k_1$ implies that

$$-2k_1 = r_n F_1''(L) + k_1 F_2''(1) + G''(1) \text{ so that}$$

$$F_1''(1) = G''(1) = 0 \text{ and } F_2''(1) = -2$$

Knowing the polynomial degree and the boundary conditions, one can write down the functions $F_1(x)$, $F_2(x)$, and $G(x)$ almost by inspection. For $F_1(x)$ we have that

$$\begin{aligned} F_1(0) &= 0 & F_1(1) &= 0 \\ F_1(0) &= 2 & F_1'(1) &= 0 \\ & & F_1''(1) &= 0 \end{aligned}$$

so that we may write immediately that

$$F_1(x) = c_1 \, x(x-1)^3$$

to satisfy the homogeneous boundary conditions. Applying the final condition $F_1'(0) = 2$ gives

$$F_1(x) = -2x(x-1)^3 \tag{E.16}$$

. ilarly we may write

$$F_2(x) = -x^2(x-1)^2 \tag{E.17}$$

For $G(x)$ we have that

$$G(0) = 0 \qquad G(1) = 1$$
$$G'(0) = 0 \qquad G'(1) = 0$$
$$G''(1) = 0$$

so we may write

$$\frac{d}{dx} G(x) = c_1 x(x-1)^2$$

and integrating gives

$$G(x) = c_1 (\tfrac{1}{4} x^4 - \tfrac{2}{3} x^3 + \tfrac{1}{2} x^2) + c_2$$

For $G(0) = 0$ we have $c_2 = 0$ and for $G(1) = 1$ we obtain finally that

$$G(x) = x^2 (3x^2 - 8x + 6) \tag{E.18}$$

We now have completely defined $y^2(x)$ by equations (E.15), (E.16), (E.17), and (E.18) which satisfy the boundary conditions (E.3). Inserting these results into equation (E.2b), and using the fact that $f_r = L/D$, we obtain the forebody profile equations (4.3) and (4.4) in Chapter 4.

Constraint Boundaries for r_n and k_1. From physical considerations we require a non-negative radius of curvature R_n at the nose and non-positive curvature K_1 at the maximum diameter section. We have defined r_n and k_1 so that $r_n \geq 0$ and $k_1 \geq 0$ satisfy these physical requirements.

Mainly because of previous hydrodynamic experience, an additional requirement is introduced, namely, that of no inflection point on the forebody [29]. The limiting case occurs when the second derivative touches zero but does not change sign and is expressed as

$$d^2 Y(X)/dX^2 = 0 \tag{E.19a}$$

$$d^3Y(X)/dX^3 = 0 \qquad\qquad (E.19b)$$

for $0 \leq X \leq X_m$. If a solution exists for equations (E.19), it represents the r_n versus k_1 curve for which a limiting inflection point occurs somewhere on $0 \leq X \leq X_m$.

Using equations (E.2), (E.5), (E.6), (E.7), and (E.15), equations (E.19) reduce to

$$2ff'' - (f')^2 = 0 \qquad\qquad (E.20a)$$

$$f''' = 0 \qquad\qquad (E.20b)$$

The procedure is to fix the location x on $0 \leq x \leq 1$ where the limiting inflection point occurs and to solve equations (E.20) for the corresponding values of r_n and k_1. In this sense r_n and k_1 are related through the parameter x. The Secant Method [30] is used to obtain the solution which is given in Table E1 and plotted in Figure 20 in Chapter 4.

E.2 Pointed Aftbody Section [29]

The pointed aftbody and its dimensional parameters are shown in Figure E2. The maximum diameter D occurs at the axial location X_m;
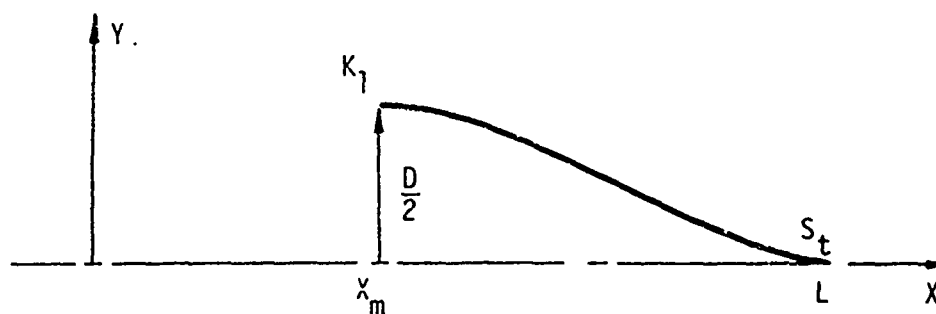
Figure E2. Pointed Aftbody Section.

Table E1. Solution for Limiting Inflection on Forebody.

x	k_1	r_n	x	k_1	r_n
.000	4.0000	.0000	.520	3.7301	1.1187
.020	4.0398	.0005	.540	3.5616	1.2439
.040	4.0794	.0024	.560	3.3711	1.3743
.060	4.1184	.0057	.580	3.1590	1.5080
.080	4.1566	.0105	.600	2.9269	1.6423
.100	4.1940	.0172	.620	2.6774	1.7742
.120	4.2300	.0258	.640	2.4146	1.9002
.140	4.2646	.0366	.660	2.1436	2.0166
.160	4.2972	.0499	.680	1.8710	2.1198
.180	4.3276	.0659	.700	1.6034	2.2069
.200	4.3552	.0849	.720	1.3479	2.2756
.220	4.3796	.1072	.740	1.1104	2.3251
.240	4.4000	.1333	.760	.8957	2.3554
.260	4.4160	.1634	.780	.7068	2.3681
.280	4.4266	.1980	.800	.5448	2.3654
.300	4.4311	.2375	.820	.4094	2.3498
.320	4.4285	.2823	.840	.2988	2.3243
.340	4.4178	.3331	.860	.2108	2.2913
.360	4.3977	.3901	.880	.1424	2.2533
.380	4.3670	.4539	.900	.0909	2.2121
.400	4.3243	.5250	.920	.0534	2.1692
.420	4.2681	.6038	.940	.0276	2.1258
.440	4.1968	.6906	.960	.0112	2.0828
.460	4.1088	.7855	.980	.0026	2.0407
.480	4.0027	.8887	1.000	.0000	2.0000
.500	3.8768	1.0000			

the curvature at this point is K_1. The finite slope at the tail is S_t. The overall body length is L. The boundary conditions for this profile are listed below where primes on $Y(X)$ denote differentiation with respect to X:

1. $Y(X_m) = D/2$ (E.21a)

2. $Y'(X_m) = 0$ (E.21b)

3. $Y''(X_m) = K_1$ (E.21c)

4. $Y(L) = 0$ (E.21d)

5. $Y'(L) = S_t$ (E.21e)

where D, K_1, S_t, X_m, and L may all vary.

It is possible to reduce $Y(X)$ to a nondimensional profile with only two variable boundary conditions. We define the nondimensional profile to be

$$x = (L-X)/(L-X_m) \qquad\qquad\text{(E.22a)}$$

$$y = 2Y/D \qquad\qquad\qquad\text{(E.22b)}$$

so that the boundary conditions given by equations (E.21) become

1. $y(0) = 0$ (E.23a)

2. $y'(0) = -2(L-X_m)S_t/D = s_t$ (E.23b)

3. $y(1) = 1$ (E.23c)

4. $y'(1) = 0$ (E.23d)

5. $y''(1) = 2(L - X_m)^2 K_1/D = -k_{1a}$ (E.23e)

where primes on $y(x)$ denote differentiation with respect to x. From equations (E.3f) and (E.23e) it is apparent that

$$k_{1_a} = k_1[(L-X_m)/X_m]^2 = k_1[(1-x_m)/x_m]^2 \qquad (E.24)$$

where $x_m = X_m/L$. The variable boundary conditions are s_t and k_{1_a}; two free parameters make it possible to conveniently plot constraint boundaries for the pointed aftbody.

We follow the same procedure used in Section E.1 for the forebody so that equations (E.4), (E.5), (E.6), and (E.7) apply. For the case $x = 0$, equations (E.4) and (E.5) reduce to

$$y(0) = 0 = b_0 \qquad (E.25)$$

$$2y(0) \, y'(0) = b_1 \qquad (E.26)$$

In order to satisfy the finite slope requirement when using the "quadratic" polynomial, equation (E.4), then

$$b_1 = 0 \qquad (E.27)$$

so that $y'(0)$ is indeterminant in equation (E.26). Setting $b_1 = 0$ and dividing through by $2y(x)$ in equation (E.5), we may apply L'Hopital's Rule in the limit as x approaches zero so that

$$\lim_{x \to 0} y'(x) = \lim_{x \to 0} \frac{\sum_{i=2}^{n} (i)(i-1)b_i \, x^{i-2}}{2y'(x)} = s_t$$

$$s_t = \frac{2b_2}{2s_t}$$

$$b_2 = s_t^2 \qquad (E.28)$$

Using equations (E.25), (E.27), and (E.28), the boundary conditions (E.23c, d, e) give

$$s_t^2 + \sum_{i=3}^{n} b_i = 1 \tag{E.29a}$$

$$2s_t^2 + \sum_{i=3}^{n} (i)b_i = 0 \tag{E.29b}$$

$$2s_t^2 + \sum_{i=3}^{n} (i)(i-1)b_i = -2k_{1_a} \tag{E.29c}$$

Setting $n = 5$ yields a unique solution for equations (E.29).

Rather than solving for the b_i, $i = 3$, 4, 5, by direct elimination, we follow the procedure given in Section E.1. Since $y^2(x)$ is linear in the b_i, $i = 3$, 4, 5, which are linear in s_t^2 and k_{1_a}, we postulate that

$$y^2(x) = s_t^2 F_1(x) + k_{1_a} F_2(x) + G(x) \tag{E.30}$$

where $F_1(x)$, $F_2(x)$, and $G(x)$ are polynomials of degree $n = 5$, and s_t^2 and k_{1_a} are independent and arbitrary for the moment. Following the procedures of Section E.1, we obtain finally the pointed aftbody profile equations (4.5) and (4.6) in Chapter 4. In equation (4.5), parameter k_{1_a} has been eliminated using equation (E.24).

Constraint Boundaries for s_t and k_{1_a}. From physical considerations we require a nonpositive slope S_t at the tail, and a nonpositive curvature K_1 at the maximum diameter section. We have defined s_t and k_{1_a} so that $s_t \geq 0$ and $k_{1_a} \geq 0$ satisfy these physical requirements.

Either no or one inflection point on the pointed aftbody is allowed. We consider the noninflected case first, proceeding as in Section E.1 for the forebody. The limiting inflection point condition is expressed by equation (E.19) for $X_m \leq X \leq 1$.. Using equations (E.22), (E.29), (E.4), (E.5), (E.6), and (E.7), equations (E.19) reduce to equations (E.20). These are solved using the Secant Method [30]. The solution is given in Table E2 and is plotted in Figure 19 in Chapter 4.

Although Table E2 contains an entry for x = 0, there is actually a singularity there with an infinite number of solutions. For x = 0, equation (E.20a) is identically satisfied and equation (E.20b) reduces to

$$3s_t^2 + k_{1_a} = 10 \qquad (E.31)$$

where equation (E.30) has been used. This straight line is plotted in Figure 21 in Chapter 4.

E.3 Midbody Section

The midbody section used with the eight-parameter tailboom body is shown in Figure E3 with its dimensional parameters. The maximum diameter D occurs at the axial location X_m; the curvature at this point is
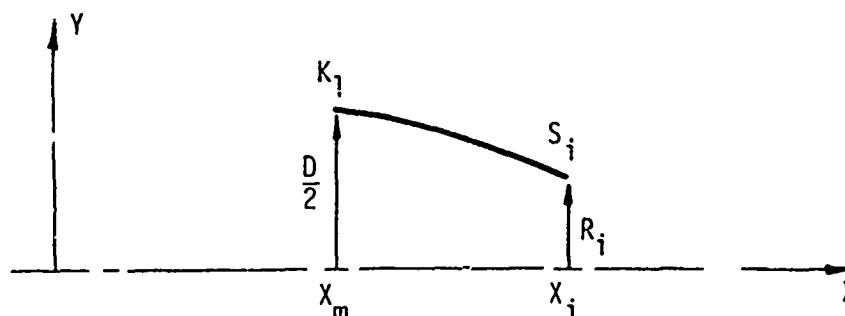

Figure E3. Midbody Section.

Table E2. Solution for Limiting Inflection on Pointed Aftbody.

x	$k_{1_a}*$	s_t^2	x	$k_{1_a}*$	s_t^2
.000	5.0000	1.6666	.520	7.1756	3.1789
.020	5.0546	1.6490	.540	7.1986	3.5385
.040	5.1118	1.6317	.560	7.1927	3.9549
.060	5.1718	1.6150	.580	7.1518	4.4330
.080	5.2348	1.5990	.600	7.0690	4.9769
.100	5.3008	1.5840	.620	6.9370	5.5894
.120	5.3701	1.5703	.640	6.7480	6.2706
.140	5.4428	1.5582	.660	6.4944	7.0169
.160	5.5191	1.5482	.680	6.1695	7.8194
.180	5.5990	1.5407	.700	5.7690	8.6614
.200	5.6826	1.5365	.720	5.2923	9.5174
.220	5.7701	1.5362	.740	4.7449	10.3520
.240	5.8614	1.5407	.760	4.1403	11.1212
.260	5.9564	1.5510	.780	3.5005	11.7770
.280	6.0549	1.5685	.800	2.8551	12.2756
.300	6.1568	1.5946	.820	2.2371	12.5868
.320	6.2614	1.6311	.840	1.6772	12.7019
.340	6.3682	1.5799	.860	1.1976	12.6356
.360	6.4762	1.7434	.880	.8090	12.4200
.380	6.5845	1.8243	.900	.5111	12.0961
.400	6.6914	1.9257	.920	.2954	11.7039
.420	6.7952	2.0508	.940	.1493	11.2769
.440	6.8937	2.2036	.960	.0595	10.8403
.460	6.9843	2.3881	.980	.0133	10.4112
.480	7.0640	2.6089	1.000	.0000	10.0000
.500	7.1291	2.8708			

$$* \ k_{1_a} = (\frac{1-x_m}{x_m})^2 k_1 \ \text{as given by equation (E.24)}$$

K_1. An inflection point occurs at X_i; at this point the slope is S_i and the profile radius is R_i. The boundary conditions for this profile $Y(X)$ are listed below where primes on $Y(X)$ denote differentiation with respect to X:

1. $Y(X_m) = D/2$ (E.32a)

2. $Y'(X_m) = 0$ (E.32b)

3. $Y''(X_m) = K_1$ (E.32c)

4. $Y(X_i) = R_i$ (E.32d)

5. $Y'(X_i) = S_i$ (E.32e)

6. $Y''(X_i) = 0$ (E.32f)

where D, K_1, R_i, S_i, X_m, and X_i may all vary.

It is possible to reduce $Y(X)$ to a nondimensional profile with only two variable boundary conditions. We define the nondimensional profile to be

$$x = (X_i - X)/(X_i - X_m) \qquad \text{(E.33a)}$$

$$y = (Y - R_i)/(D/2 - R_i) \qquad \text{(E.33b)}$$

so that the boundary conditions given by equations (E.32) become

1. $y(0) = 0$ (E.34a)

2. $y'(0) = -(X_i - X_m)S_i/(D/2 - R_i) = s_i$ (E.34b)

3. $y''(0) = 0$ (E.34c)

4. $y(1) = 1$ (E.34d)

5. $y'(1) = 0$ (E.34e)

6. $y''(1) = (X_i - X_m)^2 K_1/(D/2 - R_i) = -k_{1_m}$ (E.34f)

where primes on $y(x)$ denote differentiation with respect to x. From equations (E.3f) and (E.34f) it is apparent that

$$k_{1_m} = k_1(X_i/X_m - 1)^2/(1 - 2R_i/D) = k_1(x_i/x_m - 1)^2/(1 - r_i)$$ (E.35)

where $x_m = X_m/L$, $x_i = X_i/L$, and $r_i = 2R_i/D$. The variable boundary conditions are s_i and k_{1_m}; two free parameters make it possible to conveniently plot constraint boundaries for the midbody section.

Deviating somewhat from Granville's procedure, we postulate immediately that

$$y(x) = k_{1_m} F_1(x) + s_i F_2(x) + G(x)$$ (E.36)

where $F_1(x)$, $F_2(x)$, and $G(x)$ are polynomials of degree five since there are six boundary conditions given by equations (E.34). It is emphasized that equation (E.36) is an "ordinary" polynomial involving $y(x)$ rather than the "quadratic" polynomial used by Granville which involves $y^2(x)$. If equation (E.36) is an incorrect postulate, then some of the boundary conditions (E.34) will not be satisfied.

For arbitrary values of k_{1_m} and s_i the boundary conditions for the functions $F_1(x)$, $F_2(x)$, and $G(x)$ are

$$F_1(0) = 0 \qquad F_1(1) = 0$$
$$F_1'(0) = 0 \qquad F_1'(1) = 0$$
$$F_1''(0) = 0 \qquad F_1''(1) = -1$$

$$F_2(0) = 0 \qquad F_2(1) = 0$$
$$F_2'(0) = 1 \qquad F_2'(1) = 0$$
$$F_2''(0) = 0 \qquad F_2''(1) = 0$$

$$G(0) = 0 \qquad G(1) = 1$$
$$G'(0) = 0 \qquad G'(1) = 0$$
$$G''(0) = 0 \qquad G''(1) = 0$$

For the function $F_1(x)$ we may write

$$F_1(x) = c_1 x^3 (x - 1)^2$$

which immediately satisfies the homogeneous boundary conditions. The nonhomogeneous condition gives

$$F_1(x) = -\tfrac{1}{2} x^3 (x - 1)^2 \qquad\qquad (E.37)$$

For the function $F_2(x)$ we may write

$$F_2(x) = \sum_{i=0}^{5} b_i x^i$$

since the boundary conditions cannot be satisfied by the simple form (constant) $x^m (x - 1)^n$. By direct elimination we obtain

$$F_2(x) = x - x^3 (3x^2 - 8x + 6) \qquad\qquad (E.38)$$

For the function $G(x)$ we may write

$$\frac{d}{dx} G(x) = c_1 x^2 (x - 1)^2$$

Integrating and applying $G(1) = 1$ gives

$$G(x) = x^3(6x^2 - 15x + 10) \tag{E.39}$$

Since all the $y(x)$ boundary conditions are satisfied, then apparently the postulated form given by equation (E.36) is correct. Combining equations (E.35), (E.36), (E.37), (E.38), and (E.39), and using the fact that $f_r = L/D$, we obtain finally equations (4.9) and (4.10) in Chapter 4.

Constraint Boundaries for s_i and k_{1_m}. From physical considerations we require a nonpositive slope S_i at X_i and nonpositive curvature K_1 at the maximum diameter section. We have defined s_i and k_{1_m} so that $s_i \geq 0$ and $k_{1_m} \geq 0$ satisfy these physical requirements.

We also require that no inflection points occur on the midbody except at X_i. The limiting inflection point occurs when the second derivative touches zero but does not change sign. This is expressed by equations (E.19) which reduce immediately to

$$y''(x) = 0 \tag{E.40a}$$

$$y'''(x) = 0 \tag{E.40b}$$

Equations (E.40) can be solved by direct substitution to obtain

$$k_{1_m} = \frac{G''(x) \, F_2'''(x) - G'''(x) \, F_2''(x)}{F_1''(x) \, F_2'''(x) - F_1'''(x) \, F_2''(x)} \tag{E.41a}$$

$$s_i = \frac{k_{1_m} \, F_1''(x) - G''(x)}{F_2''(x)} \tag{E.41b}$$

for the limiting inflection point condition. The solution is tabulated in Table E3 and plotted in Figure 21 in Chapter 4.

There is a singularity in equations (E.41) for x = 0. For this case equation (E.40a) is identically satisfied and equation (E.40b) reduces to

$$S_i = -\frac{1}{12} k_{1_m} + \frac{5}{3} \qquad (E.42)$$

This straight line is plotted in Figure 23 in Chapter 4.

E.4 Tailboom Aftbody Section

The tailboom aftbody section used with the eight-parameter tail-boom body is shown in Figure E4 with its dimensional parameters. An inflection point occurs at X_i; at this point the slope is S_i and the radius is R_i. There is also an inflection point at L; the terminal radius is T. The boundary conditions for this profile Y(X) are listed
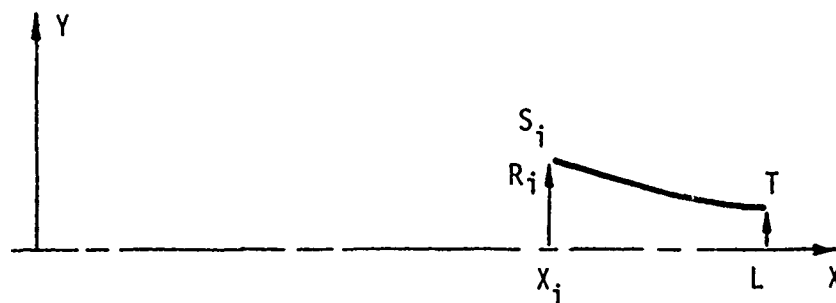

Figure E4. Tailboom Aftbody Section.

below where primes on Y(X) denote differentiation with respect to X:

Table E3. Solution for Limiting Inflection on Midbody.

x	k_{1m}*	s_i	x	k_{1m}*	s_i
.020	5.0511	1.2457	.520	7.6460	1.2787
.040	5.1048	1.2415	.540	7.7794	1.3161
.060	5.1612	1.2371	.560	7.8913	1.3641
.080	5.2203	1.2327	.580	7.9698	1.4246
.100	5.2826	1.2282	.600	8.0000	1.5000
.120	5.3480	1.2237	.620	7.9632	1.5919
.140	5.4169	1.2192	.640	7.8387	1.7016
.160	5.4896	1.2147	.660	7.6052	1.8289
.180	5.5662	1.2102	.680	7.2452	1.9716
.200	5.6470	1.2058	.700	6.7500	2.1250
.220	5.7324	1.2016	.720	6.1250	2.2812
.240	5.8225	1.1975	.740	5.3936	2.4308
.260	5.9178	1.1938	.760	4.5957	2.5638
.280	6.0185	1.1904	.780	3.7812	2.6718
.300	6.1250	1.1875	.800	3.0000	2.7500
.320	6.2374	1.1852	.820	2.2924	2.7971
.340	6.3560	1.1838	.840	1.6842	2.8157
.360	6.4810	1.1835	.860	1.1854	2.8104
.380	6.6123	1.1846	880	.7941	2.7837
.400	6.7500	1.1875	.900	.5000	2.7500
.420	6.8934	1.1926	.920	.2891	2.7048
.440	7.0419	1.2005	.940	.1467	2.6548
.460	7.1940	1.2121	.960	.0588	2.6029
.480	7.3478	1.2282	.980	.0132	2.5508
.500	7.5000	1.2500	1.000	.0000	2.5000

* $k_{1m} = (x_i/x_m - 1)^2/(1 - r_i)$ by equation (E.35)

$$1. \quad Y(X_i) \quad = \quad R_i \qquad\qquad\qquad (E.43a)$$

$$2. \quad Y'(X_i) \quad = \quad S_i \qquad\qquad\qquad (E.43b)$$

$$3. \quad Y''(X_i) \quad = \quad 0 \qquad\qquad\qquad (E.43c)$$

$$4. \quad Y(L) \quad = \quad T \qquad\qquad\qquad (E.43d)$$

$$5. \quad Y'(L) \quad = \quad 0 \qquad\qquad\qquad (E.43e)$$

$$6. \quad Y''(L) \quad = \quad 0 \qquad\qquad\qquad (E.43f)$$

where R_i, S_i, T, X_i, and L may all vary.

It is possible to reduce $Y(X)$ to a nondimensional profile with only two variable boundary conditions. We define the nondimensional profile to be

$$x \quad = \quad (L - X)/(L - X_i) \qquad\qquad\qquad (E.44a)$$

$$y \quad = \quad Y/R_i \qquad\qquad\qquad (E.44b)$$

so that the boundary conditions given by equations (E.31) become

$$1. \quad y(0) \quad = \quad T/R_i \quad = \quad t/r_i \qquad\qquad\qquad (E.45a)$$

$$2. \quad y'(0) \quad = \quad 0 \qquad\qquad\qquad (E.45b)$$

$$3. \quad y''(0) \quad = \quad 0 \qquad\qquad\qquad (E.45c)$$

$$4. \quad y(1) \quad = \quad 1 \qquad\qquad\qquad (E.45d)$$

$$5. \quad y'(1) \quad = \quad -(L - X_i) \, S_i/R_i \quad = \quad s_{i_a} \qquad\qquad\qquad (E.45e)$$

$$6. \quad y''(1) \quad = \quad 0 \qquad\qquad\qquad (E.45f)$$

where primes on $y(x)$ denote differentiation with respect to x and $t = 2T/D$ and $r_i = 2R_i/D$. It is apparent from equations (E.34b) and (E.45e) that

$$s_{i_a} = s_i[(L - X_i)(D/2 - R_i)]/[(X_i - X_m)(R_i)]$$

$$= s_i[(1 - x_i)(1 - r_i)]/[(x_i - x_m)(r_i)] \qquad (E.46)$$

where $x_m = X_m/L$, $x_i = X_i/L$, and $r_i = 2R_i/D$. The variable boundary conditions are s_{i_a} and t/r_i; two free parameters make it possible to conveniently plot constraint boundaries for the tailboom aftbody.

Following the procedure in Section E.3, we postulate immediately that

$$(x) = \frac{t}{r_i} F_1(x) + s_{i_a} F_2(x) + G(x) \qquad (E.47)$$

where $F_1(x)$, $F_2(x)$, and $G(x)$ are polynomials of degree five since there are six boundary conditions given by equations (E.45). For arbitrary values of t/r_i and s_{i_a} the boundary conditions for the function $F_1(x)$, $F_2(x)$, and $G(x)$ are

$$
\begin{array}{llll}
F_1(0) & = 1 & F_1(1) & = 0 \\
F_1'(0) & = 0 & F_1'(1) & = 0 \\
F_1''(0) & = 0 & F_1''(1) & = 0 \\
\\
F_2(0) & = 0 & F_2(1) & = 0 \\
F_2'(0) & = 0 & F_2'(1) & = 1 \\
F_2''(0) & = 0 & F_2''(1) & = 0 \\
\\
G(0) & = 0 & G(1) & = 1 \\
G'(0) & = 0 & G'(1) & = \\
G''(0) & = 0 & G''(1) & = 0
\end{array}
$$

For the function $F_1(x)$ we may write

$$\frac{d}{dx} F_1(x) = c_1 x^2 (x - 1)^2$$

Integrating and applying conditions $F_1(0) = 1$ and $F_1(1) = 0$ gives

$$F_1(x) = 1 - x^3(6x^2 - 15x + 10) \qquad (E.48)$$

For the function $F_2(x)$ we may write

$$F_2(x) = \sum_{i=0}^{5} b_i x^i$$

since the boundary conditions cannot be satisfied by the simple form (constant) $x^m (x - 1)^n$. By direct elimination we obtain

$$F_2(x) = -x^3(3x^2 - 7x + 4) \qquad (E.49)$$

The function $G(x)$ has the same boundary conditions as in Section E.3; thus equation (E.39) applies directly. Equations (E.39) and (E.48) imply that

$$G(x) = 1 - F_1(x) \qquad (E.50)$$

so that

$$y(x) = 1 + (\frac{t}{r_i} - 1) F_1(x) + s_{i_a} F_2(x) \qquad (E.51)$$

Equations (E.48), (E.49), and (E.51) satisfy the boundary conditions (E.45); hence the postulated form given by (E.47) is correct. The results are given as equations (4.11) and (4.12) in Chapter 4, to which equation (E.46) has been applied.

Constraint Boundaries for s_{i_a} and t/r_i. From physical considerations we require a nonpositive slope S_i, a positive profile radius R_i at X_i, and a non-negative profile radius T at L. We have defined s_{i_a}, t, and r_i so that $s_{i_a} \geq 0$ and $0 \leq t/r_i \leq 1$ satisfy these physical requirements.

We also require that no inflection points occur on the tailboom aftbody other than at X_i and L; this implies that at most one inflection can occur on $X_i < X < L$. Equations (E.40) cannot be used to find the constraint boundaries; no solution exists on $0 < x < 1$ so that an alternate approach is required. Using equation (E.40a) together with equation (E.51) one may write

$$y''(x) = (\frac{t}{r_i} - 1) F_1''(x) + s_{i_a} F_2''(x) = 0 \qquad (E.52)$$

Factoring out the solutions at x and $x = 1$, we obtain after some manipulation that

$$x = \frac{[1 + \frac{2}{5} \frac{s_{i_a}}{(t/r_i - 1)}]}{[2 + \frac{s_{i_a}}{(t/r_i - 1)}]}$$

which is the location of the third inflection point. It is apparent that we must find the range of $s_{i_a}/(t/r_i - 1)$ for which $x \leq 0$ and $x \geq 1$. Setting $x \leq 0$ and then $x \geq 1$ in equation (E.53) and performing the inequality analyses gives

$$-\frac{5}{3} \frac{t}{r_i} + \frac{5}{3} \leq s_{i_a} \leq -\frac{5}{2} \frac{t}{r_i} + \frac{5}{2} \qquad (E.54)$$

which defines the region for which no inflection point exists on $0 < x < 1$. These linear boundaries are plotted in Figure 24 of Chapter 4.

APPENDIX F

ADDITIONAL RESULTS

This appendix contains additional optimization results not reported in Chapter 5. Also, summary tables and figures of all optimization runs are presented. Unless otherwise noted, all optimization runs are made using 30-station solutions. However, the reported drag coefficients are 99-station solutions. The computer running time in minutes is nominally equal to the number of performance function (PF) evaluations on the CDC 6500.

F.1 Eight-Parameter Tailboom Body at $R_V = 7 \times 10^6$.

The results for the eight-parameter tailboom body are limited; the summary is shown in Table F1. The additional data not previously reported is the comparison of the C_D values based on the 30-station and 99-station solutions. For body D-54 at $R_V = 7 \times 10^6$ the predicted C_D decreases 11% when 99 stations are used.

F.2 Five-Parameter All-turbulent Body at $R_V = 5 \times 10^6$.

The three optimization runs for this body are summarized in Table F2; overall parameter migrations are shown in Figure F1. From the table it is evident that there is essentially no relative distortion of the response surface due to the 30-station solutions. This suggests that the coarse 30-station grid loses important information associated with the rapid change in the boundary layer immediately downstream of the point transition. This rapid change does not occur in an all-turbulent

Table F1. Optimization Summary for 8-Parameter Tailboom Body at $R_V = 7 \times 10^6$.

Run No.	Search Method	No. of PF Eval.	Best Design	C_D (99-Sta.)	C_D (30-Sta.)	Figure No.	Comments
D	Complex	65	D-54	.00566	.00638	25	One-fourth lower C_D than "Dolphin." Run terminated prematurely. Body suboptimal.
U	Complex	60	U-35		.00564		Different initial complex than Series D. No formal convergence.
V	Powell						Initial guess body U-35. Used 99-station solutions. One cycle only.

Table F2. Optimization Summary for 5-Parameter All-turbulent* Body at $R_V = 5 \times 10^6$.

| Run No.	Search Method	No. of PF Eval.	Best Design	C_D (99-Sta.)	C_D (30-Sta.)	Figure No.	Comments
I	Complex	38	I-36	.01976	.02024	30	No better than Series 58. Run near convergence. Response surface quite flat.
I2	Complex	27	I2-24	.02065	.02125	--	Formal convergence achieved. No evidence of relative distortion due to 30-station solutions.
I3	Complex	27	I3-27	.01982	.02026	--	Formal convergence achieved.

* Boundary tripped at X/L = .05.
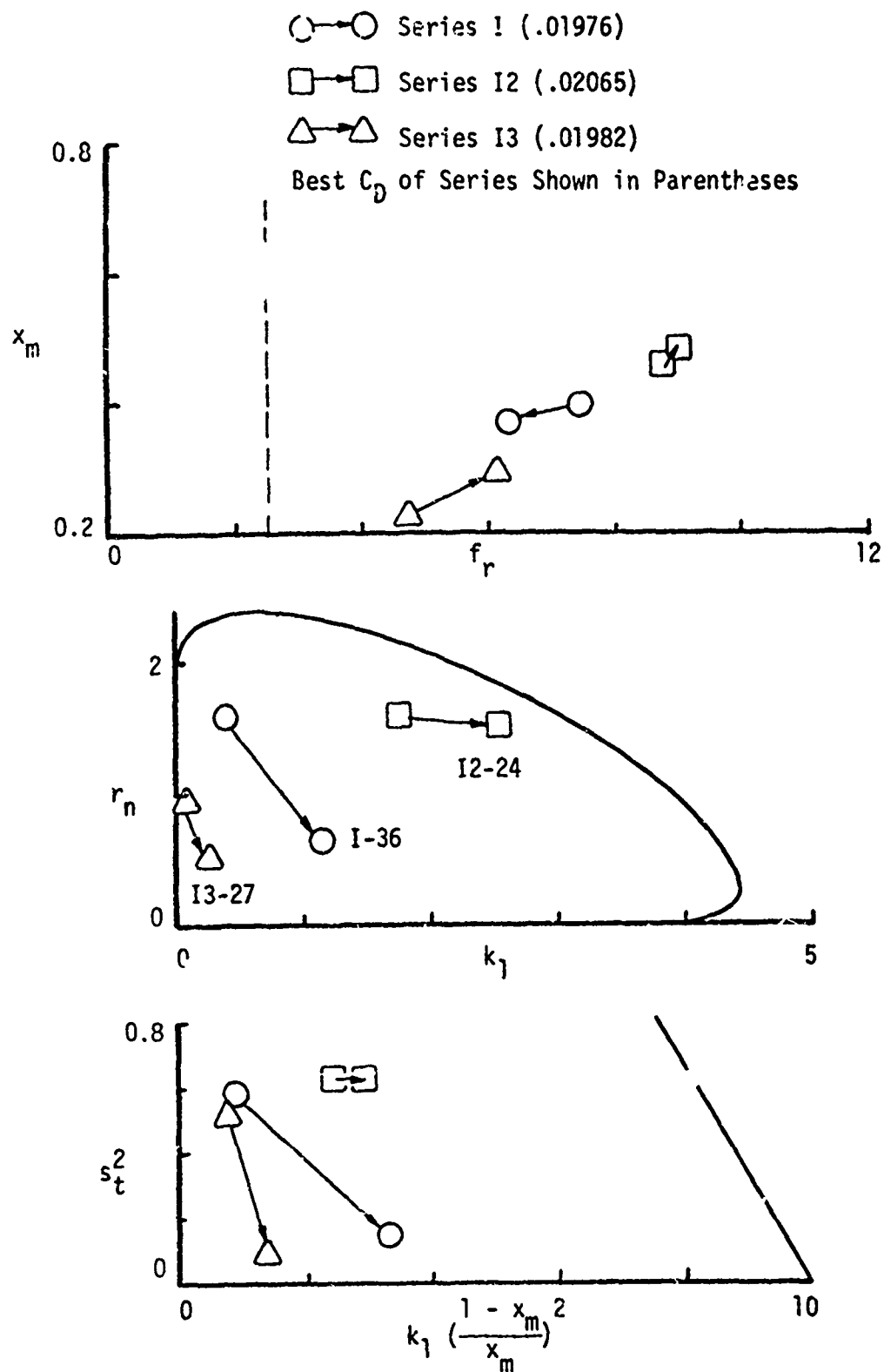
Figure F1. Summary of Parameter Migrations for
All-turbulent Bodies at $R_V = 5 \times 10^6$.

boundary layer. From Figure F1 it is apparent that the response surface for all-turbulent bodies at $R_V = 5 \times 10^6$ is quite flat. The three solutions are spatially far apart but their C_D values are all within 4.5% of the best value. The parameters for the three all-turbulent solutions are given in Table F3.

F.3 Five-Parameter Laminar Body at $R_V = 5 \times 10^6$.

The optimization runs for this body are summarized in Table F4; overall parameter migrations are given in Figure F2. It is evident in the table that there is significant relative distortion of the response surface due to the 30-station solutions. The Complex Method, moving on global information, can cope with the relative distortion; that is, the distortion apparently does not obliterate global trends. The Powell Method, moving on local information, is useless when using 30-station solutions; the results of optimization Series P in Table F4 demonstrate this. The results of Series P motivated the initiation of Series T which uses 99-station solutions. Of course, this procedure triples the cost of the optimization run.

F.4 Five-Parameter Laminar Body at $R_V = 1.6 \times 10^7$.

The optimization runs for this body are summarized in Table F5; overall parameter migrations are shown in Figure F3. As discussed above, there is relative distortion of the response surface due to the 30-station solutions. It appears that 99-station solutions must be employed to use the Powell Method effectively.

Table F3. Parameter Values for Three All-turbulent Bodies.

Parameter	Body Number		
	I-36	I2-24	I3-27
f_r	6.3294	·8.9937	6.1323
x_m	.3692	.4815	.2924
k_1	1.1272	2.5468	.2338
r_n	.6391	1.5045	.5044
s_t^2	.1513	.6324	.0951
* k_{1_a}	3.2017	2.9534	1.3696

$$* \ k_{1_a} \ = \ k_1 (\frac{1 - x_m}{x_m})^2$$

Table F4. Optimization Summary for 5-Parameter Laminar Body at $R_y = 5 \times 10^6$.

Run No.	Search Method	No. of PF Eval.	Best Design	C_D (99-Sta.)	C_D (30-Sta.)	Figure No.	Comments
G	Complex	43	G-35	.00539	.00671	31	Run terminated prematurely. Body suboptimal.
P	Powell	32	P-17	.00597	.00625	--	Initial guess body G-35. Formal convergence achieved. Indicative of relative distortion due to 30-station solutions.
T	Powell	30	T-22	.00483	--	--	Initial guess body G-35. Used 99-station solutions. Two cycles only. No formal convergence. Parameter values given below.

Parameter Values for Body T-22:

$f_r = 8.46327$ $r_n = 2.36870$
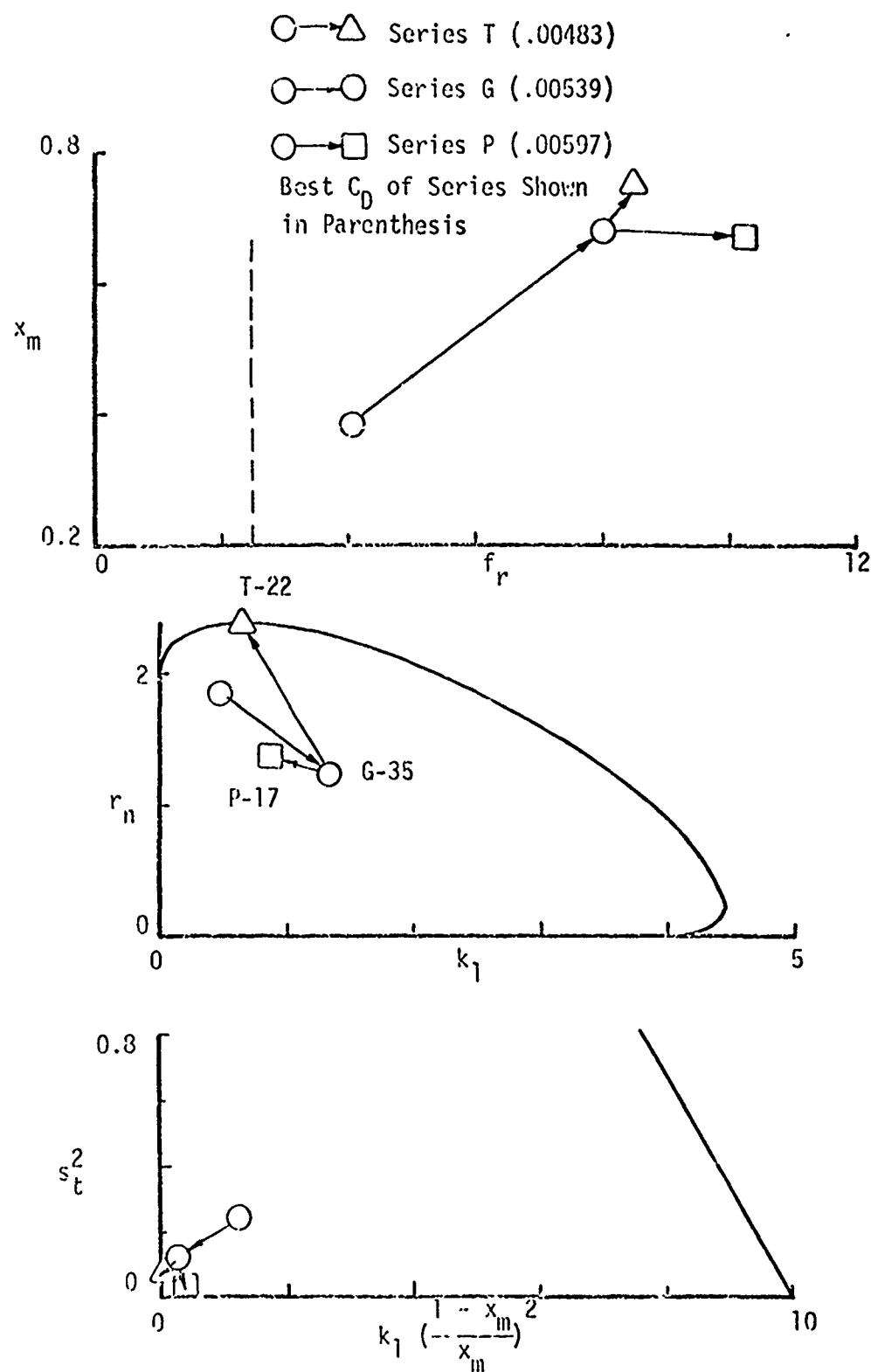
$x_m = .74939$ $s_t^2 = .07114$

$k_1 = .66100$

Figure F2. Summary of Parameter Migrations for $R_V = 5 \times 10^6$.

Table F5. Optimization Summary for 5-Parameter Laminar Body at $R_V = 1.6 \times 10^7$.

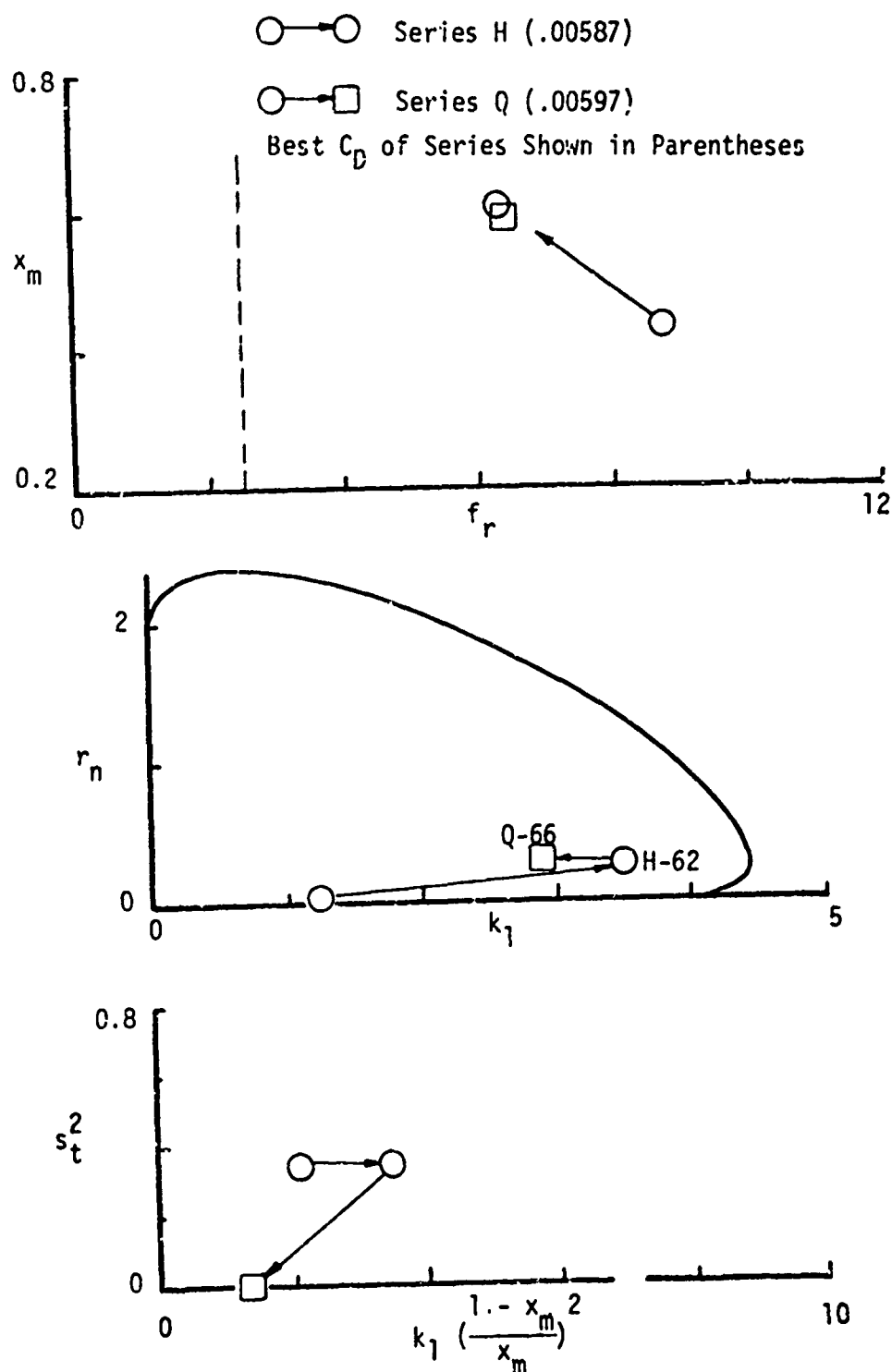| Run No.	Search Method	No. of PF Eval.	Best Design	C_D (99-Sta.)	C_D (30-Sta.)	Figure No.	Comments
H	Complex	80	H-62	.00587	.00647	35	No formal convergence. Body sub-optimal.
Q	Powell	67	Q-66	.00597	.00606	--	Initial guess body H-62. No formal convergence. Evidence of relative distortion due to 30-station solutions.

Figure F3. Summary of Parameter Migrations for $R_V = 1.6 \times 10^7$.

F.5 Five-Parameter Laminar Body at $R_V = 5 \times 10^7$.

Extensive runs have been made at this Reynolds number in an attempt to establish the existence of uniqueness of the minimum drag shapes. These runs are summarized in Table F6; the overall parameter migrations are shown in Figure F4. The results show that response surface distortion is present as mentioned in the preceding cases; however, it appears that large scale trends are not obliterated.

Based on S ·ies L, far from the feasible optimum the response surface is nominally flat with local minima present. The series is terminated before formal convergence is achieved, but after 70 PF evaluations the method is making little progress. The three Powell series K, M, and N all move rapidly to the $r_n - k_1$ boundary and then move slowly along it. It appears that the Powell Method used in conjunction with the penalty function defined by equation (3.13) cannot cope effectively with curved boundaries. Stated another way, the direction-seeking strategy of the method has difficulty aligning the search along boundaries which are not parallel to the initial set of search directions, which usually is the set of parameter axes.

Series F and F2, both using the Complex Method, converge to distinctly different shapes, as reported in Chapter 5. For this reason, the region containing these two solutions is examined in detail to determine whether the solutions are unique. By uniqueness we mean the existence of a finite number of distinct minima. Series R, using the Complex Method, revealed no significant information regarding uniqueness.

The best body shape obtained formally by an optimization run is body M-73 which lies on the $r_n - k_1$ boundary. Mainly due to the trend of Series F2 and M, it is believed that the minimum C_D at this Reynolds number lies on this boundary. Perturbations on body M-73 along the $r_n - k_1$ boundary are shown in Figure F5. A generally well behaved trend is evident; the bracketed minimum is near solution MP7 with a C_D value of .00712. This behavior suggests that the minimum drag solution is unique. However, this cannot be construed as a sufficient test for uniqueness; a truly sufficient test for uniqueness does not exist for this problem.

Table F6. Optimization Summary for 5-Parameter Laminar Body at $R_V = 5 \times 10^7$.

| Run No.	Search Method	No. of PF Eval.	Best Design	C_D (99-Sta.)	C_D (30-Sta.)	Figure No.	Comments
	Complex	90	F-57	.00765	.00749	39	No formal convergence. Evidence of relative distortion due to 30-station solutions.
F2	Complex	70	F2-49	.00727	--	42	No formal convergence.
K	Powell	61	K-57	.01236	.00911	--	No formal convergence. Method moving slowly along $r_n - k_1$ boundary.
L	Powell	70	L-67	.01113	.01171	--	No formal convergence. Apparent local minimum far from global feasible optimum.
M	Powell	75	M-73	.00716	.00712	--	No formal convergence. Method moving slowly along $r_n - k_1$ boundary.
N	Powell	61	N-61	.00783	.00729	--	Initial guess body F-57. No formal convergence. Method moving slowly along $r_n - k_1$ boundary.
R	Complex	30	R-2	.00723	.00712	--	Small initial complex in vicinity of M-73 and N-61. Run terminated prematurely.
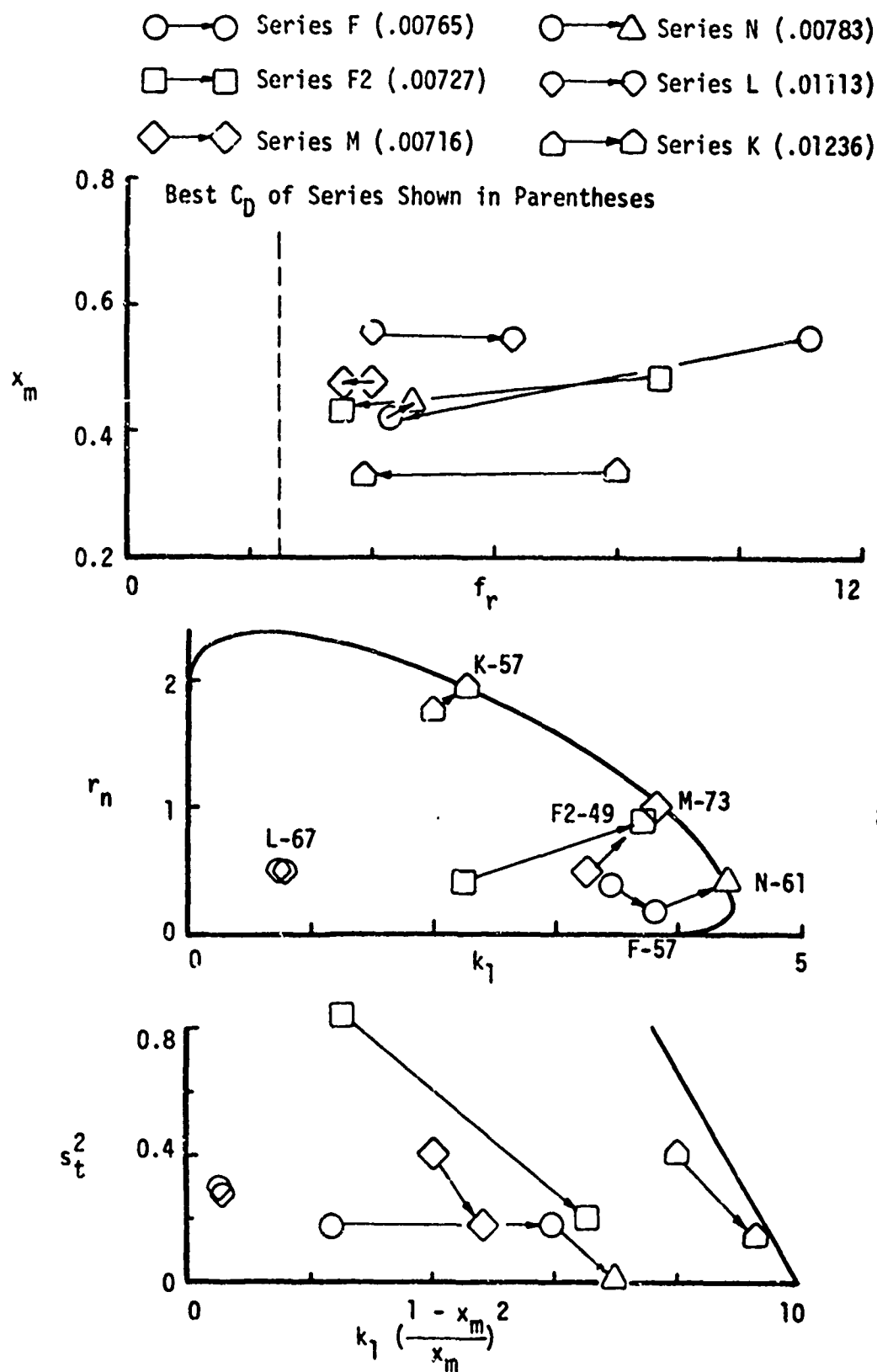
Figure F4. Summary of Parameter Migrations for $R_V = 5 \times 10^7$.

$$f_r = 3.531$$
$$x_m = .4710$$
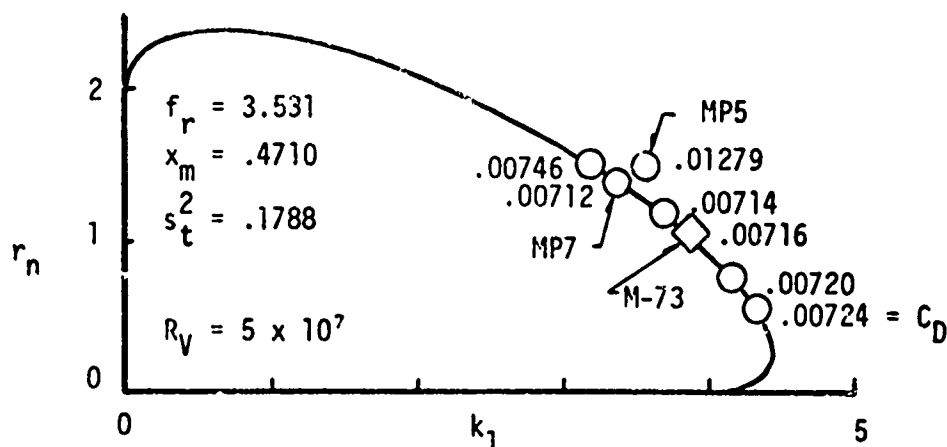$$s_t^2 = .1788$$
$$R_V = 5 \times 10^7$$

Figure F5. Perturbations on Body M-73 along r_n - k_1 Boundary.

Assuming that the optimum solution at $R_V = 5 \times 10^7$ is body MP7, then it is proper to question the validity of the presumed boundary on which the optimum lies. An additional perturbation, body MP5 with $C_D = .01279$, reveals that the response surface ascends rapidly outside the presumed feasible region. This tends to confirm the previous hydrodynamic experience which motivated the presence of this boundary at the outset. The parameters for six laminar bodies obtained in studies at $R_V = 5 \times 10^7$ are summarized in Table F7.

It is of interest to examine the hydrodynamic reasons why body MP7 has a low C_D while its close neighbor, body MP5, has such an inferior C_D value. Body MP7 and its velocity distribution are shown in Figure F6. The forebody has a limiting inflection at $X/L = .26$. The curvature behavior induces an early adverse velocity gradient region which the laminar boundary survives at this Reynolds number, at least according to the flow model. A region of locally accelerated flow suppresses transition until $X/L = 0.5$. The early adverse region helps to reduce skin friction but it has a destabilizing effect on the laminar flow. This can be seen in Figure F7 which shows the R_θ versus R_S trajectory at $R_V = 5 \times 10^7$. The trajectory very nearly touches the Michel-e[9] curve at $X/L = .25$ approximately. The region of locally accelerated flow

Table F7. Parameter Values for Six Laminar
Bodies Designed at $R_V = 5 \times 10^7$.

Parameter	Body Number					
	F-57	F2-49	M-73	MP5	MP7	R-2
f_r	4.2735	3.5000	3.5306	3.5306	3.5306	3.7866
x_m	.4446	.4300	.4710	.4710	.4710	.4729
k_1	3.8081	3.7000	3.8191	3.5000	3.3500	4.1106
r_n	.1821	.9000	1.0217	1.5500	1.3900	.5607
s_t^2	.1773	.2000	.1789	.1789	.1789	.0478
* k_{1a}	5.9443	6.5015	4.8157	4.4133	4.2242	5.1086
c_D	.0077	.0073	.0072	.0128	.0071	.0072

$$* \; k_{1a} \; = \; k_1 \left(\frac{1 - x_m}{x_m} \right)^2$$
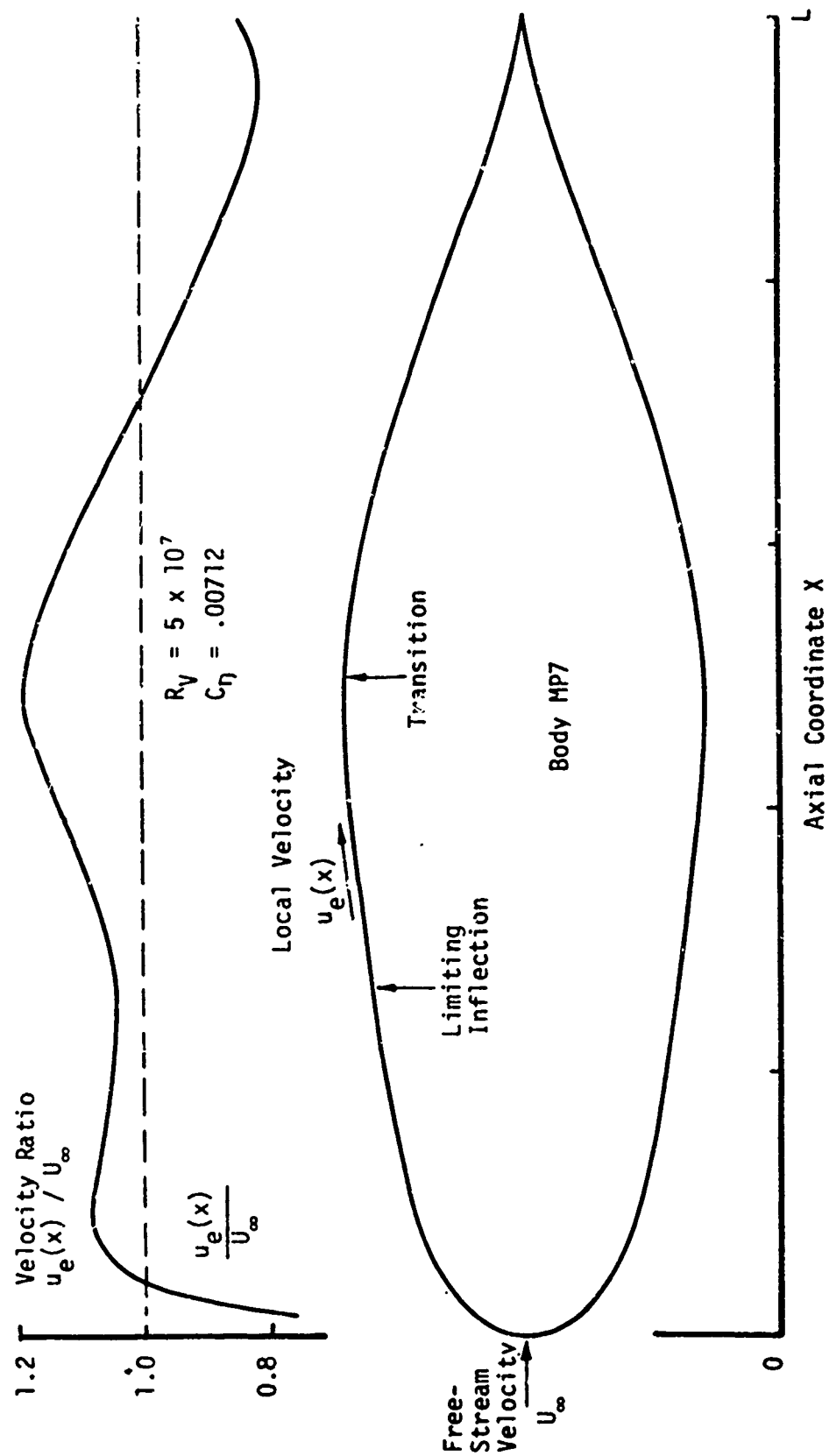
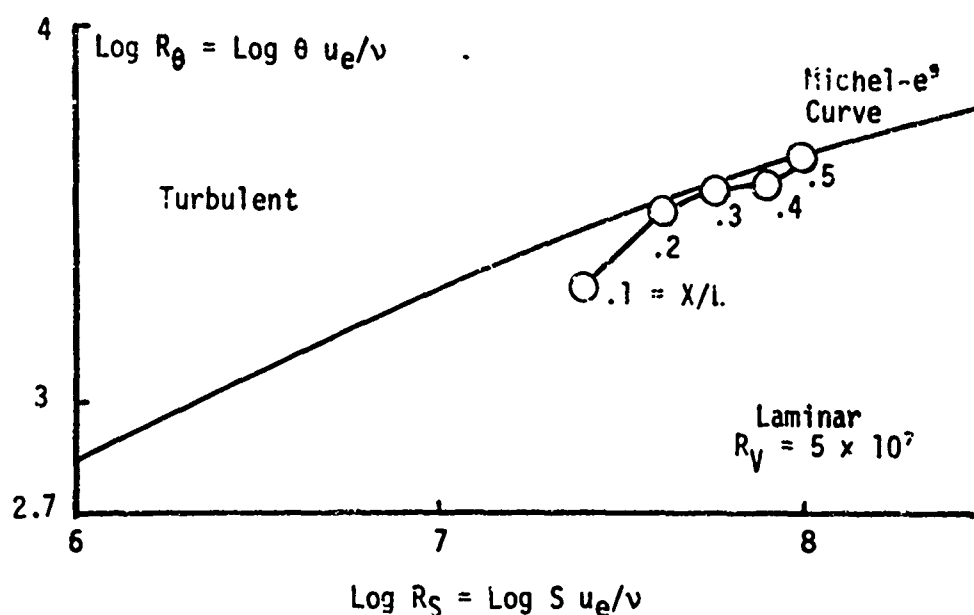Figure F6. Body MP7: Lowest C_D at $R_V = 5 \times 10^7$.

Figure F7. R_θ Versus R_S for Body MP7.

causes the trajectory to veer away and then cross the correlation curve at $X/L = 0.5$. The neighboring solution, body MP5, appears very similar to body MP7 and has a similar velocity distribution (figure not shown). However, the early adverse region for body MP5 is severe enough to cause its R_θ versus R_S trajectory to cross the Michel-e^9 curve at $X/L = .22$. This accounts for the rapid change in C_D between the neighboring solutions.

The high sensitivity of body MP7 to early transition, as inferred from Figure F7, makes it an undesirable hydrodynamic design. The trade-off between low C_D and low sensitivity to early transition must be left to the judgement of the designer. It is possible, of course, to insert additional constraints into the drag minimization problem to avoid this undesirable sensitivity.